

# Non-LTE Luminosity and Abundance Diagnostics of Classical Novae in X-rays

by  
Peter Nemeth

Master of Science in Astronomy  
University of Szeged  
Hungary, 2004

A dissertation submitted to  
Florida Institute of Technology  
in partial fulfillment of the requirements  
for the degree of

Doctor of Philosophy  
in  
Physics

Melbourne, Florida  
May 2018

© Copyright 2018 Peter Nemeth  
All Rights Reserved

The author grants permission to make single copies

---

We the undersigned committee hereby recommends that the attached document be accepted as fulfilling in part the requirements for the degree of Doctor of Philosophy in Physics.

"Non-LTE Luminosity and Abundance Diagnostics of Classical Novae in X-rays"  
a dissertation by Peter Nemeth

<hr/> <p>Matthew A. Wood, Ph.D. Professor Dept. of Physics and Space Sciences Academic Advisor</p>	<hr/> <p>Terry D. Oswalt, Ph.D. Professor, Department Head Dept. of Physics and Space Sciences Co-Advisor</p>
<hr/> <p>Stephane Vennes, Ph.D. Senior Research Scientist Astronomický ústav, Ondřejov, Czech Rep. Guest Member, Former Advisor</p>	<hr/> <p>Hamid K. Rassoul, Ph.D. Professor, Associate Dean Dept. of Physics and Space Sciences, College of Sciences Committee Member</p>
<hr/> <p>Ming Zhang, Ph.D. Professor Dept. of Physics and Space Sciences Committee Member</p>	<hr/> <p>Mary L. Sohn, Ph.D. Professor Dept. of Chemistry Committee Member</p>

# ABSTRACT

Non-LTE Luminosity and Abundance Diagnostics of Classical Novae in X-rays

by

Peter Nemeth

Academic Advisor: Matthew A. Wood, Ph.D.

Classical novae have fundamental importance in astronomy as they are relevant to both an understanding of individual stellar evolution and to taking proper distance measurements on galactic and cosmological scales. Also, novae are significant sources of interstellar material, especially carbon, nitrogen, oxygen and aluminum. These standard candles are only behind supernovae and  $\gamma$ -ray bursts as the third brightest objects in the sky, and the most probable progenitors of the brightest, type Ia supernovae.

Just after a nova outburst the system enters into the constant bolometric luminosity phase and the nova maintains a stable hydrogen burning in the surface layers of the white dwarf. As the expanding shell around the nova attenuates, progressively deeper and hotter layers become visible. At the end of the constant bolometric luminosity phase, the hottest layers are exposed and novae radiate X-rays.

This work uses the static, plane-parallel model atmosphere code TLUSTY to calculate atmospheric structure, and SYNSPEC to calculate synthetic X-ray spectra of

novae. It was necessary to incorporate atomic data for the highest ionization stages for elements ranging from hydrogen to iron for both programs. Atomic data on energy levels, bound-free, bound-bound transitions and natural broadening were taken from NIST and TOPbase.

Extensive tests revealed the importance of line opacities on atmospheric parameters and on the final spectra. A correlation can be defined between effective temperature and surface gravity. The spectral appearance is not very sensitive to the joint changes of both. Due to this effect both parameters might be over-estimated with static models. These tests also showed that N VI and N VII lines are good indicators of effective temperature.

Model fitting of V4743 Sgr and V2491 Cyg confirmed the anticipated impact of modeling geometry and stellar wind. Both novae are close to or over the Eddington limit. Ionization balance and line profiles also indicate this. These results are consistent with previous studies; further and unambiguous details require a comprehensive update of TLUSTY, what is under way.

# Contents

<b>1</b>	<b>Introduction</b>	<b>1</b>
1.1	The light curve of CNe . . . . .	4
1.2	Spectral evolution . . . . .	10
1.3	Degeneracy . . . . .	13
1.4	The outburst . . . . .	18
1.5	Supersoft X-ray Sources . . . . .	19
<b>2</b>	<b>Modeling Hot Atmospheres</b>	<b>23</b>
2.1	Model Atmospheres . . . . .	23
2.2	TLUSTY and SYNSPEC . . . . .	29
<b>3</b>	<b>Model Atoms</b>	<b>41</b>
3.1	TOPbase . . . . .	42
3.2	NIST/ASD . . . . .	46
3.3	TOPAtom . . . . .	48
<b>4</b>	<b>X-ray Modeling of Classical Novae</b>	<b>66</b>

4.1	Model Example . . . . .	79
4.2	Trends in the model grid . . . . .	93
4.3	Comparison with TMAP . . . . .	109
<b>5</b>	<b>Observations of Classical Novae</b>	<b>111</b>
5.1	Chandra . . . . .	112
5.2	XMM-Newton . . . . .	115
5.3	Data Reduction . . . . .	117
5.4	Interstellar absorption . . . . .	119
5.5	Instrumental resolution . . . . .	121
5.6	Application to Observations . . . . .	124
5.6.1	V4743 Sgr . . . . .	124
5.6.2	V2491 Cyg . . . . .	136
<b>6</b>	<b>Conclusions</b>	<b>143</b>
6.1	Future directions . . . . .	147
	<b>Appendices</b>	<b>154</b>
<b>A</b>	<b>O VI model atom</b>	<b>155</b>
<b>B</b>	<b>Catalog of Galactic CNe with Supersoft Phase</b>	<b>161</b>

# List of Figures

1.1	General light curve of CNe. . . . .	5
1.2	Temporal spectral evolution of V1974 Cyg. . . . .	6
1.3	Maximum magnitude versus rate of decline (MMRD) curve for CNe. . . . .	7
1.4	Spectral evolution of the FeII class. . . . .	10
1.5	Spectral evolution of the He/N class. . . . .	12
1.6	Fermi-Dirac distribution. . . . .	15
1.7	The mass–radius relationship and mass distribution of WDs . . . . .	17
1.8	Response of WDs to mass accretion. . . . .	21
2.1	The main steps of model atmosphere calculation. . . . .	25
3.1	Example for photoionization cross-sections for Mg. . . . .	54
3.2	Example for photoionization cross-sections for O. . . . .	55
3.3	Grotrian diagram for N VII. . . . .	60
3.4	Comparison of Fe VI lines in Kurucz database and TOPbase. . . . .	63
3.5	349 even parity energy levels for Fe VI in TOPbase and NIST. . . . .	65
4.1	LTE – NLTE comparison. . . . .	68



4.2	Effects of different abundances of carbon on the final spectra. . . . .	72
4.3	Effects of different abundances of nitrogen on the final spectra. . . . .	73
4.4	Effects of different abundances of neon on the final spectra. . . . .	74
4.5	Effects of different abundances of magnesium on the final spectra. . . . .	75
4.6	Nova shell abundances. . . . .	76
4.7	Model grid. . . . .	78
4.8	Final spectrum in LTE and NLTE. . . . .	81
4.9	Atmospheric structure. . . . .	82
4.10	Ionization fractions for carbon and nitrogen. . . . .	83
4.11	Ionization fractions for oxygen, neon and magnesium. . . . .	84
4.12	Ionization fractions for aluminum, silicon and sulfur. . . . .	85
4.13	Ionization fractions for argon, calcium and iron. . . . .	86
4.14	NLTE departure coefficients of ions from H I – C VI. . . . .	88
4.15	NLTE departure coefficients of ions from N V – N VII. . . . .	89
4.16	NLTE departure coefficients of ions from O V – O VIII. . . . .	90
4.17	Departure coefficients of included ions from Ne VII – Ne X. . . . .	91
4.18	Departure coefficients of included ions from Mg IX – Mg XII. . . . .	92
4.19	NLTE-C convergence log. . . . .	94
4.20	NLTE-L convergence log. . . . .	95
4.21	Gravity sequence. . . . .	96
4.22	Gravity sequence – structure. . . . .	97
4.23	PHOENIX flux vs. mass-loss rate. . . . .	98

4.24	Temperature sequence. . . . .	99
4.25	Temperature sequence – structure. . . . .	100
4.26	Temperature–gravity sequence. . . . .	101
4.27	Models close to the Eddington limit. . . . .	103
4.28	Effects of higher energy levels. . . . .	104
4.29	Effects of metallicity. . . . .	105
4.30	Effects of metallicity on atmospheric structure. . . . .	106
4.31	Thickness of atmospheres. . . . .	107
4.32	Radiation pressure. . . . .	108
4.33	TMAP models. . . . .	110
4.34	TLUSTY models. . . . .	110
5.1	The Chandra Observatory. . . . .	113
5.2	The structure of HRMA. . . . .	114
5.3	The XMM-Newton Observatory. . . . .	116
5.4	LETG first order effective area for V4743 Sgr. . . . .	118
5.5	Correction for interstellar absorption. . . . .	120
5.6	RGS spectral resolution. . . . .	122
5.7	Correction for instrumental resolution. . . . .	123
5.8	Convolution function for instrumental resolution. . . . .	123
5.9	Spectral evolution of V4743 Sgr. . . . .	126
5.10	Comparison of LETG and RGS spectra. . . . .	127
5.11	Model fit for V4743 Sgr. March 19, 2003 . . . . .	130

5.12	Model fit for V4743 Sgr. July 18, 2003. . . . .	131
5.13	Model fit for V4743 Sgr. September 25, 2003 . . . . .	132
5.14	Model fit for V4743 Sgr. February 28, 2004 . . . . .	133
5.15	Kiel-diagram for V4743 Sgr. . . . .	135
5.16	Spectral evolution of V2491 Cyg. . . . .	137
5.17	Model fit for the May 20th spectrum. . . . .	139
5.18	Model fit for the May 30th spectrum. . . . .	140
5.19	Model fit with solar abundances. . . . .	141
6.1	Spectral lines added to the supersoft range. . . . .	144
A.1	Grotrian diagram for O VI. . . . .	160

# List of Tables

1.1	Speed classes of classical novae. . . . .	8
2.1	First and second blocks of TLUSTY input. . . . .	30
2.2	Third block of TLUSTY input: explicit atoms. . . . .	31
2.3	Fourth block of TLUSTY input: explicit ions. . . . .	32
3.1	First ten energy levels of N VI in TOPbase. . . . .	44
3.2	Photoionization cross-sections in TOPbase. . . . .	45
3.3	First ten lines of $f$ -values data for N VI. . . . .	45
3.4	First 10 energy levels of N VI in NIST/ASD. . . . .	47
3.5	Example for NIST lines data for N VI. . . . .	50
3.6	Cross correlated TOPbase and NIST line lists. . . . .	50
3.7	N VI line list up to 100 Å. . . . .	51
3.8	First ten energy levels of N VI. . . . .	52
3.9	First ten transitions of N VI. . . . .	56
3.10	CNO levels and transitions. . . . .	59
3.11	Ne and Mg levels and transitions. . . . .	61

3.12	Al and Si levels and cross sections. . . . .	62
4.1	Abundance of CO and ONeMg noave. . . . .	77
4.2	Example model parameters. . . . .	80
5.1	Chandra and XMM observations of V4743 Sgr. . . . .	125
5.2	Model parameters for V4743 Sgr. . . . .	134
5.3	X-ray observations of V2491 Cyg. . . . .	136
5.4	Model parameters for V2491 Cyg. . . . .	142

## Acknowledgements

In the first place I would like to thank to my Parents for their continuous support and encouragement to follow my hobby, even though they knew this will take me away for many years. I am working on to turn this childhood hobby into a scientific profession.

I am indebted to my advisor, Dr. Stephane Vennes, for suggesting this hot topic, teaching me the steps of spectral modeling and helping me throughout my research. I thank Dr. Matthew A. Wood for his professional help during my studies, especially in the last year when his supervision helped me to finish this work on time. Gratitude goes to Dr. Terry D. Oswalt for his advices, his careful reading and innumerable suggestions to improve this dissertation, and for his financial support in the last year. I thank to all the members in my doctoral committee for their useful comments.

My appreciation goes to Dr. Adela Kawka for her help and to the Ondřejov Observatory for supporting this project during my summer visits. I also thank Nora Reeves for her cheering and support, and Dr. Laszlo Baksay for drawing my attention to the Ph.D. program at Florida Tech.

Special thanks go to Dr. Ivan Hubeny and Dr. Thierry Lanz for developing, documenting and making TLUSTY and SYNSPEC publicly available. Similarly, I thank to the TOPbase and NIST groups for their well organized atomic data.

I thank to the Department of Physics and Space Sciences at Florida Institute of

Technology for supporting me as a teaching assistant for five years.

I am grateful to all my former teachers and professors for their work. Without their inspiration, enthusiasm and professionalism I would not be here today.

Last but not least, I thank all my friends who stood by me and brightened my days in “Boreida”. Thank You!

# Dedication

to Runci ...

*"... because there, where you want to go for  
further studies, you will learn spectroscopy ... "*  
(High school chemistry, ~1996)



# Chapter 1

## Introduction

In ancient times the Latin name *nova stella* (new star) was applied to the sudden appearance of a previously unrecorded bright star. The name was coined by Tycho Brahe after he discovered a new bright star (SN 1572) in the constellation Cassiopeia in 1572. Reports of such new stars can be traced back to about 1500 BCE in eastern and European records. According to Lundmark (1921) there were six novae (namely: Nova Vulpeculae 1670, Nova Sagittae 1783, Nova Ophiuchi 1848, Nova Corona Borealis 1866, Nova Cygni 1876 and Nova Andromedae 1885) discovered in the post-telescopic era before the application of wide-field photography in 1887. After this date their discovery rate quickly rose to the current 4–6 per year in the Milky Way. From this number the Galactic nova rate estimated by Shafter (2002) is  $30 \pm 10 \text{ yr}^{-1}$ . Observations of the evolution of Nova Ophiuchi 1848 showed that the star returned to its faint, original state at apparent magnitude 13.5 a few years after the outburst, confirming that novae are not new objects, just enormous brightenings of existing stars.

Also the recurrence of some other novae suggested that the cataclysmic process that produces the sudden outburst does not destroy the star. The different nature of novae and supernovae was not realized until the late 1930's. With respect to novae where there is a thermonuclear explosion on the surface of the star, in supernovae the entire star explodes, releasing about  $10^3$  times more energy. Without knowing the difference between the two types of objects Harlow Shapley was led to the wrong conclusion regarding the distance to spiral nebulae. This error contributed to the Great Debate about the size of the Universe in 1920. Following the detailed work of Dean B. McLaughlin in the early 1940's and Robert Kraft in the 1960's, it was realized that novae were invariably members of close binary systems. Observations showed that the progenitor is a hot star with a late-type main sequence (MS) companion. The mass estimates suggested the eruptive stars were white dwarf (WD) stars. Later the discovery of accretion disks around WDs further supported this idea. Recent theoretical work and more advanced multi-wavelength observations led to our current, fairly comprehensive picture of classical novae. Thus, novae are WDs accreting matter from a cool MS companion in a close binary system.

The initial mass function for MS stars shows an average stellar mass of  $0.6 M_{\odot}$ . Ninković and Trajkovska (2006) observationally found the same average mass for individual MS stars and about  $2 M_{\odot}$  for binaries in the solar neighborhood up to 10 pcs. Consequently, the vast majority ( $> 80\%$ ) of stellar mass is in low and intermediate mass stars. This ratio is related to their formation scenario and the fragmentation of interstellar clouds. Lada (2006) asserted that about one third of stars in our galaxy

are in binary or multiple systems, and found the larger the mass the more probable the star is not alone. On the other hand, low and intermediate mass stars ( $< 8 M_{\odot}$ ) finish their evolution on the Hertzsprung-Russell diagram as WDs. When hydrogen, the nuclear fuel of MS stars, runs out in the core the radiation and gas pressure can not counterbalance the force of gravity. In the collapsing core of the star matter is squeezed so much that electrons are forced to fill higher energy levels as all low levels are filled and they can not occupy the same states according to the Pauli exclusion principle. Energy is deposited in the kinetic energy of electrons and these free electrons give rise to the so called degenerate pressure which can stop contraction. For more massive WDs (over  $\sim 0.8 M_{\odot}$ ) electrons become relativistic. The degenerate pressure can support the star up to the Chandrasekhar mass limit. This limit is between 1.25 and 1.45  $M_{\odot}$  depending on the composition of the core. This process is accompanied by large scale mass loss, leaving behind the hot core of the star, known as a pre-WD. There is no energy generation in WDs, only the gradual release of their residual thermal energy.

The population of binary stars and the fact that WDs are the most common end products of stellar evolution suggest there are a large number of binaries which consist of WDs and MS companions. The close binaries in which members affect each others' evolution are called cataclysmic variable stars (CVs). When the secondary star fills its last stable gravitational equipotential surface (Roche lobe), it starts losing mass to the primary. The mass transfer occurs through the inner Lagrangian point, where the Roche lobes of the stars are connected. The hydrogen-rich gas ends up in an accretion

disk around, and finally on the surface of the WD. This mass transfer and its related eruptive processes cause cataclysmic variable stars to show sudden light variations.

CVs fall in two main classes depending on their magnetic fields. Classical novae (CNe), recurrent novae and U Geminorum (or dwarf novae) systems lack strong magnetic fields and may acquire an extended accretion disk. AM Herculis, and intermediate polars have strong magnetic fields which prevent the formation of a disk. In such cases the material spirals along the field lines directly to the poles of the WD.

Some classical novae emit hard X-ray radiation that originate in the shocked wind around the system and/or soft X-rays from the atmosphere of the WD. Here we will concentrate on the modeling of the soft X-ray radiation emerging from the atmospheres during the constant bolometric luminosity phase which starts just after a nova outburst.

## 1.1 The light curve of CNe

Figure 1.1 shows the general light-curve of a CNe based on the original plot published by McLaughlin (1943). The optical light variation is characterized by the remarkable initial rise, typically 6-13 magnitudes in one or two days, often with a temporary halt lasting a few hours for fast novae, to a few days for slow novae, before the final steep rise of about 2 magnitudes to maximum. The early decline is smooth for all but the slowest novae, where irregular variations are seen. The speed class of a nova is defined by the rate at which the early decline takes place. Starting about 3.5 magnitudes below maximum light, through a 2.5 magnitude drop known as the

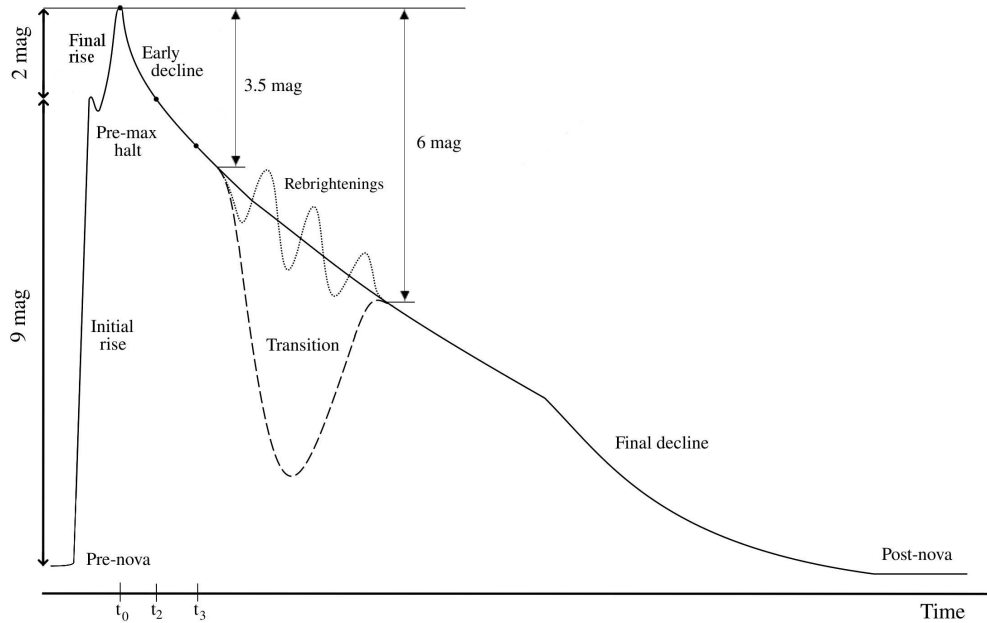


Figure 1.1: The general light curve of CNe. Figure is based on McLaughlin (1943).

transition region, showing a variety of behaviors. Faster novae usually continue to decline smoothly, others pass through a deep, 7-10 magnitude minimum lasting for 2-3 months, after which the smooth decline resumes. Still others show quasi-periodic brightness variations with amplitudes 1-1.5 mag, with a period of 5-25 days. Infrared observations show that the flux grows slowly during the initial decline and increases greatly if there is a deep minimum during the transition region. This suggests dust condensation in the expelled cooling shell causes the light variation in the transition region. The final decline to the post-nova state is usually smooth, with dwarf-nova-like variations in a few cases. Ultraviolet and X-ray observations show that the peak of the flux distribution moves steadily to shorter wavelengths after maximum light as can be seen for V1974 Cyg in Figure 1.2. The early decline in visual luminosity is due

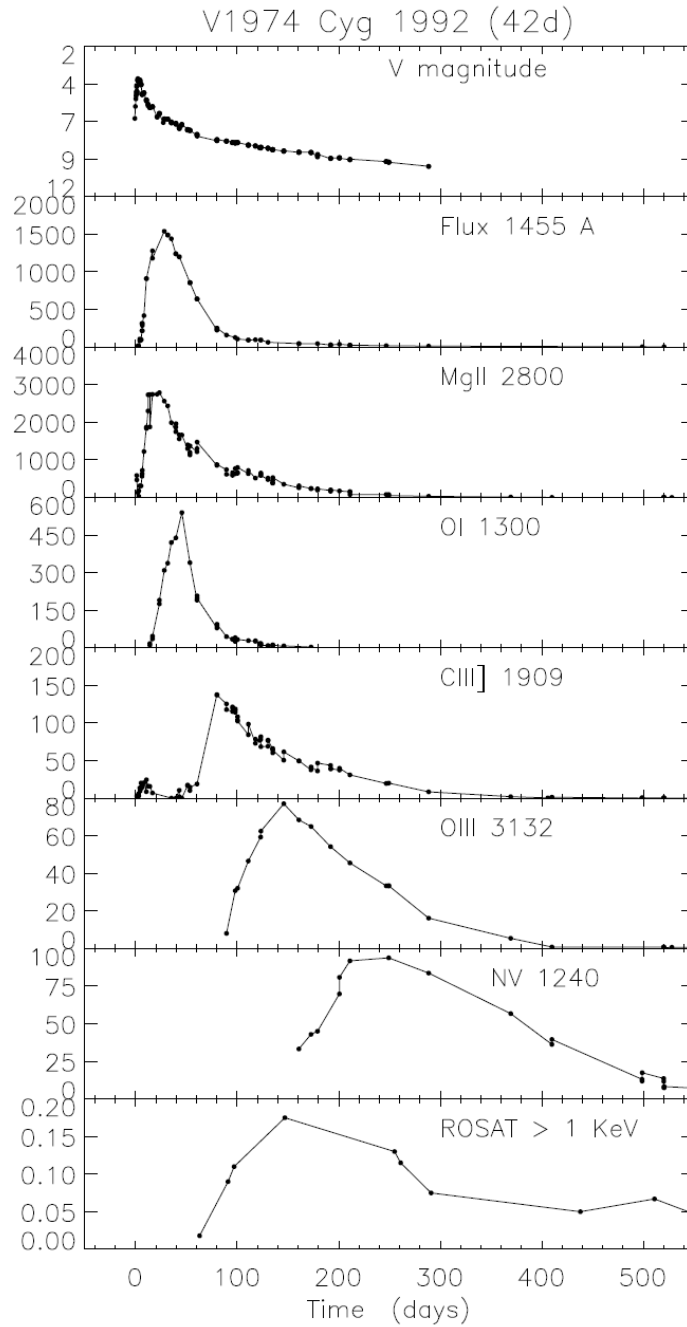


Figure 1.2: Temporal evolution of V1974 Cyg. Figure taken from Cassatella et al. (2004). Top panel shows optical V band lightcurve, bottom panel is ROSAT PSPC X-ray light curve. The rest are IUE lightcurves tracking different spectral features of V1974 Cyg.

almost entirely to the redistribution of flux. The total bolometric luminosity remains almost constant at least until the end of the transition region.

Novae are primarily classified according to the time of their decline from maximum light. This scheme is also known as the MMRD method [maximum magnitude vs. rate of decline, first introduced by McLaughlin (1945)]. For a review, see Gilmozzi and Della Valle (2003), and references therein. The rate of decline is described by the time of fading 2 or 3 magnitudes following optical maximum luminosity over a time interval denoted by  $t_2$  and  $t_3$ , respectively. Figure 1.3 shows the relation

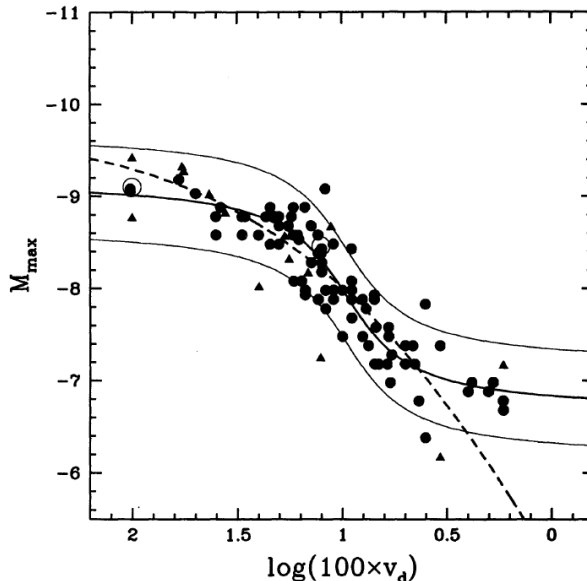


Figure 1.3: The maximum magnitude versus rate of decline (MMRD) curve for classical novae. The decline rate is expressed as  $v_d = 2/t_2$  and  $v_d = 3/t_3$ . Filled circles represent novae in M31 and triangles in LMC. The solid curves are the S shaped fit and its  $3\sigma$  ranges by Della Valle and Livio (1995), dashed curve represents the theoretical model of Livio (1992).

between the absolute magnitude and the rate of decline for novae. There are 5 speed classes based on the  $t_2$  listed in Table 1.1, although these are qualitative groups rather

Table 1.1: Speed classes of classical novae.

Speed class	$t_2$ (days)
Very fast	$< 10$
Fast	11–25
Moderately fast	26–80
Slow	81–150
Very slow	151–250

than distinct classes because the variation of the decline rate is continuous. The discovery that the rate of decline is inversely proportional to the absolute maximum brightness made such objects valuable in distance measurements. Another distance measurement technique uses the fact that all novae, almost independent of speed class, reach  $M_V \sim -5.51 \pm 0.62$  after 15 days of maximum light. These relationships are useful distance indicators for novae, or extragalactic systems in which novae occur. The extra value of novae relative to the bright and well-calibrated Cepheids is that novae, are on average, brighter by 2 magnitudes than Cepheids of the longest periods. Moreover, novae can occur in both spiral and elliptical galaxies, while Cepheids have been observed exclusively in spirals. A further advantage is that novae have a bimodal luminosity function with peaks at  $M_V = -8.8$  and  $M_V = -7.5$  magnitudes. The dip between the peaks at  $M_V = -8.2 \pm 0.15$  can be used for testing the Malmquist-bias<sup>1</sup>, which affects the completeness of the novae sample. On the other hand, due to the unpredictable nature of novae their discovery in other galaxies requires a lot of telescope time. A new calibration of MMRD with 28 objects using HST data gave

---

<sup>1</sup>A selection effect which occurs in flux limited samples. The observer sees an increase in luminosity with distance due to undetected faint objects. Because in a given intensity range it is more likely that a faint object remains undetected than a bright one.



the following linear fits, (Della Valle and Livio, 1995):

$$M_V = (2.54 \pm 0.35) \times \log t_3 - (11.99 \pm 0.56) \quad (1.1)$$

$$M_V = (2.55 \pm 0.32) \times \log t_2 - (11.32 \pm 0.44) \quad (1.2)$$

Although these linear fits proved to be only approximate relations, they are still in use because the majority of novae fall close to them. The real MMRD function is more like an S shaped function, as shown in Figure 1.3, (Della Valle and Livio, 1995):

$$M_V = -7.92 - 0.81 \arctan \left( \frac{1.32 - \log t_2}{0.23} \right) \quad (1.3)$$

A theoretical model calibrated for V1500 Cygni by Livio (1992) relates  $t_3$  to the luminosity, or to the mass of the underlying WD:

$$t_3 = 51.3 \times 10^{\frac{M_B+9.76}{10}} \times \left( 10^{\frac{M_B+9.76}{15}} - 10^{\frac{-M_B-9.76}{15}} \right)^{3/2} \quad (1.4)$$

$$t_3 = 51.3 \left( \frac{M_{WD}}{M_{Ch}} \right)^{-1} \left[ \left( \frac{M_{WD}}{M_{Ch}} \right)^{-2/3} - \left( \frac{M_{WD}}{M_{Ch}} \right)^{2/3} \right]^{3/2} \quad (1.5)$$

The flattening of the curves at the high luminosity end is real, due to super-Eddington luminosity that occurs in novae approaching the Chandrasekhar limit. The flattening at the faint end might be a selection effect, because the magnitude limit was  $m_{pg} = 19$  for the M31 survey. Its physical background is still under investigation but there is some indication that low mass WDs can cause this effect. From equations 1.4 and 1.5

it follows that the relationship between the absolute magnitude and mass of the WD is:

$$M_B \approx -8.3 - 10 \log \frac{M_{WD}}{M_\odot} \quad (1.6)$$

Thus, the more massive the WD is, the more luminous the outburst it produces. The characteristics of a light curve are also reflected in the spectral evolution.

## 1.2 Spectral evolution

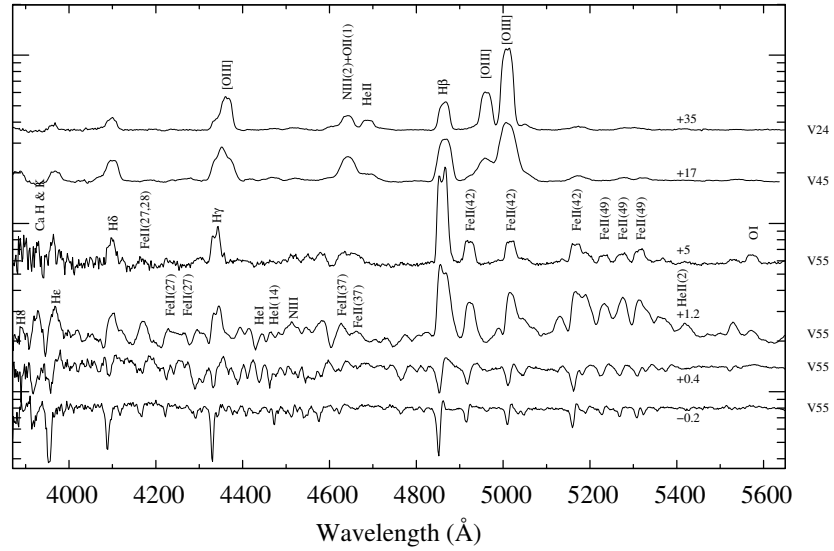


Figure 1.4: The major stages of evolution of some recent FeII class CNe. The epoch since optical maximum is indicated in days after the names of novae. Note the spectra are shifted for clarity and plotted on log scale, the offset can be found at 5400 Å for each novae. All spectra were taken with the Ortega 0.8m telescope between April and October 2008. The decline times were:  $t_{2,(V459)} = 18.3$  d,  $t_{2,(V2468)} = 10.5$  d and  $t_{2,(V5579)} = 6.1$  d.

The spectral description of classical nova evolution dates back to the extensive work

of Dean B. McLaughlin in the early 1940's (McLaughlin, 1943), and was revisited by Williams (1992). The spectral evolution is illustrated from bottom to top in Figure 1.4. The pre-maximum stage is characterized by the spectrum of a hot star with a strong continuum, blue-shifted absorption lines and weak or absent emission lines. The line shifts indicate lower velocities than after maximum. The evolution of the blue-shifted absorption line spectrum indicates an expanding and cooling photosphere. In the final expansion towards maximum, the photospheric temperature declines rapidly to 9000-4000 K depending on the speed of the nova. Spectral types in this stage are from B to A, sometimes F. The maximum luminosity stage includes the early decline, with the appearance of the "principal" spectrum showing strong P-Cygni profiles of H and Fe. Blue-shifts range from a few to several hundred km/s for slow, and around a  $10^3$  km/s for fast novae. The principal spectrum is followed by the "diffuse enhanced" spectrum about 1 or 2 days after maximum with about twice as large blue-shifts and numerous emission lines. It is characterized by strong P-Cygni profiles superimposed on a relatively cool and strong continuum, which starts fading and shifting to the blue. Strong low-ionization H, CNO and Fe emission lines appear in the spectrum. The "Orion"<sup>2</sup> spectrum appears during the transition phase, characterized by flare and coronal lines. The continuum is weaker and the shell grows optically thin as the photosphere recedes towards deeper and hotter regions. This can be seen in Figure 1.2 as well; the spectrophotometric light curves show increasing ionization stages according to increasing effective temperature. The broad emission lines show

---

<sup>2</sup>Named after the apparent similarity with Orion-nebula, which also shows strong emission lines.

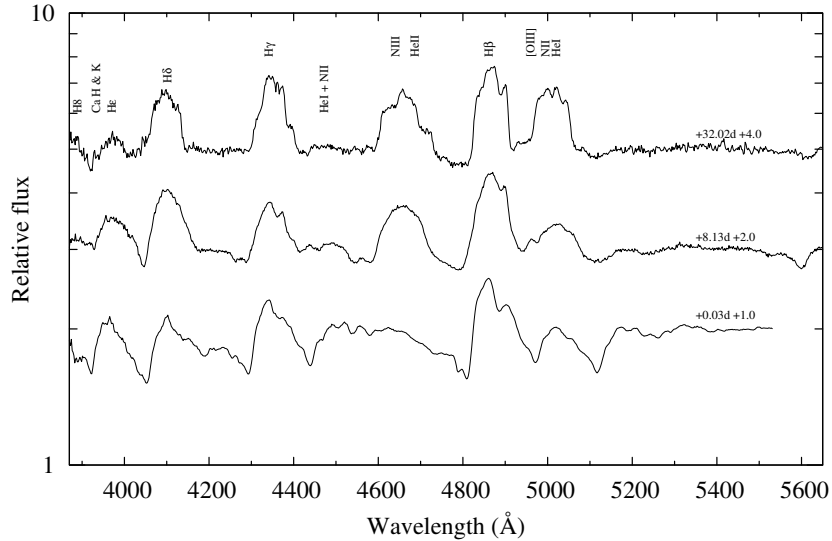


Figure 1.5: Evolution of He/N nova V2491 Cygni in the same spectral range like in Figure 1.4. The broad, rounded and jagged line profiles of H, He and N typical for these novae are clearly visible. V2491 Cyg was a very fast nova with  $t_2 = 5.65$  d. Spectra were taken with the Ortega 0.8m telescope in April and May 2008.

velocities higher than ever before and forbidden lines appear, confirming the thinning atmosphere. The photosphere is small and hot, emitting in UV and later in X-rays for novae having enough residual envelope mass or high enough accretion rate to maintain hydrogen burning. In the last, so called nebular phase, the forbidden lines strengthen and eventually dominate the spectrum, which resembles those of planetary nebulae. After years the envelope runs out of fuel, the soft X-ray radiation turns off, the star returns to its pre-nova state and the cycle starts over again.

The bimodal behavior that is seen in light curves is also present in the spectral evolution. Williams (1992) classified novae an either FeII or He/N classes (Cerro-Tololo system) based on the line properties in their permitted line spectra. About

60% of novae belong to the FeII class. The common feature of these objects are the strong FeII lines, pronounced P-Cygni profiles, slow evolution and narrow emission lines showing expansion velocity less than 2500 km/s. Novae shown in Figure 1.4 belong to the FeII type. The remaining 40% belong to the He/N class. These usually show higher excitation levels, flat, saddle shaped or jagged line emission line peaks and rapid expansion with velocity extending to 5000 km/s and fast evolution like in Figure 1.5. The classification is more complex in the nebular phase. Some FeII and He/N novae can evolve to Ne novae, forming a hybrid class. In general the main difference during the nebular phase is that FeII novae tend to have strong auroral transitions of O and N, while He/N novae either show very weak, quickly fading forbidden lines, or [FeX], or [NeIII] - [NeV] forbidden lines. He/N spectra are probably formed in discrete shells ejected at the maximum of the outburst. The narrower FeII spectra are likely formed in the subsequent wind.

### 1.3 Degeneracy

Because WDs are supported by electron degeneracy and this has a major role in nova explosions as well, a brief introduction to its physics is appropriate. Under the influence of gravity all celestial objects would be in contraction, unless some other force can counterbalance it. In MS stars the total pressure consists of the gas and the radiation pressure which comes from the liberated energy by hydrogen burning. By neglecting lower order effects like rotational and magnetic pressure the total pressure

can be written as:

$$P_{\text{total}} = P_{\text{gas}} + P_{\text{rad}} \quad (1.7)$$

$$P_{\text{total}} = NkT + \frac{4\sigma}{c} \frac{T^4}{3} \quad (1.8)$$

Where  $\sigma$  is the Stephan-Boltzmann,  $k$  is the Boltzmann constant,  $N$  is the total number density and  $c$  is the speed of light.  $T$  is the temperature of the star and  $P$  is the pressure.

When hydrogen is depleted in the core, the balance between gas, radiation pressure and gravity ends. The core starts to collapse, releasing part of its gravitational energy which initiates hydrogen shell burning around the core. The increased energy production inflates the star to a red giant and initiates large scale mass loss. Meanwhile the core is still unbalanced, contracting, heating up and getting denser. The particle energy distribution in the core is:

$$n(\epsilon) = \frac{g(\epsilon)}{e^{\alpha + \epsilon/kT} + \beta} \quad (1.9)$$

$$\alpha = \begin{cases} 0 & \text{Bose-Einstein statistics, integral spin;} \\ -\frac{h^2}{2mkT} \left(\frac{3N_e}{8\pi}\right)^{\frac{2}{3}} & \text{Fermi-Dirac statistics, half-integer spin.} \end{cases}$$

$$\beta = \begin{cases} -1 & \text{Bose-Einstein statistics, integral spin;} \\ 1 & \text{Fermi-Dirac statistics, half-integer spin.} \end{cases}$$

Where  $g(\epsilon)$  is the number density of possible states at energy  $\epsilon$ ,  $\alpha$  is the degeneracy parameter  $\beta$  is the statistical parameter and  $N_e$  is the electron density. In Figure 1.6 the occupation index  $n(\epsilon)/g(\epsilon)$  is plotted against electron energy at different degeneracy parameters. For large electron energies the Fermi-Dirac distribution shows a maxi-

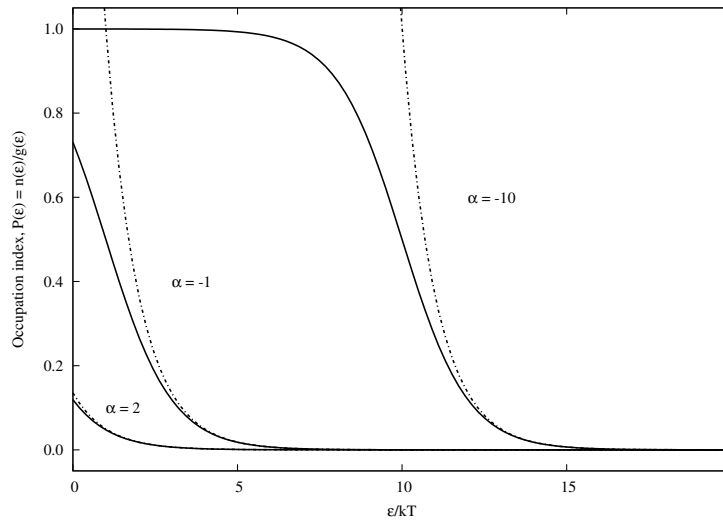


Figure 1.6: Fermi-Dirac distributions for different degeneracy parameters ( $\alpha$ ) are showed by solid lines. Maxwell-Boltzmann distributions shown by dashed-dotted lines, for low occupation indices the two statistics are identical.

mum that is a consequence of the Pauli exclusion principle. The low energy states are all occupied, electrons require more and more energy to be raised to empty high energy states and this introduces a new, electron degeneracy pressure. Also shown in Figure 1.6 are the classical Maxwell-Boltzmann statistics for each degeneracy parameter for

low occupation numbers matching with Fermi-Dirac statistics. This is analogous to the Newtonian and the relativistic theory of gravity. The Maxwell-Boltzmann statistics describe the system well for low occupation numbers and only a limiting case of the more general Fermi-Dirac distribution. At the density:

$$\frac{\rho}{\mu_e} = \frac{8\pi M_\mu}{3} \frac{(5m_e k)^{3/2}}{h^3} T^{3/2} \quad (1.10)$$

the pressure of degenerate electrons is:

$$P_e = \frac{h^2}{5m} \left( \frac{3}{8\pi} \right)^{\frac{2}{3}} N_e^{\frac{5}{3}} \quad (= P_{total}). \quad (1.11)$$

This can stop the contraction of the core. Thus, WDs are the exhausted stellar cores supported by the pressure of degenerate electrons. Note the degenerate pressure does not depend on temperature, just on electron density. As a consequence, in degenerate stars the radius is largely independent of temperature. Temperature affects the outer, normal gas envelope of these stars.

An interesting consequence of degeneracy is the WD mass-radius relation. As the degenerate pressure is a function of the density, the higher the mass of a white dwarf the smaller its radius. In Figure 1.7 the boundaries of stable regions were calculated with a 4th order Runge-Kutta numerical integration for relativistic cores consisting of light metals and iron. Also shown is the observed mass distribution by Vennes (1999) based on 141 EUV/soft X-ray selected white dwarfs. The mass limit of WDs depends



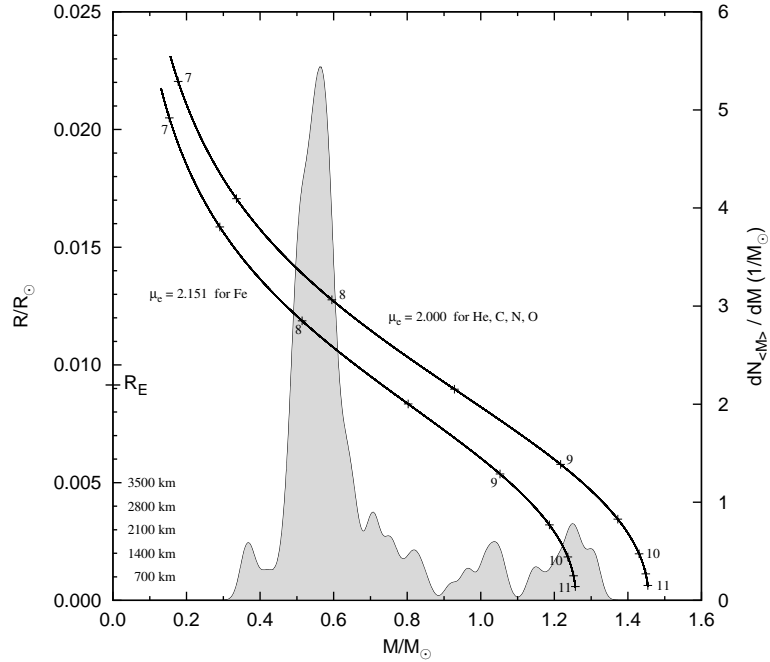


Figure 1.7: Zero temperature mass-radius relations for different electron molecular weights  $\mu_e$ . Surface gravities ( $\log g$ ) are labeled along the curves in  $\text{cm/s}^2$  units. The shaded area shows the observed mass distribution by Vennes (1999).  $R_E$  indicates the radius of Earth. For the most massive WDs radii are also shown in km.

on the core composition, in solar units:

$$M = \frac{5.87}{\mu_e^2} M_{\odot} \quad (1.12)$$

where  $\mu_e$  is the mean molecular mass per electron. This maximum mass was first realized by Subrahmanyan Chandrasekhar in the early 1930's; this work earned him the Nobel Prize in physics in 1983 and in his honor was named the Chandrasekhar limit, (Chandrasekhar, 1935).

## 1.4 The outburst

The requirements for a pre-nova are: a close binary system in which the secondary fills its Roche lobe and mass transfer rates between  $10^{-8} - 10^{-11} M_{\odot}/yr$  to the WD. At this accretion rate the hydrogen-rich material from the secondary accumulates in a layer on the WD. As the mass of the WD increases, so does the central density and the density at the boundary of the core and envelope. Eventually this reaches the critical density for relativistic degeneracy. Theoretical studies showed that the accreted layer grows until a temperature of  $> 10^7$  K and a pressure of  $> 10^{19}$  dyne/cm<sup>2</sup> is reached. More massive WDs require less material in their envelope to reach this critical density. Thus, massive WDs are expected to produce more frequent nova outbursts than their lower mass counterparts. The transferred material also carries extra heat to the envelope from released potential energy. With this extra heat and the hydrogen-rich degenerated layer in the envelope, the explosive is loaded in the gun. The core is nearly isothermal due to its high conductivity and the excess heat is expected to be distributed evenly throughout the surface layers.

When the temperature reaches the point that hydrogen ignites, the envelope suffers a thermonuclear runaway. Because the temperature goes up exponentially, the reaction rate increases suddenly and causes a chain reaction. Although the degenerate equation of state (Equation 1.11) does not depend on temperature, the degeneracy parameter does. At very high temperatures  $\alpha$  reaches small negative values, degeneracy is lifted and the material goes back to normal gas. Its temperature dependence turns on and the outer envelope expands adiabatically blowing off a significant part

of the previously accreted material.

During the outburst the atmosphere expands and cools adiabatically. The nova reaches its optical maximum at this phase. The WD gains an atmosphere like a red giant, reaching out nearly  $100 R_{\odot}$  and forming a common envelope around the stars, but it can not support this for long. Due to the strong radiation and dynamical friction with the secondary the atmosphere loses mass and the photosphere recedes. As we can see deeper and deeper into the atmosphere where temperature is higher, the peak of the energy distribution gradually shifts towards shorter wavelengths. Meanwhile there is stable hydrogen fusion at a constant rate (constant bolometric luminosity phase) on the surface of the WD which can be supported by further accretion from the secondary. The spectral analysis of this static hot WD atmosphere is the scope of this work.

## 1.5 Supersoft X-ray Sources

Supersoft X-ray sources are astronomical sources of low energy X-rays. The peak of their spectral energy distribution (SED) is between 5 and 120 Å. Normal stars burn hydrogen in their cores producing X-rays and gamma rays. By the time this radiation reaches the surface of the star, it has become visible light. However, in the mid eighties a new class of object was discovered with the Einstein Observatory: WDs which have hydrogen-burning close to their surfaces. These hot and dense stars in cataclysmic binaries can get hydrogen-rich material from their companion as a result of stellar evolution. Burning of this layer keeps the surface temperature at a few hundred

thousand Kelvins and thus is the source of the soft X-rays. Depending on the mass transfer rate there are two main classes of supersoft sources. If the mass transfer ( $\dot{M}$ ) rate is around  $10^{-7} M_{\odot} \text{ yr}^{-1}$ , it is possible that the ongoing burning is continuously supported by fresh material. These stars are referred as Close Binary Supersoft Sources (CBSS). In this case the hydrogen-burning roughly constant. The mass transfer rate must not be too high; at  $\dot{M} \geq 4 \times 10^{-7} M_{\odot} \text{ yr}^{-1}$  the released gravitational energy can stop further accretion, regulating the mass transfer and luminosity. For even higher accretion rates a common envelope forms around the stars.

If the accretion rate is low, on the order of  $10^{-8} - 10^{-11} M_{\odot} \text{ yr}^{-1}$ , the burning is episodic. In this case, a hydrogen-rich envelope builds up on the surface of the WD and it becomes a classical nova system. The recurrence time of the nova depends on the mass transfer rate and the WD's mass. The supersoft stage in this case starts with the nova event and its duration strongly depends on the WD mass and the chemical composition of the accreted material.

Figure 1.8 summarizes the response of WDs for accretion as function of WD mass and accretion rate, (Kato, 2010). The abscissa shows the WD mass in solar mass and the ordinate is the logarithm of the accretion rate ( $\dot{M}$ ) in  $M_{\odot} \text{ yr}^{-1}$ . Next to the curves are the envelope masses necessary for a nova outburst (hydrogen-shell flash). It can be seen that more massive WDs require less material for an outburst. Also shown that there is a critical rate ( $\dot{M}$ ) almost independent from WD mass at which steady hydrogen-burning occurs. Above this rate an optically thick wind forms.

Ögelman et al. (1984) discovered that soft X-ray radiation came from the classical

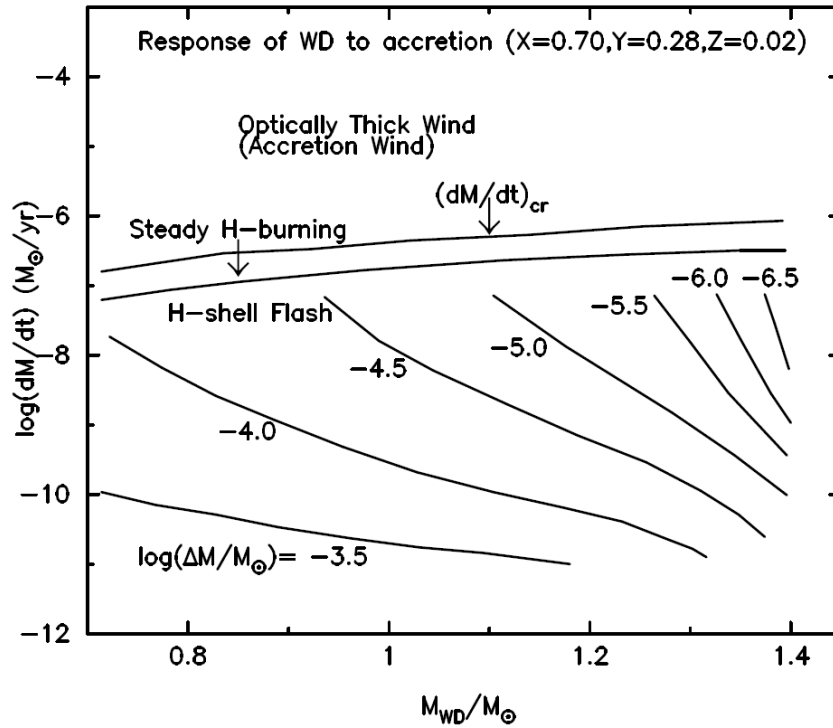


Figure 1.8: Response of WDs for mass accretion in the WD mass and mass-accretion rate plane. Figure is taken from Kato (2010).

nova GQ Mus (Nova Mus 1983) in April 1984, only two months before MacDonald et al. (1985) published the theoretical background and detectability of such radiation by EXOSAT, the only X-ray satellite that time.

The fate of these objects is also interesting. If a ONeMg WD gains enough mass it can collapse to a neutron star. If the secondary star stops donating material, hydrogen-burning turns off and the WD returns to the cooling sequence. When a CO WD reaches the Chandrasekhar limit the star explodes completely in a type Ia supernova (SNIa). The carbon core of the WD converts to nickel instantaneously, which decays to cobalt and iron in a few hundred days.

There is no clear distinction between CBSS and classical novae that emit supersoft radiation. It is possible that they are similar systems and only appear to be in a different evolutionary stage. However, while CBSS show constant, long term hydrogen-burning, CNe burn hydrogen for only a few months, and in exceptional cases, a few years (GQ Mus, V723 Cas).

## Chapter 2

# Modeling Hot Atmospheres

### 2.1 Model Atmospheres

The calculation of model atmospheres involves the solution of the equations governing the stellar structure and the flow of radiation. One must make some simplifying assumptions to pursue self-consistent solutions. For example, we assume that the stellar photosphere is thin compared to the radius of the star ( $R$ ). In plane-parallel atmospheres this approximation is valid and the surface gravity can be considered constant. We assume the atmosphere is in steady-state, neglecting the effects of pulsation, shock, stellar wind, magnetic and tidal heating. It is in hydrostatic equilibrium, such that the pressure balances the gravity in every layer of the star. Also, the atmosphere is in radiative equilibrium, energy transportation is by convection and conduction or other means can be neglected, (Mihalas, 1970).

Computationally the problem is addressed in two basic iterative steps. First, one

finds the radiation field, determining the flow of radiation from the interior. Second, keeping the energy conserved (radiative equilibrium), one determines the structure and finds the corrections to the radiation field ( $\rho$ ,  $T$ ,  $P$ ). Repeating these steps iteratively until self-consistency is achieved gives a solution. The model atmosphere is given by the surface gravity  $g$ , the effective temperature  $T_{\text{eff}}$  and the chemical composition of the star. Assuming local thermodynamic equilibrium (LTE) makes the calculation much easier, because the total line opacity depends only on the local temperature, electron density and abundance. However, in the hot atmospheres of supersoft sources the photon mean free path is large in the extended low density atmosphere and this introduces non-LTE effects. The hot deep interior of the atmosphere is coupled with outer layers, changing their atomic level populations and ionization balance from the LTE values, (Hubeny and Lanz, 1995).

In general, a model calculation proceeds as shown in Figure 2.1. The effective temperature ( $T_{\text{eff}}$ ), the surface gravity ( $\log g$ ) and the atomic input data defines the atmosphere. In Figure 2.1 at the first step  $\epsilon_i$  means not only the atomic energy levels, but also the data for bound-free and bound-bound transitions and abundances of all species. The microturbulent velocity is  $\xi_{\text{turb}}$ . The first step is to estimate the temperature at the standard depth that is usually related to the effective temperature ( $T_{\text{std}} = 0.75T_{\text{eff}}$ ). One then solves the hydrostatic equilibrium equation:

$$\frac{dP}{dm} = g \tag{2.1}$$

where  $P$  is the total pressure, involving the ideal gas, radiation and microturbulent



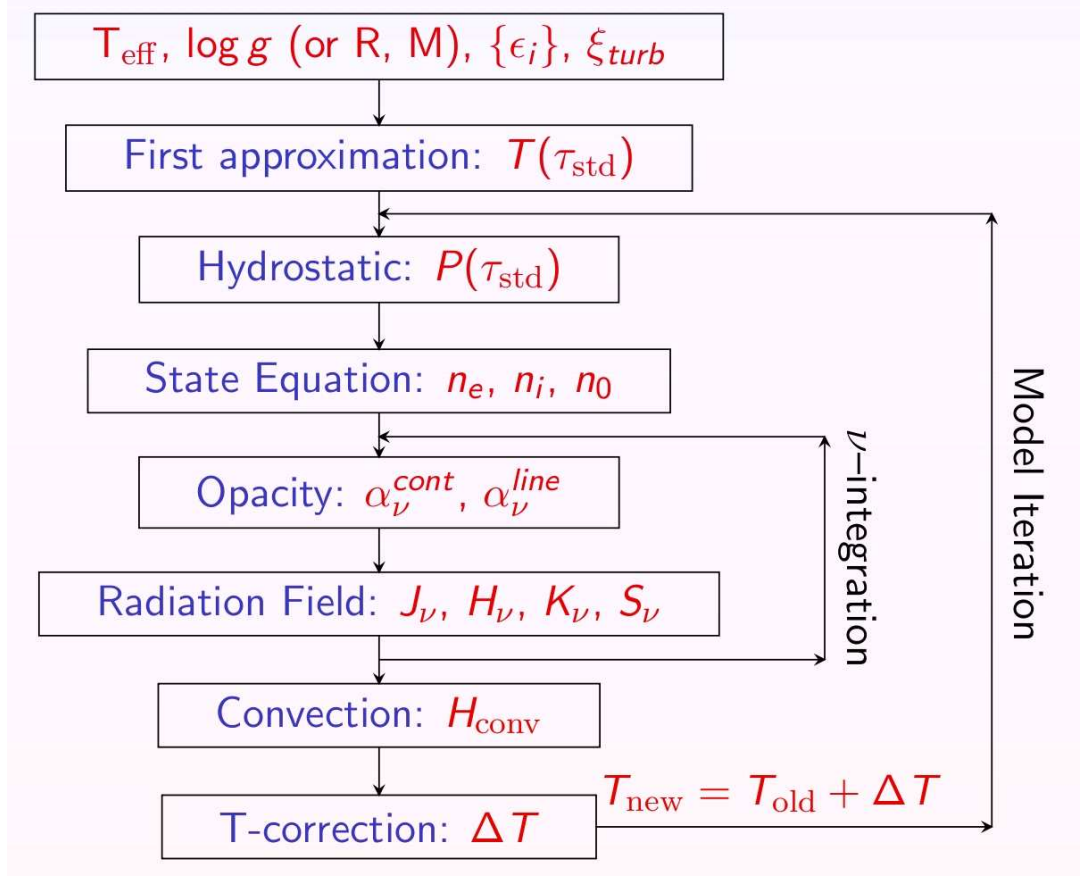


Figure 2.1: The main steps of model atmosphere calculation.

pressures,  $dm = -\rho dr$  is the Lagrangian mass,  $\rho$  is the density and  $dr$  is the geometrical vertical distance in the atmosphere. The gravitational acceleration,  $g = GM_\star/R_\star^2$  is assumed to be constant throughout the atmosphere,  $M_\star$  and  $R_\star$  are the mass and radius of the star, respectively.  $G$  is the gravitational constant. Level populations are determined by the statistical equilibrium equation, also called rate equation:

$$n_i \sum_{j \neq i} (R_{ij} + C_{ij}) = \sum_{j \neq i} n_j (R_{ji} + C_{ji}) \quad (2.2)$$

where  $n_i$  is the population of level  $i$ , and  $R_{ij}$  and  $C_{ij}$  are the radiative and collisional rate, respectively, for transitions from level  $i$  to level  $j$ . Radiative rates depend on radiation intensity and collisional rates are functions of local temperature and density. The set of rate equations for all levels of an atom would be a linearly dependent system. Therefore one equation of each set has to be replaced by the total particle number conservation equation or abundance definition equation  $\sum_i n_i = N_{atom}$ , summed over all levels of all ions of a given element. The radiative equilibrium equation expresses energy conservation, i.e. the absorbed and emitted energy must be the same everywhere in the atmosphere. In its most useful form this is, Hubeny and Lanz (1995):

$$\alpha \left[ \int_0^\infty (\kappa_\nu J_\nu - \eta_\nu) d\nu \right] + \beta \left[ \int_0^\infty \frac{d(f_\nu J_\nu)}{d\tau_\nu} d\nu - \frac{\sigma}{4\pi} T_{\text{eff}}^4 \right] = 0 \quad (2.3)$$

where  $\sigma$  is the Stefan-Boltzmann constant, and  $\kappa_\nu$  and  $\eta_\nu$  are the thermal absorption and emission coefficients, respectively. Scattering coefficients cancel out when coherent scattering may be assumed. The two terms of the equation are equivalent; the first is the integral form and the second is the differential. At large optical depths the differential form shows better numerical stability and higher accuracy, while at small optical depths the integral form is preferable. The two empirical parameters  $\alpha$  and  $\beta$  can have values between 0 and 1, and this sets the linear combination of the two forms. The flux is expressed by the variable Eddington factor  $f_\nu = K_\nu/J_\nu$ , where  $K_\nu$  is the flux, or second moment of the specific intensity and  $J_\nu$  is the mean intensity. For grey atmospheres the radiative equilibrium equation is solved with frequency independent opacities. The propagation of energy in the form of photons is expressed by the

radiative transfer equation:

$$\frac{d^2(f_\nu J_\nu)}{d\tau_\nu^2} = J_\nu - S_\nu \quad (2.4)$$

where  $\tau_\nu$  is the monochromatic optical depth. The Eddington factor  $f_\nu$  is not known but must be calculated by a separate set of formal solutions for the specific intensity, and iteratively updated using the current optical depth  $T_\nu$  and source function,  $S_\nu \equiv \eta_\nu/\kappa_\nu$ . The global electric neutrality of the medium is expressed by the charge conservation equation:

$$\sum_i n_i Z_i - n_e = 0 \quad (2.5)$$

where  $Z_i$  is the charge of level  $i$  (0 for neutrals, 1 for singly ionized, etc.) and  $n_e$  is the electron density.

The structural equations must be solved simultaneously at different layers of the atmosphere. This is done by the Hybrid CL/ALI method in TLUSTY. Before explaining these numerical methods, we first introduce the equations for LTE. Assuming LTE gives the starting values for non-LTE calculations. LTE is valid deep in the atmosphere, where due to high pressure, the free optical path of photons is small. In such an environment the level populations are determined by local conditions. The distribution of atoms among their bound states depends only on the local temperature  $T$ . This is expressed by the Boltzmann-equation:

$$\frac{N_{i,j}}{N_{0,j}} = \frac{g_i}{g_j} e^{-\chi/kT} \quad (2.6)$$

The distribution of ions depends on the temperature  $T$  and electron density  $n_e$ . This

is expressed by the Saha-Equation. In general the relative ionization fraction of any two states is:

$$\frac{N_{j+1}n_e}{N_j} = \left(\frac{2\pi mkT}{h^2}\right)^{3/2} \frac{2U_{j+1}(T)}{U_j(T)} e^{-\chi_I/kT} \quad (2.7)$$

where

$$U_j(T) = \sum_i g_i e^{\chi_I/kT} \quad (2.8)$$

is the partition function, and  $j$  is the degree of ionization. These equations can replace the rate equations (2.2) and the Planck function can be used for the source function in the transfer equation (2.4):

$$S_\nu = B_{\nu,T} = \frac{2h\nu^3}{c^2} \frac{1}{e^{\frac{h\nu}{kT}} - 1} \quad (2.9)$$

In general,  $T(\tau)$  does not satisfy the equations and one needs a correction term,  $\Delta T$  for the temperature. In this way, the whole problem is reduced to finding the correct temperature structure. The correction term  $\Delta T$  makes use of the difference between the computed values and the integrated flux  $F$ , as well as the change of total flux with optical depth  $dF/d\tau$  to force radiative equilibrium. Writing the temperature correction as:

$$T(\tau) = T_0(\tau) + \Delta T(\tau) \quad (2.10)$$

and using it in the radiative equilibrium:

$$\int_0^\infty k_\nu J_\nu d\nu = \int_0^\infty k_\nu S_\nu(T_0 + \Delta T) d\nu \quad (2.11)$$

the temperature correction has the form:

$$\Delta T = \frac{\int_0^\infty \kappa_\nu [J_\nu - B_\nu(T_0)] d\nu}{\int_0^\infty \kappa_\nu \frac{\partial B_\nu}{\partial T} d\nu} \quad (2.12)$$

With the altered temperature in the next iteration, and repeating the correction until the difference is small enough one can achieve a self-consistent solution.

## 2.2 TLUSTY and SYNSPEC

TLUSTY<sup>1</sup> (Hubeny and Lanz, 2003) is a program for calculating plane-parallel, horizontally homogeneous model stellar atmospheres in radiative and hydrostatic equilibrium following the steps in Figure 2.1. For a detailed description of the code see Hubeny (1988) and Hubeny and Lanz (1995). It solves the radiative transfer, hydrostatic, radiative and statistical equilibrium, charge and particle conservation equations using the Hybrid CL/ALI methods, a combination of the complete linearization (CL) and the Accelerated Lambda Iteration (ALI) methods. Beyond LTE, TLUSTY is also capable of calculating non-LTE models for a set of occupation numbers of selected atomic species and energy levels, and allows for convection. Starting with version 200, TLUSTY treats NLTE metal line blanketing with full consistency either using Opacity Distribution Functions (ODF) or Opacity Sampling (OS), (see Hubeny and Lanz (1995)).

An example TLUSTY input can be seen in Tables 2.1, 2.2 and 2.3. This file can

---

<sup>1</sup><http://nova.astro.umd.edu/index.html>

Table 2.1: First and second blocks of TLUSTY input.

---

700000.0 8.6	! TEFF; GRAV
F F	! LTE; LTGRAY
'flags'	! name of file containing non-standard flags
*	
* frequencies	
*	
500	! NFREAD
*	

---

be separated into four blocks. The first block defines  $T_{\text{eff}}$  and  $\log g$  of the atmosphere along with two switches that control whether LTE or non-LTE is preferred, and either grey or frequency-dependent model calculation is performed. In the third line one can pass an optional flag file to the program by which numerous (140) non-standard parameters can be changed. These parameters control additional physics and set different treatments of various processes and numerical methods in the calculation. The second input block is only one number, NFREAD. The program sets up continuum frequencies automatically and by default, two frequencies near discontinuities corresponding to the bound-free transitions from all explicit levels, plus NFREAD frequency points in between.

The third block is shown in Table 2.2. Here one can pass the list of atomic species included in the model. NATOMS is the highest atomic number considered in the model. MODE can have integer values between 0 and 2. If 0, the given atom is not considered at all. By setting it equal to 1, the element is taken into account in the particle and charge conservation equations, but not in line transitions. For MODE=2, the element is fully considered. ABN is the abundance. In this form it corresponds to

Table 2.2: Third block of TLUSTY input: explicit atoms.

---

```

* data for atoms
*
10                ! NATOMS
* mode abn  modpf
  2   1.   1     ! H
  2  1.e-1 1     ! He
  0   0   0     ! Li
  0   0   0     ! Be
  0   0   0     ! B
  2  1.e-2 1     ! C
  2  1.e-2 1     ! N
  2  1.e-2 1     ! O
  0   0   0     ! F
  2  1.e-3 1     ! Ne
*
*

```

---

the number ratio to the reference element,  $N_{\text{elem}}/N_{\text{H}}$ . If ABN is coded as negative, it corresponds to the relative solar abundance. MODPF is the mode of the evaluation of the partition function: 1 means to use Opacity Project ionization fraction tables, 0 is for standard evaluation (see Traving et al. 1966).

In the last block (2.3) one can set the data for ions. One line for each ionization level is considered in the model. IAT and IZ are the atomic number of the parent element and the charge of the ion, respectively. NLEVS is the number of atomic energy levels to be considered explicitly. The number of explicit levels can be lower than the energy levels in the model atom file. In this case only the lowest NLEVS levels will be included in the models. ILAST indicates if the given ion is the highest considered ionization degree of the given element. ILVIN changes the line treatment globally, all transitions related to energy levels with relative index smaller than ILVIN

Table 2.3: Fourth block of TLUSTY input: explicit ions.

---

```

* data for ions
*
* iat  iz   nlevs  ilast ilvlin  nonstd typion  filei
*
  1   0    9      0    90    0   ' H 1' 'data/h1x.dat'
  1   1    1      1     0    0   ' H 2' ' '
  2   1   20      0    90    0   'He 2' 'data/he2x.dat'
  2   2    1      1     0    0   'He 3' ' '
  6   4    5      0    90    0   ' C 5' 'data/c5.dat'
  6   5   10      0    90    0   ' C 6' 'data/c6.dat'
  6   6    1      1     0    0   ' C 7' ' '
  7   4    2      0    90    0   ' N 5' 'data/n5.dat'
  7   5    9      0    90    0   ' N 6' 'data/n6.dat'
  7   6   10      0    90    0   ' N 7' 'data/n7.dat'
  7   7    1      1     0    0   ' N 8' ' '
  8   5    5      0    90    0   ' O 6' 'data/o6.dat'
  8   6    9      0    90    0   ' O 7' 'data/o7.dat'
  8   7   10      0    90    0   ' O 8' 'data/o8.dat'
  8   8    1      1     0    0   ' O 9' ' '
 10   6    1      0     0    0   'Ne 7' 'data/ne7.dat'
 10   7    5      0    90    0   'Ne 8' 'data/ne8.dat'
 10   8    9      0    90    0   'Ne 9' 'data/ne9.dat'
 10   9   10      0    90    0   'Ne10' 'data/ne10.dat'
 10  10    1      1     0    0   'Ne11' ' '
  0   0    0     -1    0    0   '   ' ' '
*
* end

```

---

will be calculated in detailed radiative balance. This is used to calculate continuum-only models and neglects spectral lines. NONSTD is a flag, defining non-standard parameters for individual ions. These parameters must follow immediately after the block of the given ion. TYPION is a 10-character constant for ion identification. FILEI is the path to model atom data files. These data files were built in this work and will be described in more detail in Chapter 3.



## Complete linearization

Equations 2.1 – 2.5 are solved at discrete depths in the atmosphere and in numerous frequency points. These frequency points are carefully selected to represent the most important parts of the spectrum such as ionization edges, line centers and the wings of strong lines. A certain number of frequency points are also added equidistantly between these points. This yields a set of highly-coupled, non-linear equations. Complete linearization or CL, (Auer and Mihalas, 1969), was the first efficient and powerful method used to solve the structural equations simultaneously. The physical state of the atmosphere is described by a set of vectors  $\psi_d$  at each depth point  $d$ :

$$\psi_d = \{J_1, \dots, J_{NF}, N, T, N_e, n_1, \dots, n_{NL}\} \quad (2.13)$$

where  $J_i$  is the mean intensity of radiation at the  $i$ -th frequency point.  $N$ ,  $T$  and  $N_e$  are the number density, temperature and electron density at depth point  $d$ , respectively. The population of energy level  $i$  is  $n_i$ . In a model represented by  $NF$  number of frequency points and having  $NL$  atomic energy levels, the dimension of  $\psi_d$  is  $NN = NF + NL + 3$ . The number 3 stands for the three variables: number and electron density, and the temperature. The set of structural equations can be formally written as

$$P(\mathbf{x}) = 0 \quad (2.14)$$

where  $\mathbf{x}$  is the matrix formed from all state vectors,  $\mathbf{x} = \psi_1, \dots, \psi_{ND}$ . Equation 2.14 can be solved by the Newton-Raphson method:

$$\mathbf{x}^{(n+1)} = \mathbf{x}^{(n)} - J(\mathbf{x}^{(n)})^{-1} P(\mathbf{x}^{(n)}) \quad (2.15)$$

$J$  is the Jacobi matrix,  $J_{ij} = \partial P_i / \partial x_j$ . This represents a finite difference solution and Equation 2.14 reduces to:

$$-\mathbf{A}_d \delta \psi_{d-1} + \mathbf{B}_d \delta \psi_d - \mathbf{C}_d \delta \psi_{d+1} = \mathbf{L}_d \quad (2.16)$$

Here  $\mathbf{A}$ ,  $\mathbf{B}$  and  $\mathbf{C}$  are  $NN \times NN$  matrices, and  $\mathbf{L}_d = P_d(\mathbf{x}^{(n)})$  is defined as the residuum vector. Equation 2.16 is solved in place as a block-tridiagonal system. Only one  $NN \times NN$  matrix needs to be inverted at each depth point. Therefore, computing time scales as:

$$(NF + NL + 3)^3 \times ND \times N_{\text{iter}} \quad (2.17)$$

where  $N_{\text{iter}}$  is the number of iterations to solution. To accurately describe the radiation field it is necessary to work with  $10^4 - 10^5$  frequency points. From the computer time requirement it is clear that the complete linearization method in its original form is not practical on a single computer.

To optimize the CL method, TLUSTY utilizes some improvements over its original form. One of these improvements reduces the number of frequency points without compromising model accuracy. It is done by linearizing the mean intensities in the

most essential frequency points while keeping others fixed and updating them during a subsequent formal solution for one equation at a time for the current values of other variables. Another approach uses the multi-frequency/multi-gray method. In this method the frequency points for which the radiation forms in a similar way are grouped together, rearranging the  $NF$  frequency points into  $NB$  blocks, where  $NB \ll NF$ .  $\bar{J}_i$  represents the mean intensity typical for the  $i$ -th frequency block. These blocks do not need to be composed of continuous frequency intervals. For instance, one block can have all frequency points of the wings of weak lines, another the cores, and so on. The Accelerated Lambda Iteration is the most significant method, as it allows all the frequency points to be completely eliminated; more on this in the next section.

From Equation 2.17 it can be seen that  $NL$  also increases the cubic term. Significant improvement in computing speed can be achieved by reducing the number of energy levels, especially for heavy elements. Iron-peak elements can have thousands of levels per ion, and so the total number of levels can be comparable to the number of frequency points. The number of energy levels can be reduced by using simpler model atoms, including only the most important low-lying levels explicitly. The remaining levels can be taken in LTE through the partition function (Hubeny, 1988) or neglected, although the latter decreases accuracy. Another way to reduce the number of levels is to average individual levels into groups by their spectroscopic terms. Levels belonging to the same term share similar properties and can be averaged in multiplets. To further decrease the number of variables, individual levels or multiplets can be assigned to level groups. In this simplification, levels, in which populations can be assumed to

change in a coordinated way during linearization are grouped together. Then, instead of linearizing the individual level populations one needs to linearize only the entire population of the group. Level averaging and grouping was used in this work and is outlined in Chapter 3. Level zeroing is a numerical trick to decrease the sizes of matrices. If a level population falls to a negligible value, the population is set exactly to zero and the level is taken out of the calculations. This is also practical when one needs to include multiple ionization degrees in a model, the program will work only with those levels that contribute.

A much better approach to decrease the number of levels for heavy elements is to consider superlevels, (Hubeny and Lanz, 1995). Here many levels (50 – 100) are assigned to a superlevel assuming that each is in thermodynamic equilibrium and share the same non-LTE departure coefficient. There are two requirements for this: all levels belonging to a superlevel must have similar energies and the same parity. These two criteria assure that individual levels have indeed similar departure coefficients, and the same parity prevents transitions in a superlevel. This option was used only for iron in my work, but is available for any other species as well.

Further computational speed-up can be achieved by decreasing the number of depth points  $ND$  or the number of iterations  $N_{\text{iter}}$ . However, as timing is a linear function of these parameters, such an improvement is moderate. In hot atmospheres with line-blanketing many ionization degrees are present simultaneously and require many depth points making this option not feasible. To decrease the number of iterations TLUSTY uses Ng (Ng, 1974) and Kantorovich (Kantorovich, 1949) accelerations.

Both acceleration methods are described in Hubeny and Lanz (1992). These mathematical accelerations of convergence can significantly reduce the number of iterations, particularly for ALI. The Ng method uses information from earlier steps of the iteration. The Kantorovich method keeps the Jacobian in Equation 2.15 fixed after a certain number of iterations and re-evaluates only the residuum vector,  $\mathbf{L}_d$  in Equation 2.16. The number of iterations after which the Ng or Kantorovich acceleration is applied can be adjusted to the given model atmosphere by inspecting the convergence properties of the calculation. By default, TLUSTY uses an adjustable combination of the two methods. The Kantorovich acceleration starts after the 3rd iteration and refreshes the Jacobian after 3 iterations. Ng accelerations starts at the 7th iteration and is repeated after every 4 iterations.

## Accelerated Lambda Iteration

In Lambda Iteration the mean intensity is expressed as the product of the source function and the so-called Lambda operator:

$$J_\nu = \Lambda_\nu S_\nu \tag{2.18}$$

The iteration proceeds by consecutively updating the mean intensity using the previous source function and updating the new source function with the new mean intensity.

In LTE this is:

$$J_\nu^{(n)} = \Lambda_\nu S_\nu^{(n-1)} \quad (2.19)$$

$$S_\nu^{(n)} = (1 - \epsilon) J_\nu^{(n)} + \epsilon B_\nu \quad (2.20)$$

where  $\epsilon$  is the thermal coupling coefficient and  $B_\nu$  is the Planck function in LTE, and  $n$  is the iteration number. This procedure has slow convergence at large optical depths where  $\epsilon \approx 1$  and at high opacities. To avoid this, ALI uses operator splitting. The Lambda operator is written as:

$$\Lambda = \Lambda^* + (\Lambda - \Lambda^*) \quad (2.21)$$

where  $\Lambda$  and  $\Lambda^*$  are the exact and approximate Lambda operators, respectively. Both Lambda operators are valid for a specific frequency. With this, the mean intensity and source function have the form:

$$J_\nu^{(n)} = \Lambda_\nu^* S_\nu^{(n)} + (\Lambda_\nu - \Lambda_\nu^*) S_\nu^{(n-1)} \quad (2.22)$$

$$S_\nu^{(n)} = (1 - \epsilon) \Lambda_\nu^* S_\nu^{(n)} + (1 - \epsilon) (\Lambda_\nu - \Lambda_\nu^*) S_\nu^{(n-1)} + \epsilon B_\nu \quad (2.23)$$

The second correction term of the mean intensity is known from previous iterations. The first term represents an action of the approximate operator on the source function which is a function of temperature, density and level populations. In this way the radiative transfer equations are separated from the structural equations. The new

problem is to find a suitable approximate Lambda operator. Its form must give rise to a simpler matrix inversion while incorporating the essential properties of the original Lambda operator in order to reduce the necessary iterations. TLUSTY uses either the Rybicki-Hummer algorithm (Rybicki and Hummer, 1991), or the Olson-Kunasz operator (Kunasz and Olson, 1988) to determine  $\Lambda^*$ .

## Output

The main output of TLUSTY is the structure of the atmosphere, stored in an unformatted ASCII file. The first line contains the number of depth points and number of model parameters for a depth point. The following block is the depth grid, the column mass (in  $\text{g}/\text{cm}^2$ ) at each depth point. This is followed by the effective temperature, electron density, mass density and population numbers for all levels at each depth points. This output model can be used as an input for the next run of TLUSTY, or for calculating a synthetic spectrum with SYNSPEC. Also from this file it is possible to extract data for ionization balance and the structure of the atmosphere. In non-LTE mode the main output file is accompanied by an other file having the exact same structure, but listing the departure coefficients instead of occupation numbers.

## SYNSPEC

SYNSPEC<sup>2</sup> (Hubeny and Lanz, 2000) can work with a given model atmosphere, which either can be calculated by TLUSTY or a Kurucz model (ATLAS) taken from the

---

<sup>2</sup><http://nova.astro.umd.edu/Synspec43/synspec.html>

literature. The program reads a line list (see Appendix for O VI line list) and selects lines which contribute to the total opacity of the given atmosphere. Then it solves the radiative transfer equation (Equation 2.4), in a user-specified wavelength range and resolution and selects frequency points automatically. The program calculates the flux at the centers of two neighboring lines and in the midpoint between the two. Then it adds a certain number of frequency points equidistantly spaced between each pair to achieve the required resolution. In this way both the line centers and the continuum are sampled well. SYNSPEC is built in a similar way to TLUSTY and uses the same subroutines, but while TLUSTY calculates the model atmosphere self consistently and returns the structure and occupation numbers, SYNSPEC only recalculates the transfer equation and gives the detailed spectrum while considering natural, Stark and Van der Waals line broadening.

The calculated spectrum is the emergent flux versus wavelength at the top of the atmosphere ( $\tau_{\text{Ross}} = 10^{-7}$ ). SYNSPEC also provides the list of contributing spectral lines and their approximate equivalent widths. To compare this to observations one needs to take into account the effects of stellar rotation, interstellar absorption and convolve the data with the instrumental profile of the observing detector.



## Chapter 3

# Model Atoms

Model atoms are the primary data input for TLUSTY. These are the physical models of chemical species and their ions. This chapter describes the steps of constructing model atoms.

In order to model hot atmospheres one must include model atoms for all astrophysically important species and all of their ionization stages relevant to the work. TLUSTY itself is data independent, it has hard-coded data only for hydrogen and helium. Data for other elements must be communicated with model atom files. These files can be split into three main sections: data for energy levels, data for bound-free and bound-bound transitions.

In this work I closely followed the works of Ivan Hubeny and Thierry Lanz for sdB (Lanz and Hubeny, 2007) and sdO (Lanz and Hubeny, 2003) stars, the atomic data update of PHOENIX (Petz, 2005) and supersoft modeling of CAL 83 by Lanz et al. (2005). However, my approach differs from theirs in several ways. To keep TLUSTY

and SYNSPEC standard I did not modify the code, but extended the built-in atomic data arrays for higher ionization stages of all included metals. SYNSPEC version 48 has highest ionization degree of VII for all elements, except for Fe and Ni (for them it is X). I increased this limit to XXVI to consider all ionization degrees of all elements up to iron.

The challenge of modeling novae comes from the extreme conditions throughout the atmosphere. There is a large temperature gradient below the photosphere and outer layers of the atmosphere are radiatively heated. For this reason many ionization degrees are present, which increases the complexity and calculation time considerably. Another difficulty arises from the lack of reliable atomic data for high ionizations. The available data in the supersoft range is pretty much limited to TOPBASE<sup>1</sup> (Cunto et al., 1993), NIST<sup>2</sup>, APED<sup>3</sup> and Chianti<sup>4</sup> (Dere et al. (1997) and Dere et al. (2009)).

In the following I describe TOPBASE and NIST, from which I collected atomic data and recalculated them to model atom files that are readable by TLUSTY.

### 3.1 TOPbase

TOPbase is the atomic database of Opacity Project (OP), an international collaboration to calculate stellar envelope opacities by the *ab initio* methods of Seaton (1987). The prime initiative of the project was to provide atomic data to better understand pulsating stars. The aim was to tabulate accurate data on energy levels, oscillator

---

<sup>1</sup><http://cdsweb.u-strasbg.fr/topbase/topbase.html>

<sup>2</sup><http://www.nist.gov/physlab/data/asd.cfm>

<sup>3</sup><http://cxc.harvard.edu/atomdb/index.html>

<sup>4</sup><http://www.ukssdc.ac.uk/solar/chianti/>

strengths, photoionization cross-sections and line-broadening parameters for all contributing processes and astrophysically abundant ions. OP calculations were based on the close-coupling method of scattering theory. An N-electron system is described in terms of an N-1-electron target system and an active electron. The wave function of such a system is:

$$\Psi^{SL\pi} = \mathcal{A} \sum_i \chi_i \theta_i + \sum_i c_j \Phi_j \quad (3.1)$$

where  $\mathcal{A}$  is the antisymmetrisation operator,  $\chi_i$  is the target wave function and  $\theta_i$  is the active electron function. The  $\Psi_j$  are bound-state type functions for the total system, introduced to compensate for orthogonality conditions imposed on  $\theta_i$  and to render short-range correlations. Applying the Kohn variational principle (Kohn, 1996) with the functions  $\theta_i$  and coefficients  $c_j$  as variational parameters leads to a set of integro-differential equations which were solved numerically. In the calculations relativistic effects were neglected and LS-coupling was assumed. The close-coupling approximation addresses both electron correlations and threshold effects in the same framework, which allowed calculations of both bound-free and bound-bound transitions. This unique feature made OP data state-of-the-art for its time and it is still the most complete atomic data set for the supersoft range. The integro-differential equations were solved with the R-matrix method of Burke and Seaton (1971) and asymptotic techniques developed by Seaton (1985).

TOPbase has atomic data from Hydrogen to Silicon, for Sulfur, Argon, Calcium and Iron. The full content and data tables are available on-line at the Centre de Données Astronomiques de Strasbourg (CDS) under TIPTOPbase. The principal

and orbital angular momentum quantum numbers are limited to  $N \leq 10$  and  $l \leq 4$  respectively, except for hydrogenic ions  $N \leq 10$  and  $l \leq 9$ . The total data file is about 500 Mb. Table 3.1 shows a small subset of energy levels listed in TOPbase; here are shown the first 10 levels of N VI. These levels are actually spectroscopic terms, as TOPbase neglects hyperfine structure. The first column  $i$  is the ID number of the level in the current file,  $NZ$  and  $NE$  are the atomic number and the number of electrons. The spectroscopic term is expressed with the spin quantum number ( $S$ ), the orbital angular momentum quantum number ( $L$ ) and parity ( $P$ ) for level  $i$ :

$$SLP_i = (2S_i + 1) \cdot 100 + L_i \cdot 10 + P_i \quad (3.2)$$

Table 3.1: First ten energy levels of N VI in TOPbase.

$i$	$NZ$	$NE$	$iSLP$	$iLV$	$iCONF$	$E(RYD)$	$TE(RYD)$	$g_i$	$QD$	$EQN$	$RL(NS)$
...											
1817	7	2	100	1	1s2	-4.05249E+01	0.00000E+00	1.0	0.000E+00	0.9425	1.00E+30
1818	7	2	100	2	1s 2s	-9.22280E+00	3.13021E+01	1.0	2.431E-02	1.9757	1.00E+30
1819	7	2	100	3	1s 3s	-4.06733E+00	3.64576E+01	1.0	2.493E-02	2.9751	8.91E-02
1820	7	2	100	4	1s 4s	-2.27854E+00	3.82464E+01	1.0	2.513E-02	3.9749	1.31E-01
1821	7	2	100	5	1s 5s	-1.45466E+00	3.90702E+01	1.0	2.526E-02	4.9747	2.08E-01
1822	7	2	100	6	1s 6s	-1.00849E+00	3.95164E+01	1.0	2.531E-02	5.9747	3.19E-01
1823	7	2	100	7	1s 7s	-7.40041E-01	3.97849E+01	1.0	2.533E-02	6.9747	4.71E-01
1824	7	2	100	8	1s 8s	-5.66081E-01	3.99588E+01	1.0	2.534E-02	7.9747	6.69E-01
1825	7	2	100	9	1s 9s	-4.46959E-01	4.00779E+01	1.0	2.535E-02	8.9746	9.20E-01
1826	7	2	100	10	1s10s	-3.61833E-01	4.01631E+01	1.0	2.536E-02	9.9746	1.23E+00
...											

The next column,  $iLV$ , is the level index for a spectroscopic term, followed by its configuration. Columns seven and eight list the energy of the level in Rydbergs with respect to the ionization energy and to the ground level, respectively. The last columns are the statistical weight of the term ( $g_i$ ), quantum defect ( $QD$ ), effective

Table 3.2: First two entries of photoionization cross-sections for N VI. Only the first five data points are listed for each level.

I	NZ	NE	ISLP	ILV	E(RYD)	NP
56	7	2	100	1	-4.05249E+01	62
					4.022729E+01	3.490E-01
					4.030170E+01	3.475E-01
					4.037610E+01	3.460E-01
					4.045039E+01	3.445E-01
					4.052451E+01	3.431E-01
...						
57	7	2	100	2	-9.22280E+00	62
					8.925290E+00	4.156E-01
					8.999670E+00	4.089E-01
					9.074050E+00	4.024E-01
					9.148430E+00	3.960E-01
					9.222450E+00	3.898E-01
...						

quantum number ( $EQN$ ) and radiative lifetime ( $RL$ ) in nanoseconds.

Table 3.2 illustrates the photoionization data. Here, only five cross section values are shown for the first two levels. For each level the first number ( $I$ ) is the level index in the given file,  $NZ$ ,  $NE$ ,  $ISLP$ ,  $ILV$  and  $E$  has the same meaning as before. For each level the first line is followed by  $NP$  number of data pairs of wavenumber (in  $\text{cm}^{-1}$ ) and cross section (in Mb).

Table 3.3: First ten lines of  $f$ -values data for N VI.

i	NZ	NE	iSLP	jSLP	iLV	jLV	iCONF	jCONF	gF	gA(S-1)	WL(A)	g1	gJ
331	7	2	111	100	1	1	1s 2p	1s2	6.74E-01	5.41E+12	2.883E+01	3.0	1.0
332	7	2	111	100	1	2	1s 2p	1s 2s	7.69E-02	5.79E+07	2.977E+03	3.0	1.0
333	7	2	111	100	1	3	1s 2p	1s 3s	-5.94E-02	-1.12E+10	1.879E+02	3.0	1.0
334	7	2	111	100	1	4	1s 2p	1s 4s	-1.28E-02	-4.53E+09	1.373E+02	3.0	1.0
335	7	2	111	100	1	5	1s 2p	1s 5s	-5.03E-03	-2.25E+09	1.221E+02	3.0	1.0
336	7	2	111	100	1	6	1s 2p	1s 6s	-2.55E-03	-1.28E+09	1.152E+02	3.0	1.0
337	7	2	111	100	1	7	1s 2p	1s 7s	-1.49E-03	-8.00E+08	1.115E+02	3.0	1.0
338	7	2	111	100	1	8	1s 2p	1s 8s	-9.50E-04	-5.32E+08	1.091E+02	3.0	1.0
339	7	2	111	100	1	9	1s 2p	1s 9s	-6.46E-04	-3.72E+08	1.076E+02	3.0	1.0
340	7	2	111	100	1	10	1s 2p	1s10s	-4.60E-04	-2.70E+08	1.065E+02	3.0	1.0
...													

Table 3.3 contains radiative data for NVI. The first nine columns identify the transition using the same entries that are also listed in Table 3.1. Oscillator strength

$(gF_{ij})$  is multiplied by  $g_i$ , the statistical weight of level  $i$ . Transitions from higher to lower levels (emission) are taken as positive. Similarly, Einstein coefficients ( $A_{ij}$ ) are also multiplied by the statistical weight and emission lines are taken as positive. Wavelength calculated from the energy difference of the levels involved ( $WL$ ) is listed in Ångströms.

## 3.2 NIST/ASD

National Institute of Standards and Technology (NIST) is a measurement standards laboratory in Gaithersburg, Maryland. NIST has been collecting data, maintains and publishes scientific and technical databases. One of these databases is the Atomic Spectra Database (ASD), which contains data for radiative transitions and energy levels in atoms and atomic ions. Data are included for observed transitions of 99 elements and energy levels of 52 elements. ASD contains data for about 900 spectra from 1 Ångström to 200  $\mu\text{m}$ , with about 70,000 energy levels and 91,000 lines, 40,000 of which have transition probabilities listed. Its convenient, html interface allows for interactive data collection and download as ASCII tables, as shown in Table 3.4. Levels are listed with increasing energy with respect to the ground level and identified by their configurations, spectroscopic terms and total electronic angular-momentum quantum number ( $J$ ). Level energies and splittings are given in  $\text{cm}^{-1}$  units.

Table 3.5 is an example of line data in NIST/ASD. Observed wavelengths are tabulated if either or both energy levels of the transition are unavailable. In most cases wavelength is calculated from the energy difference of the two levels (these are

Table 3.4: First 10 energy levels of NVI in NIST/ASD.

Configuration	Term	J	Level (cm-1)	Splitting (cm-1)
1s2	1S	0	0	
1s.2s	3S	1	3385890	3385890
1s.2p	3P*	0	3438304	52414
		1	3438320	16
		2	3438610	290
1s.2s	1S	0	3439274	664
1s.2p	1P*	1	3473790	34516
1s.3s	3S	1	3991860	518070
1s.3s	1S	0	4006000	14140
1s.3p	3P*	0	4006160	160
		2	4006160	0
		1	4006160	0
1s.3d	3D	3	4013460	7300
		2	4013460	0
		1	4013460	0
1s.3d	1D	2	4013770	310
...				

the Ritz wavelengths). All wavelengths are given for vacuum. Relative intensities are tentative and serve as identifications only. Einstein coefficients  $A_{ki}$  are derived from lifetime measurements. Oscillator strengths are calculated:

$$f_{ik} = \frac{m_e c \epsilon_0 \lambda^2}{2\pi e^2} A_{ki} \frac{g_k}{g_i} \quad (3.3)$$

where  $g_x = 2J_x + 1$ . The transition strength is also function of  $A_{ki}$ :

$$S_{ik} = \frac{3h\epsilon_0\lambda^3 g_k}{16\pi^3} A_{ki} \quad (3.4)$$

### 3.3 TOPAtom

Building model atoms from TOPbase and NIST/ASD data tables is done through several steps. Each of these is written in short modules of Python scripts, which are called by a top-level program, TOPAtom. The simple command line program can be invoked with flags setting various treatments, or formats of the output.

The first task is to extract level configurations, terms, total electronic angular-momentum quantum numbers and energies from both NIST/ASD and TOPbase. These levels are then cross-correlated. Because calculated and observed data are different, levels are identified according to their configuration and term, instead of their energies or wavelengths. Both datasets provide only the significant part of the configuration. To convert them to the same format I rebuilt the full configuration and stored it in a 36 character string variable. For example, for a level of Ca XII NIST provides the configuration  $2s2p^5(^3P_o)3s$ ; in my level list this level has the configuration: `1s2.2s.2p5.(3P0).3s_____`. In the correlation work all NIST levels are kept and the list is completed with TOPbase data. With the level list generated, the next step is to generate a new dataset for transitions. The levels can be combined with selection rules considered, although NIST has data for forbidden transitions as well, so currently all linear combinations of the levels are considered. This increases the size of the transition file and the computational time, but does not skip any transitions. The transition list contains level energies, configurations, terms,  $J_s$ , level database indices (NIST or TOPbase) and the wavelengths of the transitions. This is the input for the next step, where the program cross-correlates the databases



and assigns transition strengths and transition probabilities to level pairs.

There are three data sets for the transitions: the previously described transition list, the  $f$ -values data from TOPbase, and data for lines from NIST. The latter two are converted to the same data format with the first. Correlation is done by taking each data entry in the transition file and assigning oscillator strengths and transition probabilities to them from NIST lines. Upon finding missing data in NIST, it is taken from TOPbase. If the given entry is missing from both databases the transition is dropped. This way it is possible to assign TOPbase oscillator strengths and transition probabilities to the more accurate NIST levels. Correlated results are stored in transition files `f77united_list.ion` for each ion. An example for N VI is shown in Table 3.6. Each line of the file describes one transition including oscillator strengths and transition probabilities.

### Line list

The transition files are actually line lists, they can be easily reformatted for SYNSPEC. The files are read in line by line and written to `gfXRA.ion` files like in Table 3.7 for N VI. Then these files are merged and sorted by wavelength. Currently the line list contains 380,092 lines without iron, in the supersoft range ( $10 \text{ \AA} - 100 \text{ \AA}$ ) there are 77,299 lines with oscillator strengths and natural broadening coefficients. The structure of the file follows those of the original SYNSPEC line lists for ultraviolet and optical. The first column is the wavelength in nm. The code of the ion is listed in the second column in the form  $(NZ).(NZ - NE)$ , where  $NZ$  is the atomic number

Table 3.5: Example for NIST lines data for N VI.

Observed Wavelength Vac (Å)	Ritz Wavelength Vac (Å)	Rel. Int. (?)	Aki s <sup>-1</sup>	fik	S	log-gf	Acc.	Ei (cm-1)	Ek (cm-1)	Configurations	Terms	Ji	Jk	gi	gk	Type
23.0240	23.0240	1.500e+10	6.290e+10	1.500e-02	1.137e-03	-1.824	AA	0	4343290	1s2 - 1s.6p	1S - 1P*	0 - 1	0 - 1	1 - 3	1 - 3	M1
23.2770	23.2770	1.091e+11	1.091e+11	2.659e-02	2.037e-03	-1.575	AA	0	4296090	1s2 - 1s.5p	1S - 1P*	0 - 1	0 - 1	1 - 3	1 - 3	M1
23.7710	23.7710	2.145e+11	2.145e+11	5.451e-02	4.266e-03	-1.263	AA	0	4206810	1s2 - 1s.4p	1S - 1P*	0 - 1	0 - 1	1 - 3	1 - 3	M1
23.8277	23.8277	4.59e+01	4.59e+01	1.17e-11	6.91e-08	-10.931	C	0	4196800	1s2 - 1s.4s	1S - 3S	0 - 1	0 - 1	1 - 3	1 - 3	M1
24.8980	24.8980	5.158e+11	5.158e+11	1.438e-01	1.179e-02	-0.842	AA	0	4016390	1s2 - 1s.3p	1S - 1P*	0 - 1	0 - 1	1 - 3	1 - 3	M1
24.9142	24.9142	3.847e+07	3.847e+07	1.790e-05	1.649e-03	-4.747	AA	0	4013770	1s2 - 1s.3d	1S - 1D	0 - 2	0 - 2	1 - 5	1 - 5	E2
26.0510	26.0510	8.36e+01	8.36e+01	2.36e-11	1.46e-07	-10.627	C	0	3991860	1s2 - 1s.3s	1S - 3S	0 - 1	0 - 1	1 - 3	1 - 3	M1
28.7870	28.7870	1.809e+12	1.809e+12	6.742e-01	6.390e-02	-0.171	AA	0	3473790	1s2 - 1s.2p	1S - 1P*	0 - 1	0 - 1	1 - 3	1 - 3	M2
29.0815	29.0815	1.03e+05	1.03e+05	6.53e-08	1.62e+00	-7.185	A	0	3438610	1s2 - 1s.2p	1S - 3P*	0 - 2	0 - 2	1 - 5	1 - 5	M1
29.5343	29.5343	2.55e+02	2.55e+02	1.00e-10	7.31e-07	-10.000	A+	0	3385890	1s2 - 1s.2s	1S - 3S	0 - 1	0 - 1	1 - 3	1 - 3	M1
104.884	104.884	1.58e+09	1.58e+09	7.82e-03	2.70e-03	-2.107	A	3439274	4392710	1s.2s - 1s.8p	1S - 1P*	0 - 1	0 - 1	1 - 3	1 - 3	M1
107.151	107.151	2.31e+09	2.31e+09	1.19e-02	4.21e-03	-1.823	A	3439274	4372540	1s.2s - 1s.7p	1S - 1P*	0 - 1	0 - 1	1 - 3	1 - 3	M1
110.618	110.618	3.642e+09	3.642e+09	2.004e-02	7.299e-03	-1.698	AA	3439274	4343290	1s.2s - 1s.6p	1S - 1P*	0 - 1	0 - 1	1 - 3	1 - 3	M1
116.711	116.711	6.275e+09	6.275e+09	3.844e-02	1.477e-02	-1.415	AA	3439274	4296090	1s.2s - 1s.5p	1S - 1P*	0 - 1	0 - 1	1 - 3	1 - 3	M1
116.786	116.786	7.460e+09	7.460e+09	4.576e-02	1.759e-02	-1.339	AA	3438304	4294570	1s.2p - 1s.5d	3P* - 3D	0 - 1	0 - 1	1 - 3	1 - 3	M1

Table 3.6: Example for transitions in f77united\_list.n6, for N VI. Level configurations are stored in a 36 character string variable, here it is trimmed to 20.

NZ	ME	Fij	Level i (m-1)	Level j (m-1)	Configuration i	Configuration j	Ji	Jj	ISLP	JSLP	Level i	Level j	Aji	Tr. id
7	2	0.150000E-01	0.000000000	4343290.000000000	1s2.....1s.6p	1s2.....1s.6p	0.0	1.0	100	111	MIST	MIST	0.629000E+11	M1str 1
7	2	0.265900E-01	0.000000000	4296090.000000000	1s2.....1s.5p	1s2.....1s.5p	0.0	1.0	100	111	MIST	MIST	0.109100E+12	M1str 1
7	2	0.545100E-01	0.000000000	4206810.000000000	1s2.....1s.4p	1s2.....1s.4p	0.0	1.0	100	111	MIST	MIST	0.214500E+12	M1str 1
7	2	0.117000E-10	0.000000000	4196800.000000000	1s2.....1s.4s	1s2.....1s.4s	0.0	1.0	100	300	MIST	MIST	45.9000	M1str 1
7	2	0.143800	0.000000000	4016390.000000000	1s2.....1s.3p	1s2.....1s.3p	0.0	1.0	100	111	MIST	MIST	0.515800E+12	M1str 1
7	2	0.179000E-04	0.000000000	4013770.000000000	1s2.....1s.3d	1s2.....1s.3d	0.0	2.0	100	120	MIST	MIST	0.384700E+08	M1str 1
7	2	0.236000E-10	0.000000000	3991860.000000000	1s2.....1s.3s	1s2.....1s.3s	0.0	1.0	100	300	MIST	MIST	83.6000	M1str 1
7	2	0.674200	0.000000000	3473790.000000000	1s2.....1s.2p	1s2.....1s.2p	0.0	1.0	100	111	MIST	MIST	0.180900E+13	M1str 1
7	2	0.653000E-07	0.000000000	3438610.000000000	1s2.....1s.2s	1s2.....1s.2s	0.0	2.0	100	311	MIST	MIST	103000.	M1str 1
7	2	0.100000E-09	0.000000000	3385890.000000000	1s2.....1s.2s	1s2.....1s.2s	0.0	1.0	100	300	MIST	MIST	255.000	M1str 1
7	2	0.674000	0.000000000	3473790.000000000	1s2.....1s.2p	1s2.....1s.2p	0.0	1.0	100	111	MIST	MIST	0.541000E+13	TBtr 2
7	2	0.144000	0.000000000	4016390.000000000	1s2.....1s.3p	1s2.....1s.3p	0.0	1.0	100	111	MIST	MIST	0.154000E+13	TBtr 2
7	2	0.545000E-01	0.000000000	4206810.000000000	1s2.....1s.4p	1s2.....1s.4p	0.0	1.0	100	111	MIST	MIST	0.642000E+12	TBtr 2
7	2	0.265000E-01	0.000000000	4296090.000000000	1s2.....1s.5p	1s2.....1s.5p	0.0	1.0	100	111	MIST	MIST	0.325000E+12	TBtr 2
7	2	0.150000E-01	0.000000000	4343290.000000000	1s2.....1s.6p	1s2.....1s.6p	0.0	1.0	100	111	MIST	MIST	0.188000E+12	TBtr 2

and  $NE$  is the number of electrons. The third column lists  $\log(g_i f_{ij})$ , followed by the excitation potential (in  $\text{cm}^{-1}$ ) and the  $J$  quantum number of the lower and the upper level. The eighth column has data for natural broadening  $\log(A_{ji})$ , followed by coefficients for Stark and Van der Waals broadening which are in this case set to taken with their classical expression. The eleventh column is a flag indicating that there are no more records for the given line. The last column is a comment indicating which database the oscillator strength and natural broadening were taken from.

Table 3.7: N VI line list up to 100 Å.

2.2688	07.05	-2.983	0.000	0.0	4407643.300	1.0	10.13	0.00	0.00	0	!TBtr
2.2736	07.05	-2.844	0.000	0.0	4398403.418	1.0	10.27	0.00	0.00	0	!TBtr
2.2765	07.05	-2.688	0.000	0.0	4392710.000	1.0	10.42	0.00	0.00	0	!TBtr
2.2870	07.05	-2.510	0.000	0.0	4372540.000	1.0	10.59	0.00	0.00	0	!TBtr
2.3024	07.05	-1.824	0.000	0.0	4343290.000	1.0	10.80	0.00	0.00	0	!NISTtr
2.3277	07.05	-1.575	0.000	0.0	4296090.000	1.0	11.04	0.00	0.00	0	!NISTtr
2.3771	07.05	-1.264	0.000	0.0	4206810.000	1.0	11.33	0.00	0.00	0	!NISTtr
2.3828	07.05	-10.932	0.000	0.0	4196800.000	1.0	1.66	0.00	0.00	0	!NISTtr
2.4898	07.05	-0.842	0.000	0.0	4016390.000	1.0	11.71	0.00	0.00	0	!NISTtr
2.4914	07.05	-4.747	0.000	0.0	4013770.000	2.0	7.59	0.00	0.00	0	!NISTtr
2.5051	07.05	-10.627	0.000	0.0	3991860.000	1.0	1.92	0.00	0.00	0	!NISTtr
2.8787	07.05	-0.171	0.000	0.0	3473790.000	1.0	12.26	0.00	0.00	0	!NISTtr
2.9082	07.05	-7.185	0.000	0.0	3438610.000	2.0	5.01	0.00	0.00	0	!NISTtr
2.9534	07.05	-10.000	0.000	0.0	3385890.000	1.0	2.41	0.00	0.00	0	!NISTtr
9.7408	07.05	-2.444	3385890.000	1.0	4412500.000	2.0	8.93	0.00	0.00	0	!TBtr
9.8308	07.05	-2.301	3385890.000	1.0	4403100.000	2.0	9.06	0.00	0.00	0	!TBtr
9.9501	07.05	-2.135	3385890.000	1.0	4390900.000	2.0	9.22	0.00	0.00	0	!TBtr
...											

## Atoms – Levels

Model atoms are derived from the same transition files. At the first step all levels with configurations and term designations were extracted. These levels then were listed according to TLUSTY input format shown in Table 3.8. The principal quantum number ( $N$ ) of each level is taken as the principal quantum number of the highest orbit in the configuration. Level grouping is automatic for  $N \geq 3$ . Each level is appended

by a level index, spectroscopic term, level energy in  $1000 \text{ cm}^{-1}$  and database ID as comments at the end of the lines.

Table 3.8: First ten energy levels of N VI.

***** Levels						
1.334899368397e+17	1.	1	'_____1s2'	0	0.	0 ! 1 1Se 0.0 NIST
3.198350827796e+16	3.	2	'_____1s.2s'	0	0.	0 ! 2 3Se 3385.89 NIST
3.041217608860e+16	1.	2	'_____1s.2p'	0	0.	0 ! 3 3Po 3438.304 NIST
3.041169642066e+16	3.	2	'_____1s.2p'	0	0.	0 ! 4 3Po 3438.32 NIST
3.040300243938e+16	5.	2	'_____1s.2p'	0	0.	0 ! 5 3Po 3438.61 NIST
3.038309622017e+16	1.	2	'_____1s.2s'	0	0.	0 ! 6 1Se 3439.274 NIST
2.934833257214e+16	3.	2	'_____1s.2p'	0	0.	0 ! 7 1Po 3473.79 NIST
1.381698470053e+16	3.	3	'_____1s.3s'	0	0.	-103 ! 8 3Se 3991.86 NIST
1.339307816492e+16	1.	3	'_____1s.3s'	0	0.	-103 ! 9 1Se 4006.0 NIST
1.338828148559e+16	1.	3	'_____1s.3p'	0	0.	-103 ! 10 3Po 4006.16 NIST
...						

### Atoms – Bound-free transitions

Bound-free transitions are from the TOPbase  $x$ -data. Table 3.2 shows the content of these files. Levels can be identified by level indices, which can be matched with indices in the TOPbase level data. But, instead of tracking these back to find the configuration, I chose to find levels based on energy and terms. The previous level list is the basis for this search. For each level the program seeks levels in the cross section data with the same term and within an energy difference of 1%, 5%, 25% and 100%. This way the search returns cross section data for all TOPbase levels and accuracy can be tracked for NIST levels. Levels not having cross section data in TOPbase or outside acceptable limits are taken in hydrogenic approximation.

Once photoionization data is assigned to a given level, the frequency and cross section columns are written into separate files. This data set can be very extensive for TLUSTY. Thus, they need to be resampled, smoothed or fitted. TOPAtom has

three modes to do this. The first one uses the analytic functions and coefficients for ground states from Verner et al. (1996). These are adequate only for the highest ionization states. With more electrons and more complex resonance structure these analytic functions do not fit the data. The second treatment is the Resonance Averaged Photoionization Cross-section (RAP) mode as prescribed by Bautista et al. (1998). The cross section is convolved with a Gaussian at constant resolution  $\delta E/E$ :

$$\sigma_A(E) = C \int_{E-5\delta E}^{E+5\delta E} \sigma(x) e^{-\frac{(x-E)^2}{2(\delta E)^2}} dx \quad (3.5)$$

where  $\sigma$  and  $\sigma_A$  are the detailed and averaged photoionization cross sections, respectively, and  $C$  is a normalizing constant. At high energies the resolution  $\delta E/E = 0.01$  gives reasonable results, both the general run of the function as well as resonances are represented well, as shown in Figure 3.1 for Mg VIII and Figure 3.2 for O V.

It is also possible to manually select representative data points. In this mode TOPAtom plots the graph of the cross-section and the user can select data points by mouse clicks. This mode allows full control by the user, but would make fitting hundreds of levels a tedious work, and so was not used here. Once the resampled cross section is available it is written to the model atom file.

### **Atoms – Bound-bound transitions**

Bound-bound transitions are built based on the level list. Taking the first level and forming level pairs with each higher level gives the transitions. If the level pair can be found in the transition file its oscillator strength is taken in a primarily ALI transition

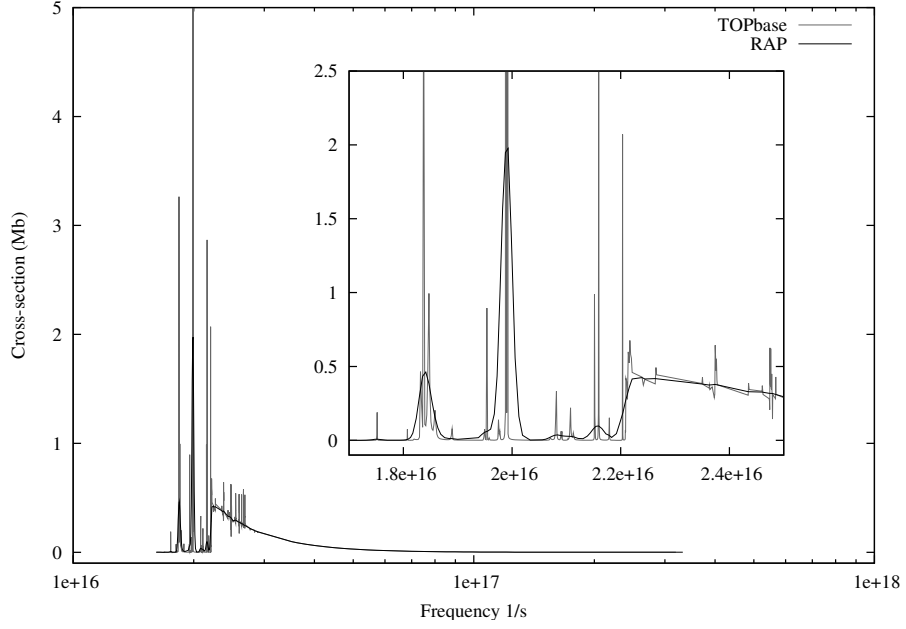


Figure 3.1: Photoionization cross-section of Mg VIII  $1s^2 2s 2p(^1P_o) 3d$  level (grey) and its resonance averaged representation (black).

with Doppler profile. The collisional rate is evaluated by Van Regemorter's formula (Equation 3.6) with  $\bar{g} = 0.2$  for transitions  $nl \rightarrow n'l'$  (where  $n \neq n'$ ) and  $\bar{g} = 0.7$  if  $nl \rightarrow nl'$ .

$$\Omega = 19.7363 f_{ij} T^{-3/2} U_0^{-1} \exp(-U_0) \max[\bar{g}, 0.276 \exp(U_0) E_1(U_0)] \quad (3.6)$$

where  $U_0 = (E_j - E_i)/(kT)$ ,  $E_i$  and  $E_j$  are the energies of the lower and upper levels,  $T$  is the temperature and  $f_{ij}$  is the oscillator strength.  $E_1(U_0)$  is the first exponential integral function:

$$E_1(U_0) = \int_{U_0}^{\infty} \frac{e^{-t}}{t} dt \quad (3.7)$$

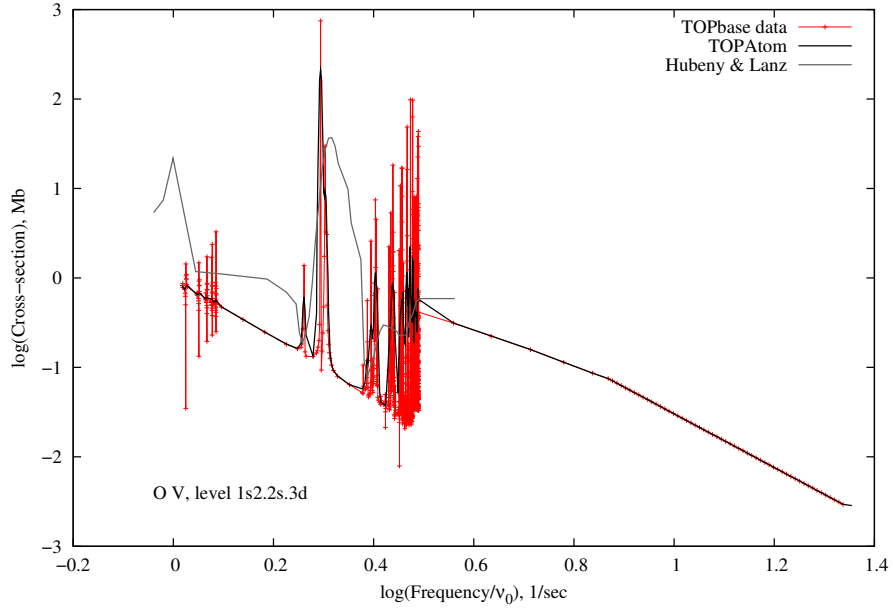


Figure 3.2: Photoionization cross-section of the O V,  $1s2.2s.3d$  level.  $\nu_0$  is the ionization edge frequency. The original data consists of 967 data points and are shown here in red. The TOPAtom RAP smoothed data is black, it has 192 data points. For comparison the cross-section from TLUSTY’s web site is plotted with grey.

If the transition is neither in NIST nor in TOPbase its oscillator strength is set to “scaled hydrogenic”. These lines are then treated in detailed radiative balance with Doppler profiles and collisional rates are evaluated by the Eissner-Seaton formula (Equation 3.8) with  $c_0 = 0.05$ :

$$\Omega = 8.631 \cdot 10^{-6} g_i^{-1} T^{-1/2} \exp(-U_0) c_0 \quad (3.8)$$

where  $g_i$  is the statistical weight of level  $i$ .

Table 3.9: First ten transitions of N VI.

---

```

*** Line transitions
1 2          -1 0 1 0 0      1.0000e-10 2.000e-01
  F 1 7 0. 0.
1 3          0 0 4 0 0      0.0000e+00 5.000e-02
1 4          0 0 4 0 0      0.0000e+00 5.000e-02
1 5          -1 0 1 0 0      6.5300e-08 2.000e-01
  F 1 7 0. 0.
1 6          0 0 4 0 0      0.0000e+00 5.000e-02
1 7          -1 0 1 0 0      6.7420e-01 2.000e-01
  F 1 7 0. 0.
1 8          -1 0 1 0 0      2.3600e-11 2.000e-01
  F 1 7 0. 0.
1 9          0 0 4 0 0      0.0000e+00 5.000e-02
1 10         0 0 4 0 0      0.0000e+00 5.000e-02
...

```

---

### Averaged model atoms

The detailed model atom output of TOPAtom is readable by TLUSTY in theory, although very extensive. The few hundred energy levels and thousands of transitions would make model calculations very ineffective and impractical. For this reason, it is necessary to reduce the number of levels to a few dozen. This is also done with TOPAtom. Levels can be grouped according to their principal quantum number, their spectroscopic terms or any other user-defined way. TOPAtom needs only the level indices rearranged into groups and does the averaging automatically. In the first step it calculates the weighted average of all levels in a group using the energies and statistical weights of the individual levels. Autoionizing levels included in TOPbase are also incorporated in model atom files; they are listed separately, as negative levels.

Bound-free transitions require a bit more attention. These are given with a few hundred data points of the RAP cross-sections for each individual transition. First



the frequencies are collected from all the cross-sections belonging to a new level group. This gives the frequency points of the averaged cross-section. This scale is trimmed to the shortest data set to avoid spurious extrapolations. Following this, each cross-section data set is interpolated to the new frequency points and their weighted average is calculated. This way every feature of the cross-section is considered. The procedure returns a large number of close lying data points as well. To sort out unnecessary data points a filtering is applied for each cross-section. First, the total frequency range is divided into 1000 bins. Then the relative change is calculated between adjacent data points; if this is below 0.001 the data point is considered unnecessary and gets deleted. The first and last data points are always kept. This way the data is sampled with many data points where the cross section changes fast and only by a few in the smooth parts, such as the high energy tails.

Transitions are averaged according to Equation 3.9, where  $\bar{\lambda}_{ik}$  is the wavelength of the averaged transition:

$$f_{ik}^{\text{multiplet}} = \frac{\sum_{J_i, J_k} (2J_i + 1) \lambda(J_i, J_k) f(J_i, J_k)}{\bar{\lambda}_{ik} \sum_{J_i} (2J_i + 1)} = \frac{\sum_{i,k} g_i \lambda_{ik} f_{ik}}{\bar{\lambda}_{ik} \sum_i g_i} \quad (3.9)$$

## Hydrogen and Helium

Hydrogen and helium have no spectral lines in the soft X-rays and the energies considered in my work exceeds their highest ionization degree in most of the atmosphere. They are important because they are abundant and provide reference species. Hydrogen and helium are well-described and incorporated in TLUSTY and SYNSPEC

by default. For this reason I used the hard-coded atomic data and model atoms from TLUSTY's web page.

The hydrogen model atom is adopted from Lanz and Hubeny (2003) sdO grid (OSTAR2002). It consists of the eight lowest levels and one superlevel merging higher excitation levels from  $N = 9$  to 80, in this model atom Lyman and Balmer series are included with approximate Stark profiles and all other lines have Doppler profiles. Hydrogen is considered in detailed balance in my NLTE-C and NLTE-L models.

Similarly to hydrogen, helium is also taken from OSTAR2002 model grid. He I consists of 19 individual levels up to  $N = 4$  and five averaged levels up to  $N = 8$ . Although He I is somewhat populated in hot models, to avoid convergence problems it was not always included. He II has 20 levels up to  $N = 20$ .

I updated my line list for SYNSPEC and included all hydrogen and helium lines from 880 Å to 7500 Å from the line lists provided on TLUSTY's page. These 1715 lines have no significance in this work, but they are included to keep the line list consistent with the model atoms.

## **Carbon, Nitrogen and Oxygen**

NIST has abundant data on energy levels and a significant number of transitions for C, N and O. Only the highest energy levels were taken from TOPbase. This means at least one level was taken from NIST for each transition, which improves the accuracy of the wavelengths of individual lines. Model atoms for these light metals are published from neutrals up to lithium-like ions. I built helium-like and hydrogenic model atoms

for all three species and lithium-like ions of carbon and oxygen for verification of my code. The O VI model atom can be found in Appendix A. The hydrogenic ions of C, N and O were fully considered, Figure 3.3 shows the Grotrian diagram for N VII.

Table 3.10: Number of energy levels and transitions for CNO model atoms.  $\lambda_e$  is the ionization edge in Ångströms.

Atom	$\lambda_e$ Å	TOPbase		NIST		Total		Model atom	
		Levels	Lines	Levels	Lines	Levels	Lines	Levels	Lines
C V	31.62	15	684	64	146	79	830	22	151
C VI	25.30	10	703	81	137	91	840	20	115
N V	126.66	0	72	45	402	45	474	18	113
N VI	22.46	17	483	51	90	68	573	29	214
N VII	18.59	10	704	81	137	91	841	52	339
O VI	89.77	2	345	43	126	45	471	18	112
O VII	16.77	18	600	60	188	78	788	29	203
O VIII	14.23	0	839	99	137	99	976	49	295

## Neon and Magnesium

About one third of classical nova explosions occur on ONeMg WDs. This core material can mix with the envelope before the nova explosion, causing Ne and Mg enrichment in the atmosphere and shell. The effectiveness of this process is not well understood, but the presence of these elements is observed in both UV and visible regions. Unfortunately, neon has very few lines in the supersoft range. Resonance transitions of Ne IX and X ending in the  $1s$  level are all either shorter than  $13.5 \text{ \AA}$  or longer than  $37 \text{ \AA}$ .

With increasing atomic number the number of NIST transitions reduces to the strongest lines of the lower excitation levels. For Ne X and Mg XII NIST has no data on lines at all.

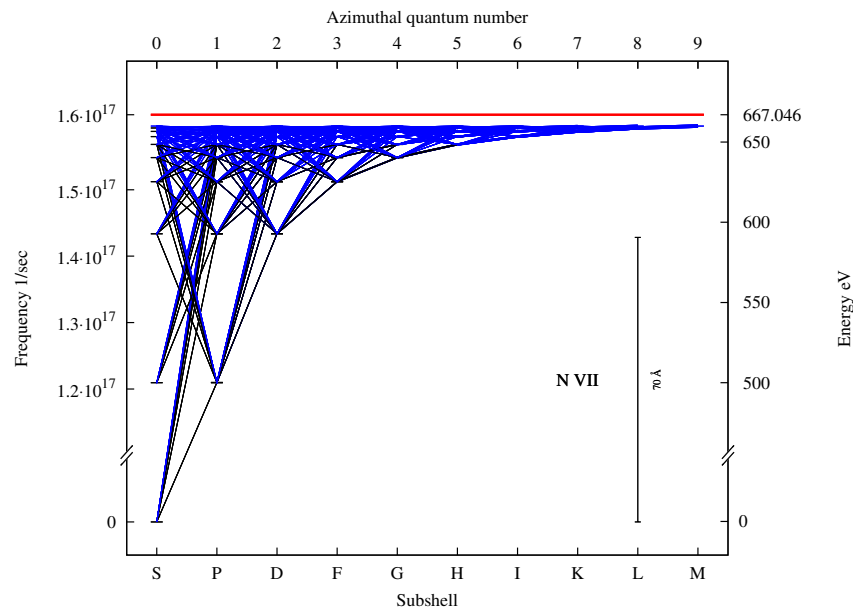


Figure 3.3: Grotrian diagram for N VII. Black lines show NIST levels and transitions, blue ones are from TOPbase. The red horizontal bar is the ionization limit. For transitions line widths are proportional to oscillator strengths. The  $1s$  level is not on the linear scale for better clarity of the graph. The  $70 \text{ \AA}$  bar represents the long wavelength limit for practical purposes. Levels that are farther apart (Lyman-series) than this limit have transitions in the supersoft range.

Table 3.11: Number of energy levels and transitions for Ne and Mg model atoms.  $\lambda_e$  is the ionization edge in Ångströms.

Atom	$\lambda_e$ Å	TOPbase		NIST		Total		Model atom	
		Levels	Lines	Levels	Lines	Levels	Lines	Levels	Lines
Ne VII	59.82	80	4407	148	147	228	4554	18	132
Ne VIII	51.85	4	303	35	65	39	368	11	54
Ne IX	10.37	25	705	50	23	75	728	17	102
Ne X	9.10	0	978	100	0	100	978	25	145
Mg VIII	46.62	225	6649	151	920	319	7569	26	244
Mg IX	37.81	127	2849	71	406	198	3255	23	196
Mg X	33.73	9	190	30	184	39	374	19	120
Mg XI	7.04	25	361	42	192	67	553	25	152
Mg XII	6.32	30	538	40	0	70	538	20	115

## Aluminum and Silicon

CNe are believed to be important sources of galactic Al, Kolb and Politano (1997).

To include Al, I built six ions from Al VIII – Al XIII. My Al IX contains 339 levels that is tremendously simplified to the nine lowermost levels and eight averaged levels for spectral modeling. This blurs individual transitions but Al IX is needed to keep the ionization balance and to set the flux distribution. It does not affect models over 500,000 K significantly. Al X and higher ions have fewer levels and so my model atoms have more details on these ions.

## Sulfur, Argon and Calcium

Sulfur, argon and calcium have numerous lines and provide important line blanketing.

Their complex structure prevents them from being included in modeling in detail. In my models these ions were extremely simplified, according to their principal quantum

Table 3.12: Number of energy levels and transitions for Al and Si model atoms.  
 $\lambda_e$  is the ionization edge in Ångströms

Atom	$\lambda_e$ Å	TOPbase		NIST		Total		Model atom	
		Levels	Lines	Levels	Lines	Levels	Lines	Levels	Lines
Al VIII	43.56	478	13539	88	418	566	13957		
Al IX	37.56	273	7995	104	338	377	8333		
Al X	31.05	160	2938	40	169	200	3107	23	187
Al XI	28.05	8	183	32	208	40	391	25	158
Al XII	5.94	25	361	42	192	67	553	27	176
Al XIII	5.38	35	538	35	0	70	538	21	127
Si VII	50.50	387	10998	102	212	489	11210	25	219
Si VIII	40.85	443	16332	64	167	507	16499	26	204
Si IX	35.31	517	14611	63	270	580	14881	29	257
Si X	30.89	297	8820	78	289	375	9109	26	238
Si XI	26.04	150	2908	52	244	202	3152	31	283
Si XII	23.68	9	186	30	174	39	360	25	159
Si XIII	5.09	8	252	71	585	79	837	27	173
Si XIV	4.64	30	538	40	0	70	538	21	127

numbers, into 9-10 levels only. In all cases the ground levels were treated separately and all higher energy levels were grouped together assuming their population changes in a coordinated way.

## Iron

Similarly to sulfur, argon and calcium, the large number of energy levels and transitions of Iron cannot be treated in the format of light metals in the calculations. For this reason I first combined NIST and TOPbase atomic data with TOPAtom into the standard format. Then I split these large files into separate data files for energy levels, continuum transitions and line transitions in Kurucz CD-ROM 22 format. Lanz and Hubeny (2003) and Lanz and Hubeny (2007) gave model atoms for iron from singly

ionized to Fe VI. To validate my method I built an Fe VI model atom and compared my result to the published input. The original Kurucz Fe VI has 4740 energy levels and 475,750 transitions. In my model atom I have 761 levels and 37,047 transitions, although as TOPbase levels are actually multiplets, the number of individual levels and transitions are somewhat greater. I show a comparison between Kurucz and TOPbase transitions in Figure 3.4. TOPbase transitions are weaker in general and it is obvious that the Kurucz data is superior for low ionizations. Low energy transitions are not very significant as they do not contribute lines in the supersoft range and therefore they do not change the atmospheric structure. Similarly, due to the low spectral resolution the short wavelength transitions form blends and are not distinguishable separately, but they affect the emergent flux through blanketing.

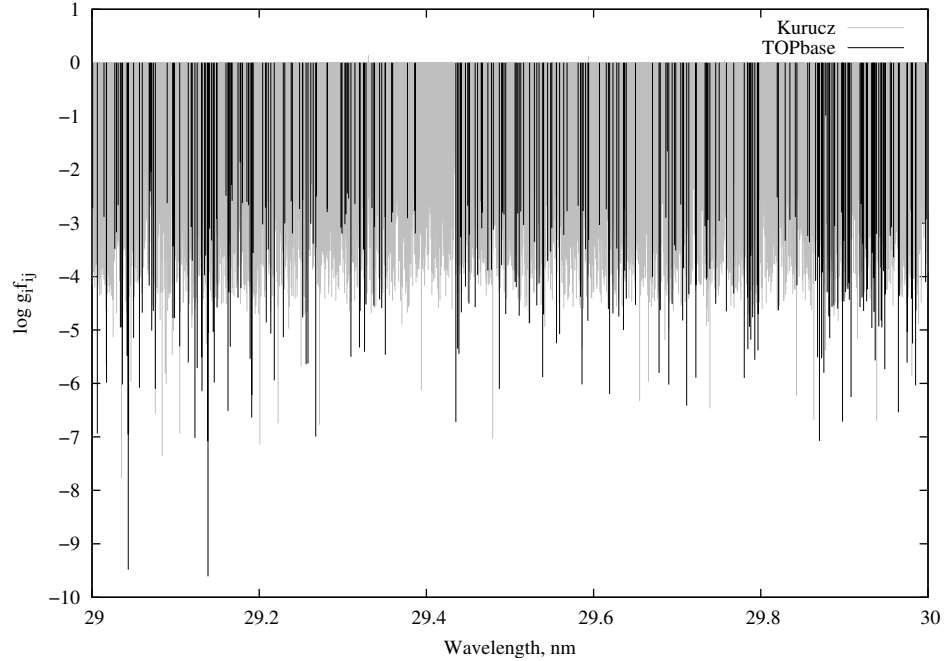


Figure 3.4: Comparison of Fe VI lines in Kurucz database and TOPbase.

I worked out Fe VI in the OS mode and Fe XIV – Fe XXVI model atoms in standard mode. In OS mode levels are assigned into superlevels based on their energies and parity. Figure 3.5 shows the even parity energy levels for Fe VI. Energy levels are labeled with integer IDs from the ground level up to the highest levels. The ionization limit is at zero energy. Doubly excited levels cause autoionization, in this case an excited atom returns to the ground state of its next ionization degree. These levels lie lower than the ionization limit and assigned negative energies and they are always treated separately from regular levels. TOPAtom shows this kind of graph for even and odd parity levels and one can select the boundaries of a level group by mouse clicks. The interactive graphs allow for zooming as well. Once the superlevels are set up the program calculates their energies as in the standard mode and constructs the model atom file. However, in this case the model atom file refers to auxiliary data files in which data for bound-free and bound-bound transitions are stored. Bound-free transitions are not smoothed, they are represented by the weighted average of all individual cross sections in the same superlevel. Data on photoionization cross sections is stored in `ion.pcs` file. For lines and energy levels data is written into `ion.lin` and `ion.gam` files in Kurucz CD-ROM 22 format, respectively.



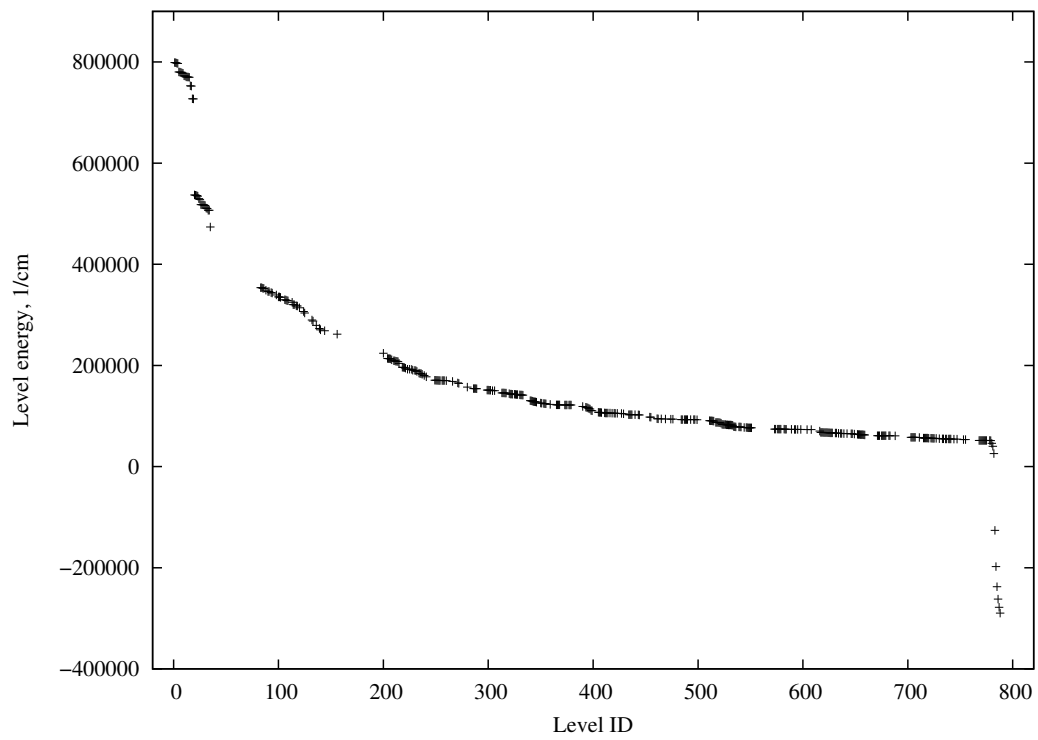


Figure 3.5: 349 even parity energy levels for Fe VI in TOPbase and NIST.

## Chapter 4

# X-ray Modeling of Classical Novae

The first detailed X-ray spectral modeling of a supersoft source with TLUSTY was done by Lanz et al. (2005) on CAL 83. I followed their methodology as well as general considerations for hot stars from Lanz and Hubeny (2003). I used my model atoms and carried out spectral analysis of two recent novae (V4743 Sgr and V2491 Cyg) in their supersoft phase to test the new atomic input, and to set up boundaries for their luminosities and abundances. In general, to model stellar atmospheres one needs to construct a series of spectra in a possible parameter space for effective temperature, gravity and abundance. Then the elements of this model grid can be compared to observed data using  $\chi^2$  minimization method to find the best fit model. Using the results to update input parameters, the fitting process can be repeated until a satisfactory match is achieved. In this work I used TLUSTY version 200 for the atmospheric structure, and SYNSPEC version 48 to calculate synthetic x-ray spectra.

There are severe complications to modeling supersoft sources. Rough estimates of

effective temperatures and surface gravities can be derived from observations. Unfortunately, determination of chemical composition is not straightforward. The CNO-processed hydrogen-burning envelope has a peculiar abundance with increased helium, nitrogen, oxygen and depleted carbon. This abundance is further complicated by both the mixing of WD core material into the envelope and the unknown original composition of the accreted material. Line-blanketing has a crucial role in both the structure of the atmosphere and in the formation of the final spectrum. The flux blocked by these lines emerges at other, higher frequencies. Because the bandwidth of the spectrum in which energy transport occurs is restricted by lines, a steeper temperature gradient is necessary in underlying layers to drive the flux, causing the effect called backwarming (Mihalas, 1978). These effects can be seen in Figure 4.1 where LTE and non-LTE spectra with same composition, effective temperature and surface gravity were compared. With increasing surface gravity this effect decreases and spectra calculated in LTE are similar to non-LTE. Ionization balance can change significantly throughout the atmosphere due to non-LTE effects over a few thousand Kelvins. The extended and expanding atmosphere complicates the spectral appearance further. TLUSTY's basic assumptions, that is, the atmosphere is in hydrostatic equilibrium and can be considered in plane-parallel geometry break down for novae. To include the effects of an extended and dynamic atmosphere in modeling a major upgrade of the code is needed, which is not within the scope of this work. However, the atomic data input presented in Chapter 3 is necessary for future work with supersoft sources and important conclusions on atomic data can be drawn from static and plane-parallel

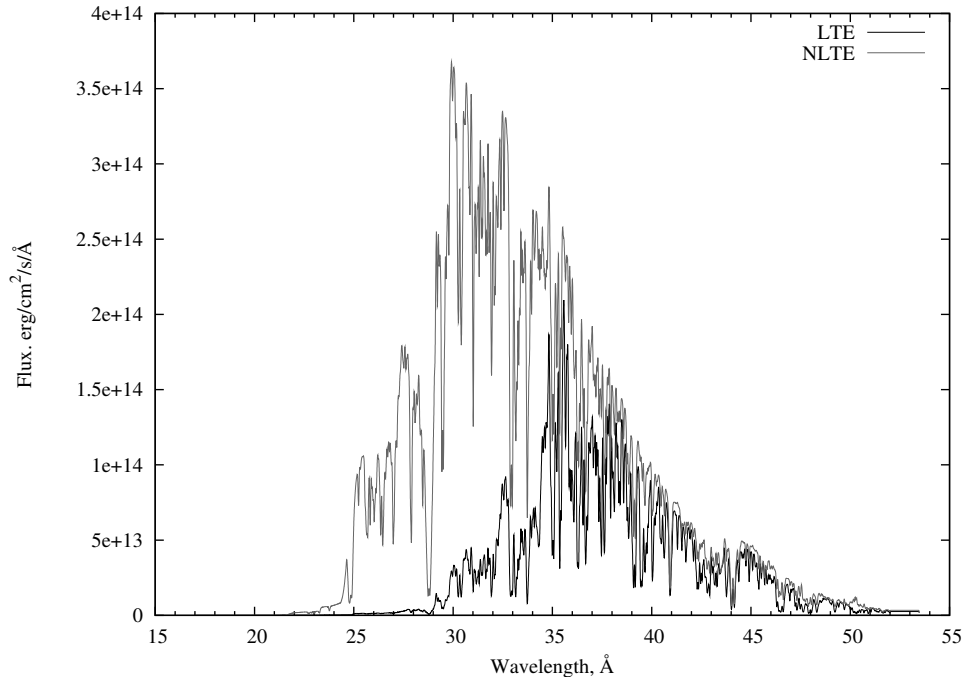


Figure 4.1: Comparison of LTE and non-LTE synthetic spectra calculated with the same model input at  $T_{\text{eff}} = 450,000$  K and  $\log g = 8.00$  cm/s $^{-2}$ . Spectra are corrected for interstellar absorption with  $N_h = 4.1 \times 10^{-20}$  cm $^{-2}$  and convolved for Chandra resolution (see Section 5.5).

tests.

The final spectrum is dominated by both the few strong lines of abundant light metals and the blanketing of numerous weak lines of heavier metals. Simple CNO models can be calculated fast based on observed line strengths, but because of the strong coupling between species it is necessary to include all heavier elements in the modeling at once. With increasing atomic number, intermediate levels become more significant, neglecting these decrease modeling accuracy. By including these levels computer time also increases drastically. Also, inaccuracies in atomic data, the blurred energy levels of averaged model atoms and the overwhelming interstellar absorption altogether

prevent qualitative methods. Model fitting was done by eye, within tolerances chosen by changing each model parameter one-by-one and inspecting their effects on the final spectrum.

Proton collision rates were neglected in modeling as Petz (2005) did not find significant contribution of this process. A microturbulent velocity of 50 km/s was used, similar to O-star models of Lanz and Hubeny (2003). The frequency range was automatically set up for continuum transitions by TLUSTY according to  $\nu_{\max} = 8 \times 10^{11} T_{\text{eff}}$ , or  $h\nu_{\max}/kT_{\text{eff}} \approx 38$ . The minimum frequency was  $10^{12}$  Hz for all models. The same frequency range was applied for line transitions as well. The Rosseland optical depth was  $10^{-7}$  in the first, and increased to  $10^4$  in the last depth point to consider the low opacity of hydrogen. The radiative transfer equation was solved by an ordinary second-order Feautrier method with a full ALI scheme, where the diagonal  $\Lambda^*$  operator was evaluated by the algorithm of Rybicki and Hummer (1991). Bound-free transitions were taken as primarily linearized transitions with photoionization cross sections taken from TOPbase. Electron collisional rates were calculated by Seaton's formula (Equation 4.1) for continua:

$$\Omega = 1.55 \times 10^{13} T^{-1/2} U_0^{-1} \exp(-U_0) \sigma_0 \bar{g} \quad (4.1)$$

where  $U_0 = (E_j - E_i)/kT$ ,  $\sigma_0$  is the absorption cross section at the ionization edge and  $\bar{g} = 0.3$  for all ions. Bound-bound transitions (spectral lines) were treated in ALI with Doppler profiles. Only the strongest resonance lines of nitrogen and oxygen were considered with depth-dependent Voigt profiles. Collisional rates were calculated by

Van Regemorter’s formula (Equation 3.6). Light metals up to silicon were considered with detailed model atoms. Sulfur, argon and calcium were included with their simple model atoms having only 9–10 levels per ion. Ions of iron were considered with their ground levels only to account for the effects of iron on the ionization balance. At least 50 depth points were set up, for some models it was increased to 80. With less than 50, or more than 80 depth points the convergence properties of the models got worse. The maximum relative change of the state vector was kept at its default value of  $10^{-3}$ , as shown in Figure 4.19. Figure 4.19 shows only the relative changes of occupation numbers as temperature, and pressure convergence were much faster for every model. Opacity Sampling was not used as with light metals it did not change the spectra but increased the computation time. For iron-peak elements however, the many new frequency points introduced by the OS mode exceeded computer limits.

Model calculation started with invoking TLUSTY and SYNSPEC consecutively in a user defined temperature, surface gravity range and resolution. Super-Eddington models were skipped as they do not converge and are out of TLUSTY’s modeling domain. Each model atmosphere was calculated in two steps. First a continuum gray model was calculated, keeping all lines in detailed balance. This was followed by a full non-LTE model calculation with lines and frequency dependent opacities. Optionally, LTE models can be calculated before non-LTE, but this is not necessary for the convergence of non-LTE models. Element abundance can be changed parallel for all elements, starting with solar abundance and increasing to 3, 30, 100 and  $10^3$  times their solar values. Convergence properties of the solar models are poor and

this method failed for higher abundances and high energy levels included. Also the large number of overlapping lines (up to 15) made it hard or impossible to identify individual lines in the spectra. Abundances were set up individually for each star based on nova shell abundances in Andreä et al. (1994) and Gehrz et al. (1998) and by investigating the effects of different species on the spectra. The shell compositions can be seen in Figure 4.6. To discover the contribution of each element to the spectra, I calculated models with similar input parameters, only changing the abundance of one element at a time. Figure 4.2 and 4.5 show these graphs for carbon, nitrogen, neon and magnesium, respectively. For carbon, the increasing abundance changes the flux significantly. A strong cut-off can be seen below 25 Å, while the flux increases in the continuum over 25 Å. An increase in line strengths of the Lyman series (33.7, 28.5, 27.0, 26.3 26.0 Å) can be also seen. Similar effects can be found in the case of nitrogen only on a moderate level. The high energy cut-off is at 21.5 Å and the Ly $\alpha$  (24.7 Å) line is dominant. The soft part of the spectrum is practically unchanged.

The neon abundance has not much effects on the spectra. Unfortunately neon has no spectral lines in the supersoft range. Transitions to the 1s level lie in the hard X-rays, and transitions to 2s and 2p levels are all softer than 30 Å. Neon decreases the flux between 23 and 43 Å, while it does not introduce significant changes below 23 Å. A small increase can be seen over 43 Å. More interesting are the effects of magnesium. While increasing magnesium abundance only slightly reduces the flux below 22 Å, there is a great impact between 23 and 35 Å. The large photoionization cross-section of magnesium redistributes the energy into the soft tail of the spectrum.

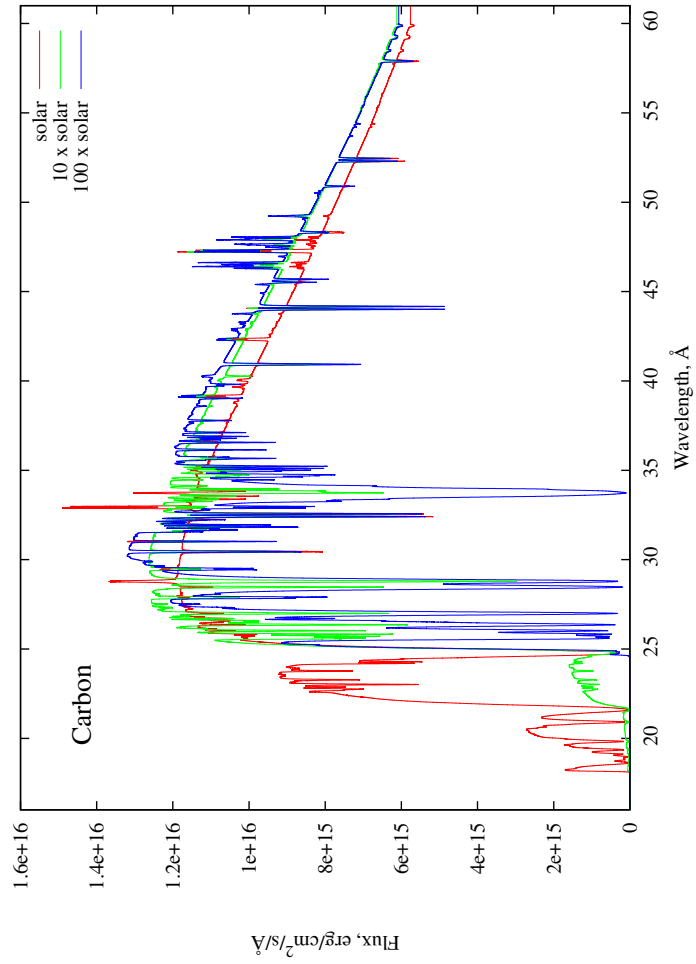


Figure 4.2: Effects of different abundances of carbon on the final spectra.



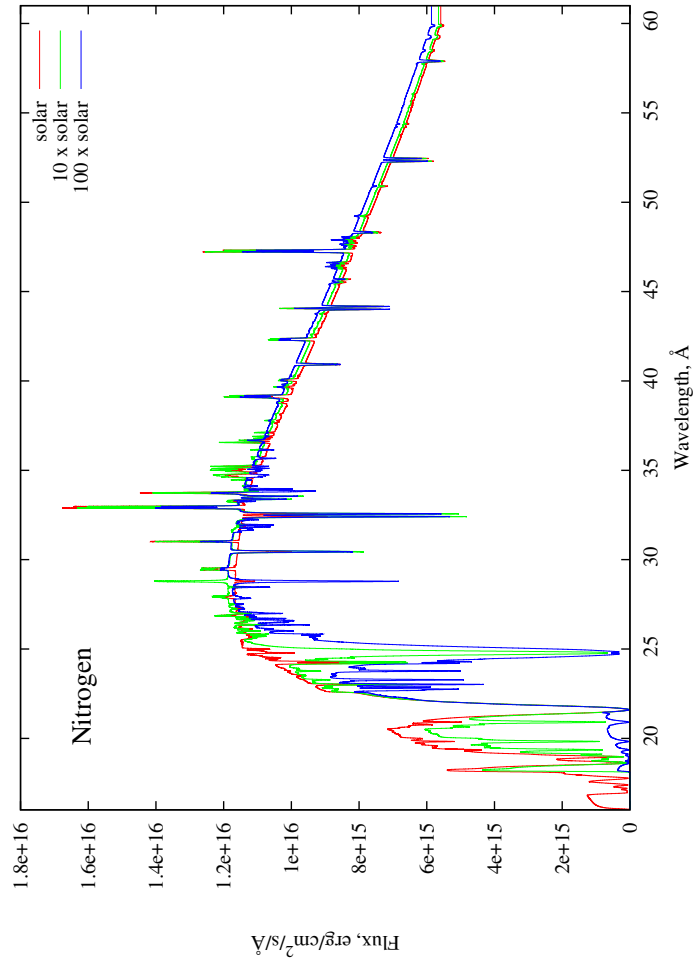


Figure 4.3: Effects of different abundances of nitrogen on the final spectra.

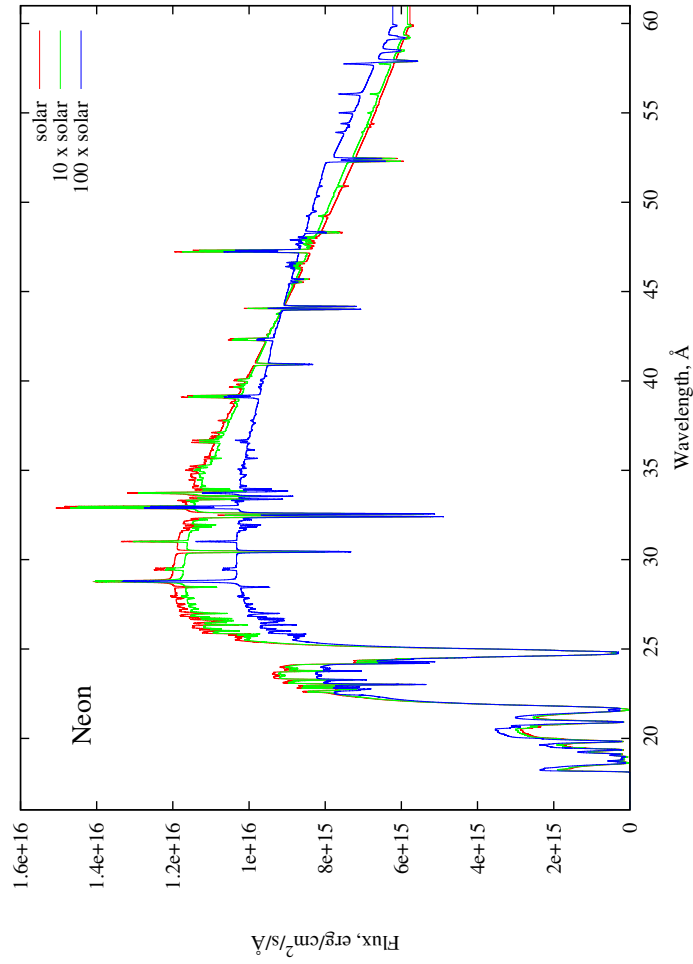


Figure 4.4: Effects of different abundances of neon on the final spectra.

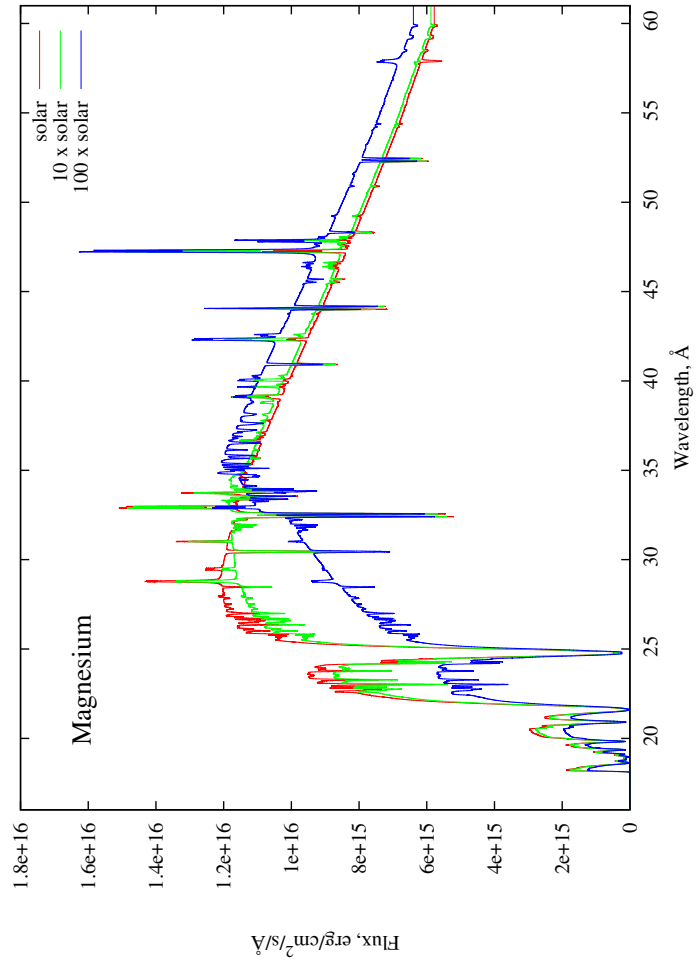


Figure 4.5: Effects of different abundances of magnesium on the final spectra.

Similar graphs were calculated for all included species and chemical composition was set up with the help of these diagnostics.

Once the grid had been generated all spectra were corrected for interstellar absorption as described in Section 5.4, and convolved with the instrumental resolution, as described in Section 5.5. Then spectra were scaled to observations, which directly

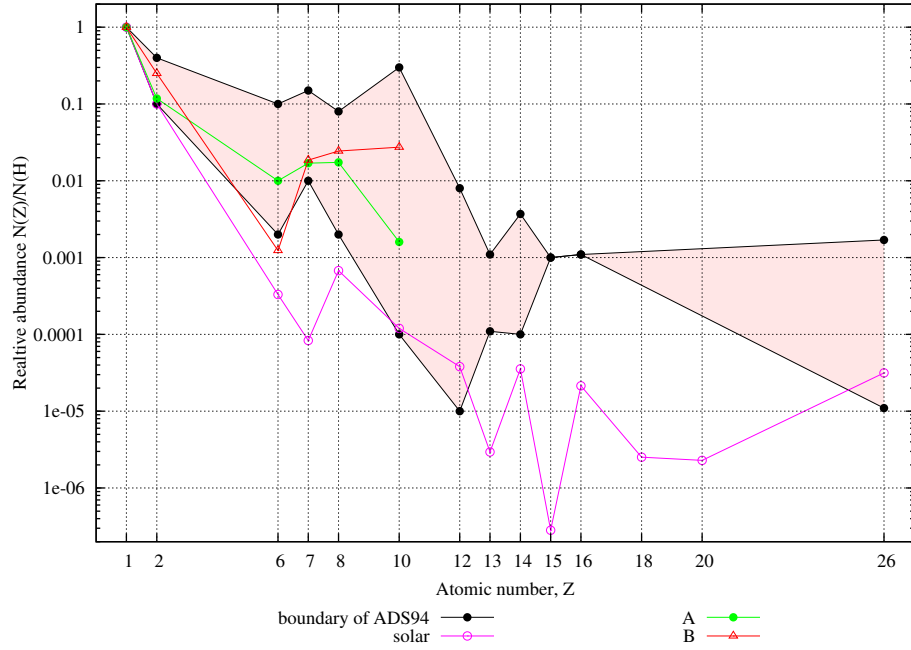


Figure 4.6: Nova abundance limits based on UV and optical observations of nova shells, data taken from Andreä et al. (1994) and Gehrz et al. (1998). Solar abundance is from TLUSTY, Grevesse and Sauval (1998). Lines A and B shows abundance from Table 4.1 (MacDonald and Vennes, 1991).

provided  $d^2/R^2$  factors, where  $R$  is the radius of the star and  $d$  is its distance. The next step would be to select some strong lines and cross-correlate the model and data to get Doppler-shifts. This can be done for lines of separate species or ionization degrees. The last step would be to select some lines of a given ion and get  $\chi^2$  for each

spectrum. All these steps can be done by TGRID, a procedure-oriented script which generates the grid and carries out the steps of spectral analysis. Unfortunately, the large number of overlapping lines in the soft X-rays makes  $\chi^2$  minimization unreliable. Due to the strong line blanketing radial velocities could be measured only for the strongest lines of nitrogen and oxygen.

Table 4.1: Abundance for CO and ONeMg novae from MacDonald and Vennes (1991).

Abundance pattern	WD type	Fractions					
		H	He	C	N	O	Ne
A (mass)	CO	0.47	0.22	0.059	0.11	0.13	0.015
A (number)	CO	1.00	0.118	0.01	0.017	0.0174	0.0016
A (number $_{\odot}$ )	CO	1.00	1.21	29.42	150.6	20.51	13.9
B (mass)	ONeMg	0.31	0.31	0.0046	0.08	0.12	0.17
B (number)	ONeMg	1.00	0.25	0.00124	0.0186	0.0244	0.0274
B (number $_{\odot}$ )	ONeMg	1.00	2.58	3.47	166.1	28.7	238.8

Temperature and gravity ranges of my model grid can be seen on Figure 4.7. It is worth comparing surface gravities for some grid points with Figure 1.7 to find mass, radius and relative numbers of these WD cores. However, this mass-radius relation valid only for the degenerate cores, as the atmosphere of CNe in the constant bolometric luminosity phase is significantly extended, up to a few stellar radii. In Figure 4.7 each point represents a TLUSTY model. With SYNSPEC it is possible to change the composition assuming that small changes in abundance do not change the atmospheric structure, so the number of synthetic spectra calculated is larger than shown in Figure 4.7. This  $\log g$  vs.  $T_{\text{eff}}$  diagram also shows the effective modeling domain of TLUSTY. It can calculate atmospheres with effective temperature up to  $10^9$  K, although at high gravities the Chandrasekhar-limit sets a natural boundary,

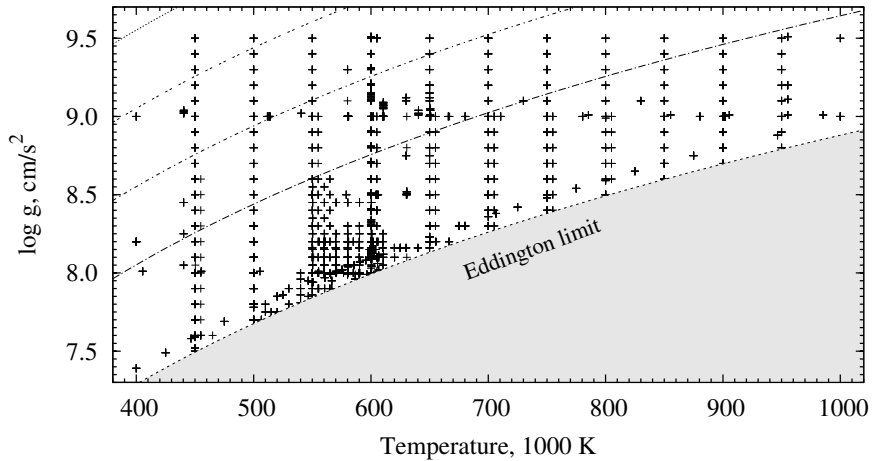


Figure 4.7: Model grid. Each point indicates a TLUSTY model. The Eddington limit and 4 iso-luminosity curves are also shown assuming a given stellar mass and black body radiation.

WDs over  $\log g = 9.5$  were not considered in my work. At low gravities and high temperatures typical for these atmospheres, the Eddington-luminosity sets another limit, as a strong stellar wind breaks down the basic assumption of TLUSTY, i.e. the atmosphere is no longer static. The Eddington-luminosity as function of mass can be written as:

$$L_{\text{Edd}} = \frac{4\pi GMm_p c}{\sigma_T} \cong 3.3 \times 10^4 \left( \frac{M}{M_\odot} \right) L_\odot \quad (4.2)$$

where  $m_p$  is the proton mass and  $\sigma_T$  is the Thomson cross-section for electrons. The black body luminosity is:

$$L = 4R^2 \pi \sigma T_{\text{eff}}^4 \quad (4.3)$$

where  $\sigma$  is the Stephan-Boltzmann constant and  $T_{\text{eff}}$  is the effective temperature of the star. From the two equations above and the definition of surface gravity:

$$g = \frac{GM}{R^2} \quad (4.4)$$

it follows that the temperature dependence of the surface gravity at Eddington-luminosity is:

$$\log g = 4 \times \log T_{\text{eff}} - 15.12 \quad (4.5)$$

where  $\log g$  is in  $\text{cm/s}^2$  and  $T_{\text{eff}}$  is in Kelvins. This modeling limitation is also shown in Figure 4.7

Following Lanz et al. (2005), Compton scattering was neglected. Their analysis did not reveal significant contribution from Compton scattering at 500,000 K and  $\log g = 8.5$ , while extended the computation time. Also, their comprehensive study on line broadening mechanisms concluded that at the high temperature typical for supersoft sources natural broadening dominates linear Stark broadening. In my models natural broadening was included for the strongest resonance lines in model atoms and for all the lines in the line list either from TOPbase or NIST/ASD.

## 4.1 Model Example

A representation of all models is beyond the scope of this dissertation. Because the structures of these atmospheres are only slightly different, here only one of them is discussed in detail. This atmosphere was calculated as part of the grid for V4743 Sgr.

The model parameters are presented in Table 4.2.

Table 4.2: Model parameters of example atmosphere calculated at  $T_{\text{eff}} = 599,900$  K and  $\log g = 8.54$  cm/s<sup>2</sup>. Abundances are given in solar units.

Parameter	Value	unit
Effective Temperature, $T_{\text{eff}}$	599,900.0	K
Surface gravity, $\log g$	8.54	cm/s <sup>2</sup>
H/H <sub>⊙</sub>	1.0	
He/He <sub>⊙</sub>	3.5	
C/C <sub>⊙</sub>	4.0	
N/N <sub>⊙</sub>	27.0	
O/O <sub>⊙</sub>	12.0	
Ne/Ne <sub>⊙</sub>	50.0	
Mg/Mg <sub>⊙</sub>	30.0	
Al/Al <sub>⊙</sub>	10.0	
Si/Si <sub>⊙</sub>	2.0	
S/S <sub>⊙</sub>	1.0	
Ar/Ar <sub>⊙</sub>	0.1	
Ca/Ca <sub>⊙</sub>	0.05	
Fe/Fe <sub>⊙</sub>	0.01	

Figure 4.8 shows the final spectra assuming LTE and non-LTE at identical input parameters. Strong non-LTE effects clearly dominate the spectrum and cause flux redistribution towards high energies as Hartmann and Heise (1997) pointed out with ground level model atoms. This result also shows that hot nova atmospheres can not be modeled in LTE.

The temperature and density structures of the atmosphere are shown in Figure 4.9. The bottom horizontal axis shows the radial distance in the atmosphere calculated from the column mass and density at each depth point. The horizontal axis on the top indicates the corresponding depth points to the radial distance. The short vertical line at 124 km indicates  $\tau_{\text{Ross}} = 1$ , the location of the continuum forming region measured



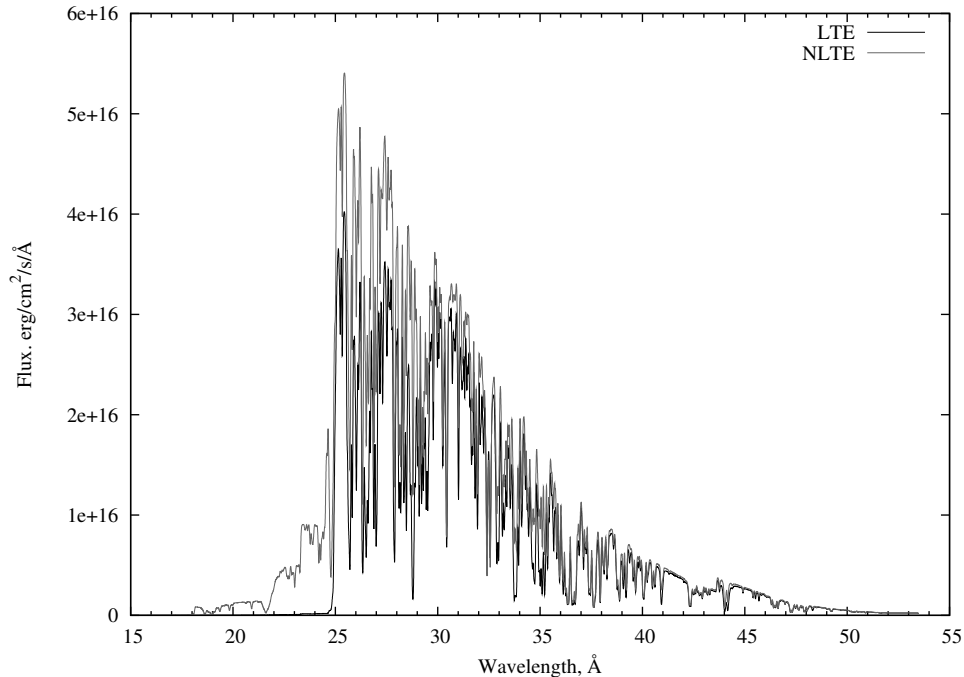


Figure 4.8: Comparison of LTE and non-LTE synthetic spectra calculated with the same model input. Spectra are corrected for interstellar absorption with  $N_h = 4.1 \times 10^{-20} \text{ cm}^{-2}$  and convolved for Chandra resolution (see Section 5.5).

from the bottom of the atmosphere. Temperature decreases sharply with radius in the inner parts of the atmosphere, then above the photosphere it becomes nearly constant. In the outermost layers it shows a slight increase. Density changes slowly at the beginning and over the photosphere it decreases logarithmically.

From level populations given by TLUSTY one can calculate the ionization balance throughout the atmosphere. For this, the ratio of each level population and the total population of the ion must be calculated at each depth point. These graphs are shown in Figures 4.10 – 4.13. Due to the high temperature, hydrogen and helium are completely ionized. Figure 4.10(a) shows that carbon is also ionized throughout

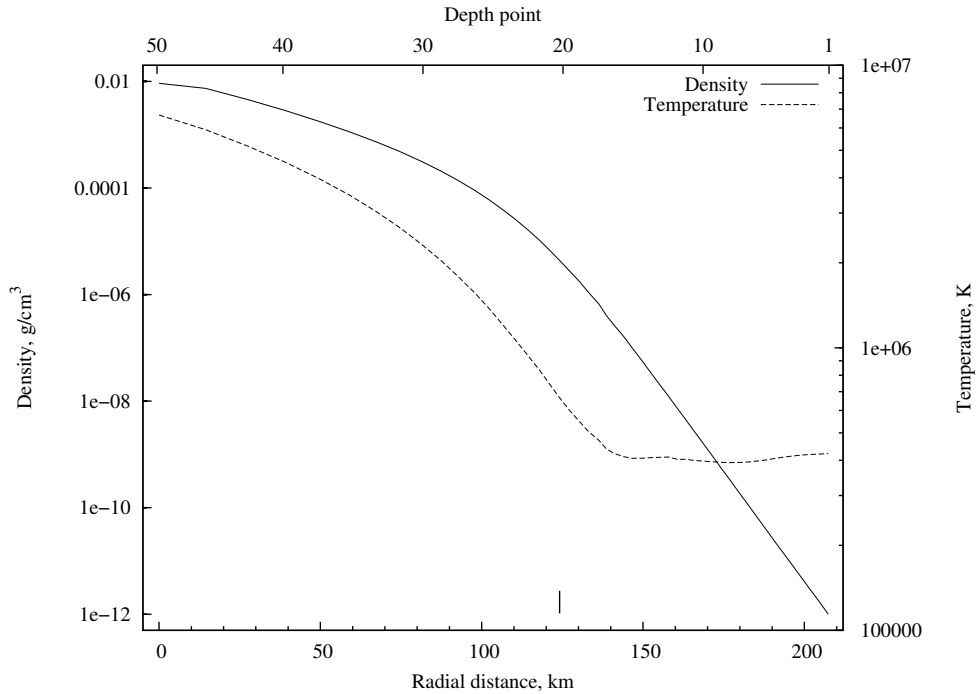
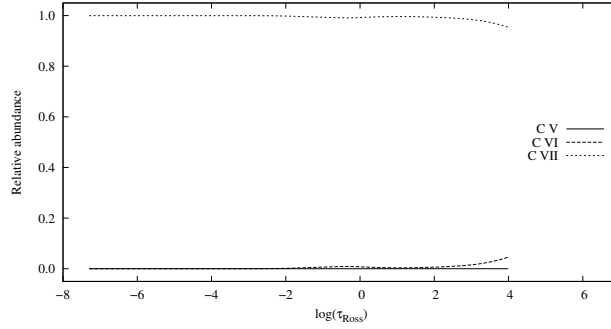


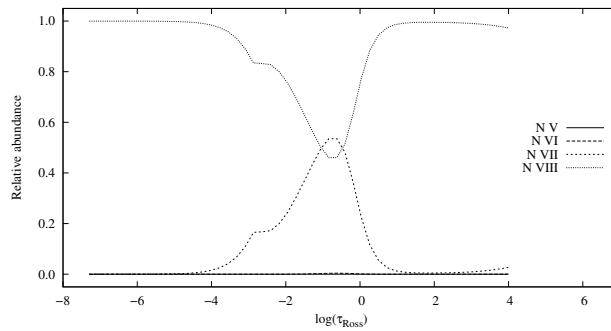
Figure 4.9: Atmospheric structure. The two lines represent the temperature and density throughout the atmosphere as function of radial distance from the bottom of the atmosphere. Corresponding depth points are also indicated.

the atmosphere, with only a very tiny contribution of C VI around  $\log \tau_{\text{Ross}} \approx 0$ , what is also a non-LTE effect. The temperature structure is not monotonic in non-LTE. Proceeding outward from the atmosphere the temperature decreases rapidly, reaching a minimum above the photosphere and increasing in the outermost layers. This effect is more noticeable for nitrogen and heavier elements. From neon through silicon the helium-like ions are dominant in most of the atmosphere. Sulfur, argon, calcium and iron show complex structures with 3–5 dominant ions simultaneously in the atmosphere. Iron shows a stratified structure in the inner parts and Fe XVII alone dominates the atmosphere in most of the line forming region. These graphs are important diagnostics to improve the model input. By excluding levels which do

not contribute to the ionization balance, both the computation time and modeling stability improves.



(a) Carbon.



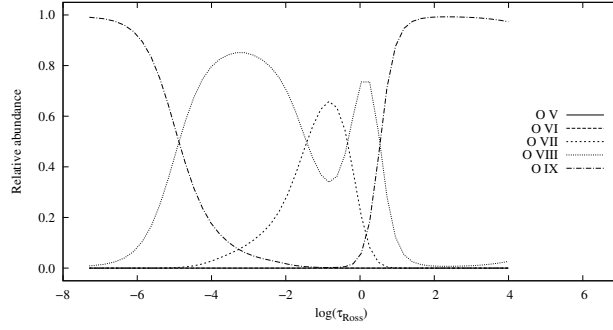
(b) Nitrogen.

Figure 4.10: Ionization fractions for carbon and nitrogen.

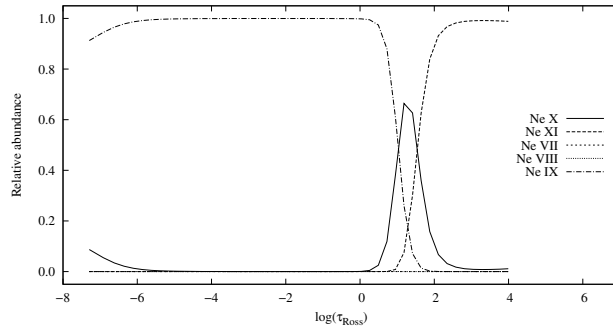
Along with population numbers, in non-LTE TLUSTY also provides departure coefficients for each depth point and all levels. Departure coefficients are defined as the relative fraction of the population of level  $i$  calculated in non-LTE to the level population calculated in LTE:

$$b_i = \frac{n_i(\text{NLTE})}{n_i(\text{LTE})} \quad (4.6)$$

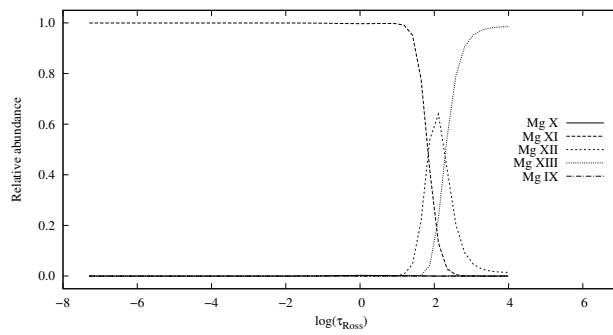
Departure coefficients from carbon to magnesium are shown in Figures 4.14 – 4.18.



(a) Oxygen.

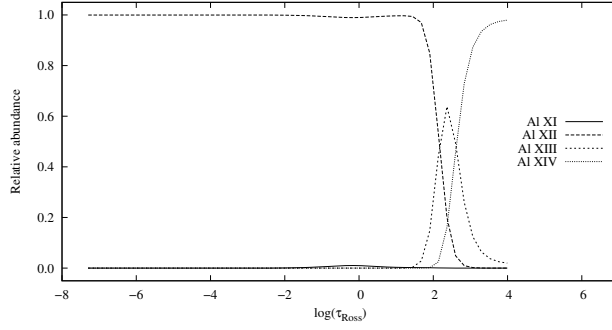


(b) Neon.

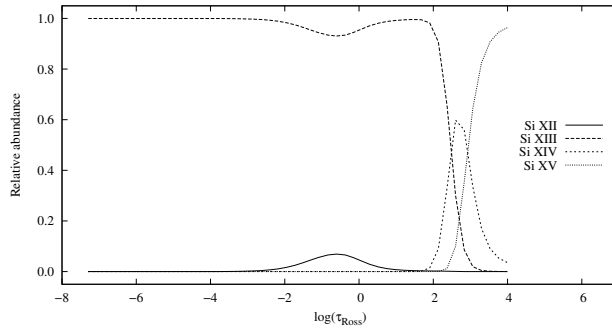


(c) Magnesium.

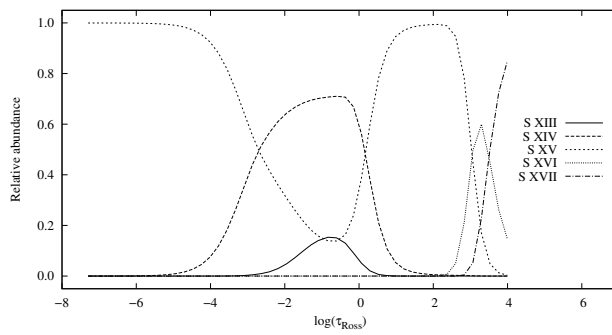
Figure 4.11: Ionization fractions for oxygen, neon and magnesium.



(a) Aluminum.

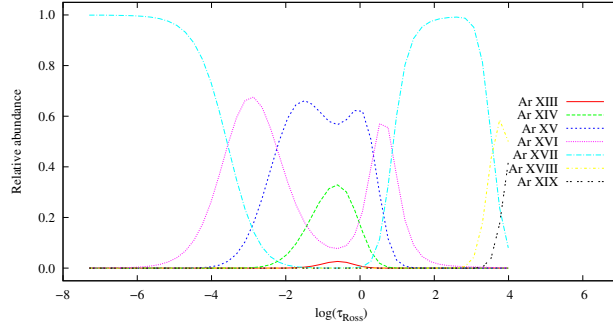


(b) Silicon.

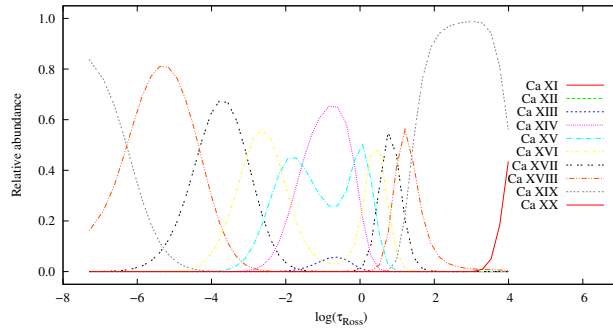


(c) Sulfur.

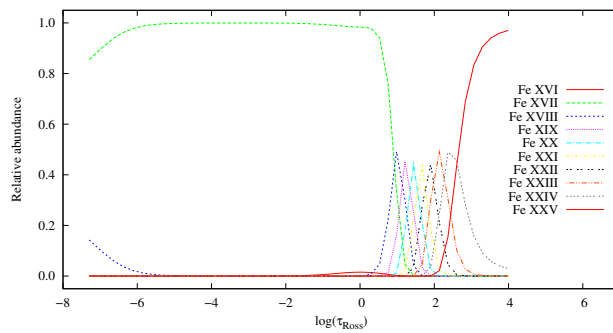
Figure 4.12: Ionization fractions for aluminum, silicon and sulfur.



(a) Argon.



(b) Calcium.

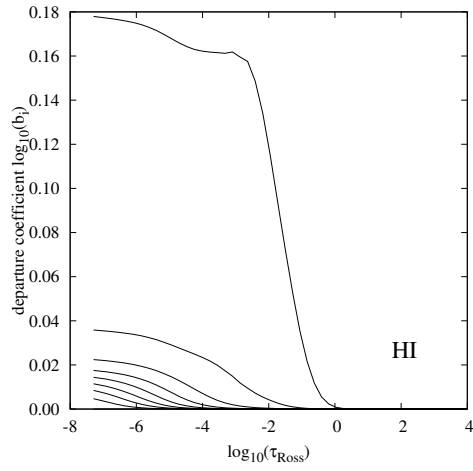


(c) Iron.

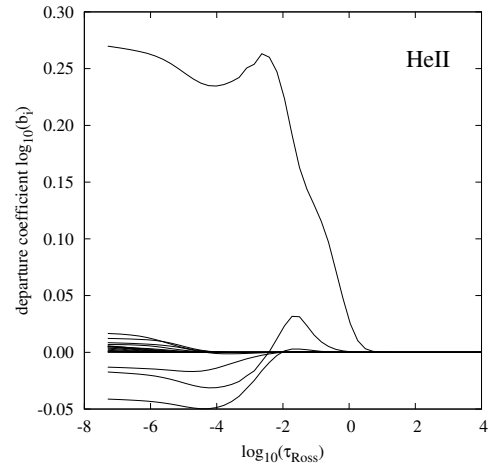
Figure 4.13: Ionization fractions for argon, calcium and iron.

These graphs depict the strength of non-LTE effects on each level. In general, deep in the atmosphere LTE prevails due to high pressure and the fact that departure coefficients are close to one. In the outer half of the atmosphere population numbers can significantly differ from their LTE values. Ground and low lying levels are overpopulated while high levels show less deviation.

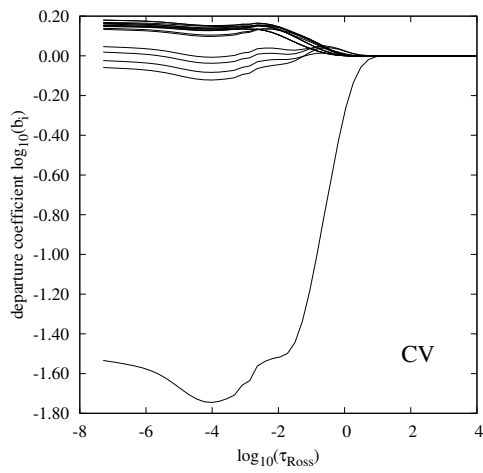
Figures 4.19 and 4.20 show the convergence log for continuum and full non-LTE models, respectively. Convergence is very sensitive for model parameters, and usually about 25–55 iterations are needed. Close to the Eddington limit the convergence slows down, and shows oscillatory behavior. Model atoms and abundances also have great impact on the convergence. During model calculations TLUSTY prints the relative change of effective temperature, electron density and population numbers into a file for each depth point at each iteration. By plotting these quantities one can investigate the convergence properties of the model. In Figure 4.19 the continuum model is presented. The top panel shows the relative-change vs. depth-point curves. Numbering and calculation starts at the top of the atmosphere, depth-point zero means the outermost layer ( $\tau_{\text{Ross}} = 10^{-7}$ ) and 50 is the innermost layer ( $\tau_{\text{Ross}} = 10^4$ ) of the atmosphere. Thin grey lines represent the relative changes at each iteration. Usually relative changes are large at the beginning and quickly fall below the convergence limit (horizontal line at  $\delta n_i/n_i = 10^{-3}$ ) in the innermost layers. The rest of the atmosphere converges more slowly, especially at the photosphere around depth-point 30 and in the outermost layers. The lower panel in Figure 4.19 shows the relative-change vs. iteration number relations. It is like looking at the top panel from the side. This graph shows



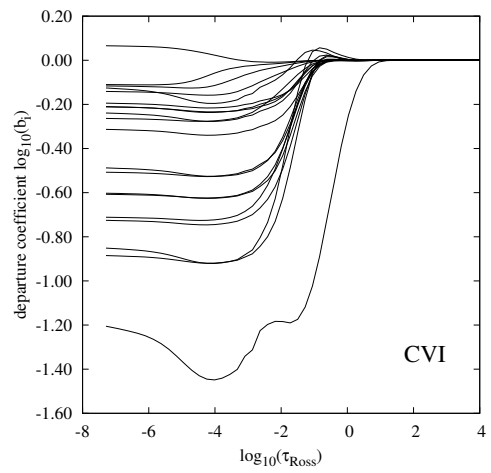
(a) For H I.



(b) For He II.



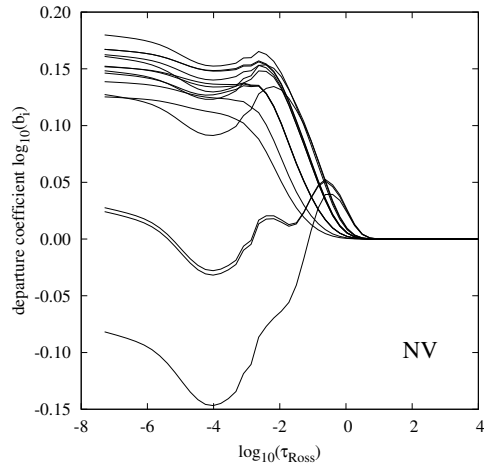
(c) For Carbon V.



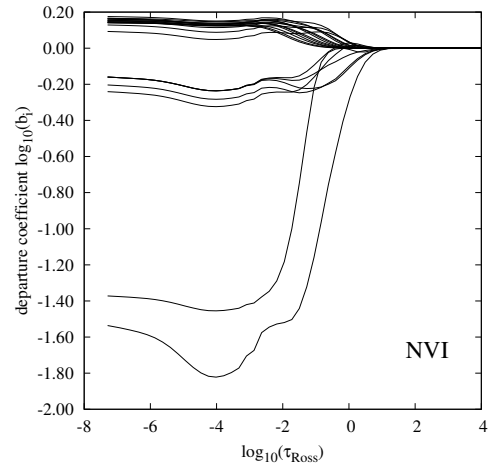
(d) For Carbon VI.

Figure 4.14: NLTE departure coefficients of ions from H I – C VI.

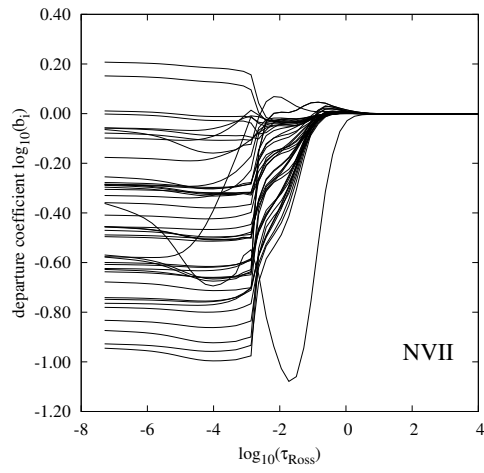




(a) For Nitrogen V.

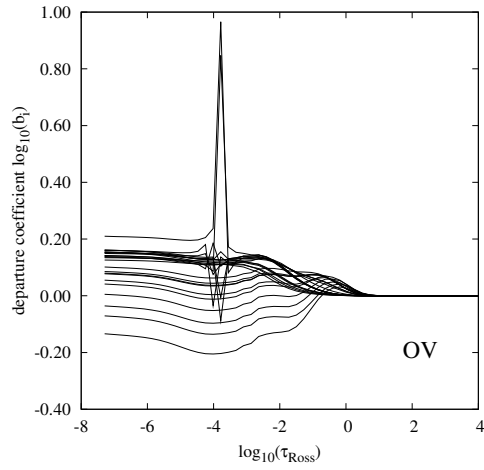


(b) For Nitrogen VI.

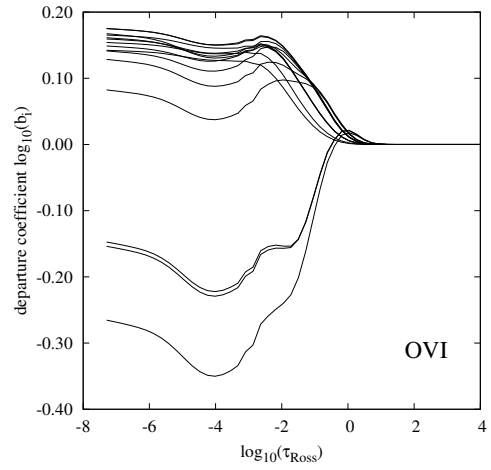


(c) For Nitrogen VII.

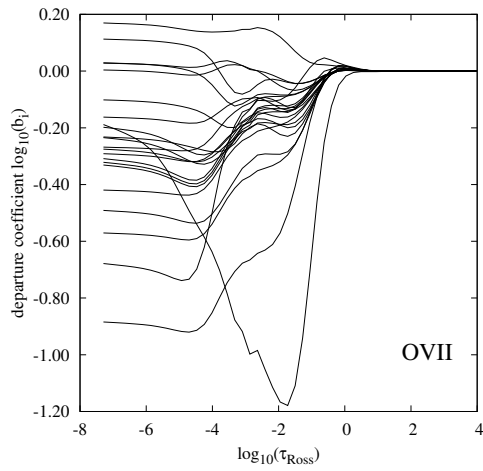
Figure 4.15: NLTE departure coefficients of ions from N V – N VII.



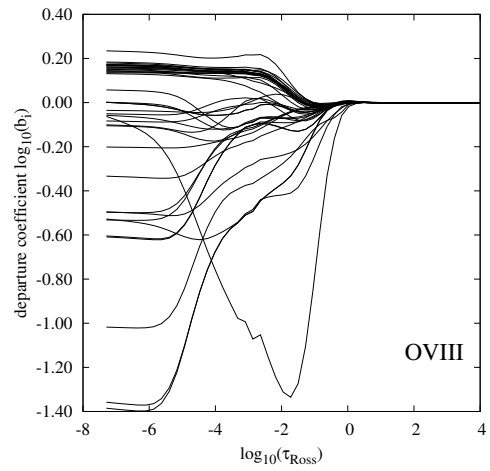
(a) For Oxygen V.



(b) For Oxygen VI.

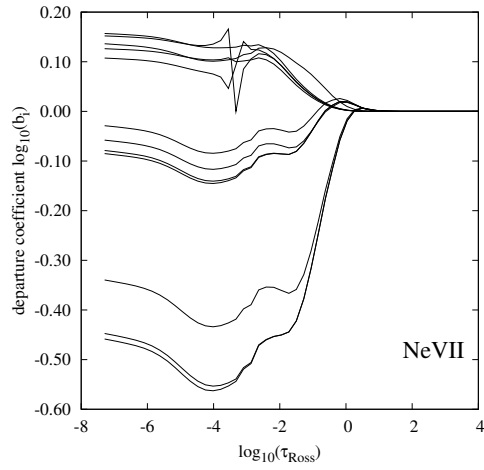


(c) For Oxygen VII.

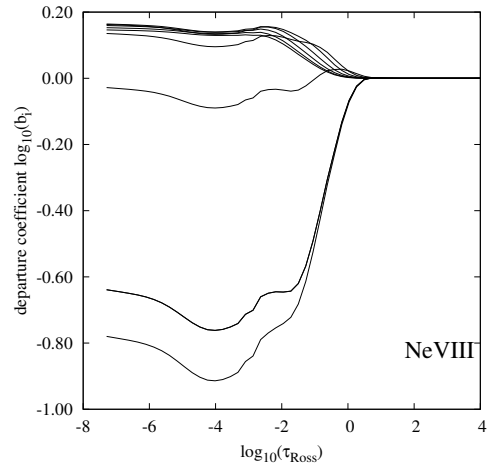


(d) For Oxygen VIII.

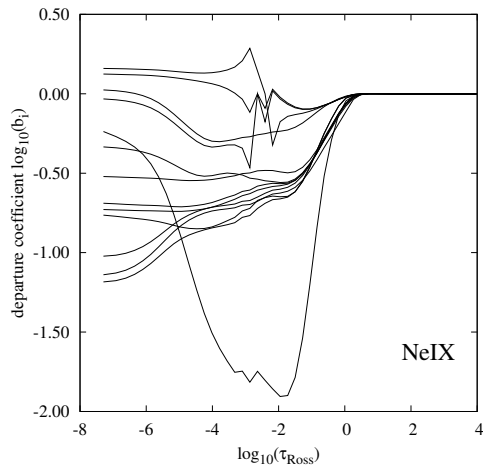
Figure 4.16: NLTE departure coefficients of ions from O V – O VIII.



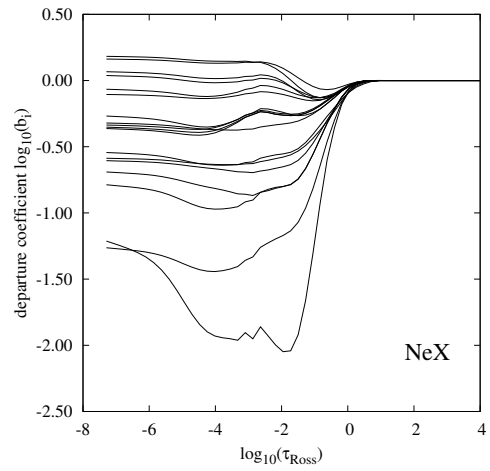
(a) For Neon VII.



(b) For Neon VIII.

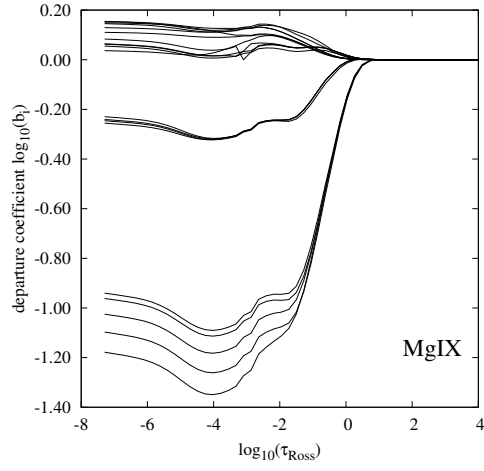


(c) For Neon IX.

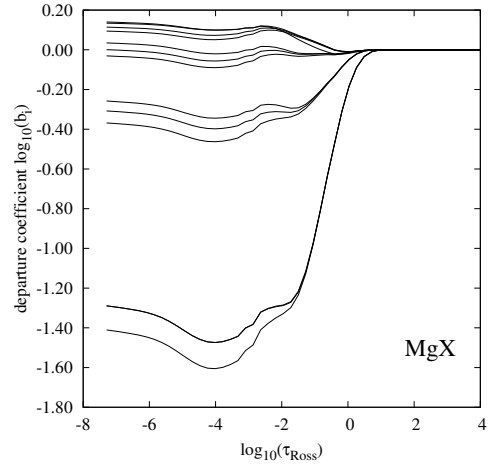


(d) For Neon X.

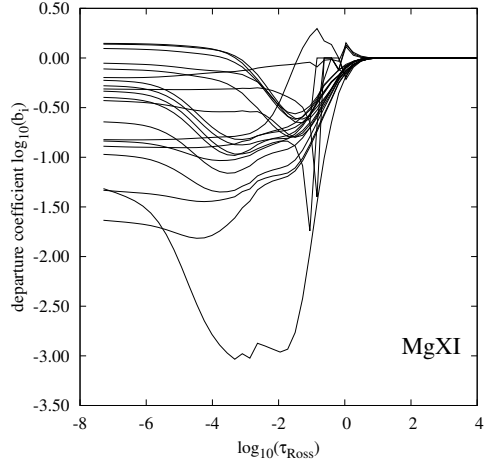
Figure 4.17: Departure coefficients of included ions from Ne VII – Ne X.



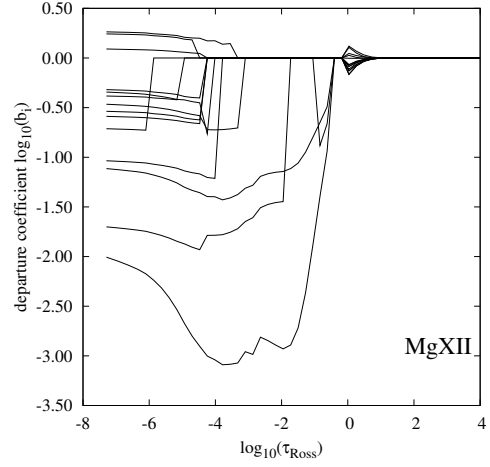
(a) For Neon VII.



(b) For Neon VIII.



(c) For Neon IX.



(d) For Neon X.

Figure 4.18: Departure coefficients of included ions from Mg IX – Mg XII.

that 21 iterations were required for full convergence. Kantorovich acceleration started at the third iteration and repeated after every third iteration. Ng acceleration was applied from the seventh iteration and repeated after every fourth step. Figure 4.20 has the same structure as Figure 4.19 only for the NLTE-L model, which considers spectral lines as well. Similar convergence properties can be seen, but non-LTE effects are more prominent. The convergence is very slow in the outermost layers where non-LTE effects of spectral lines are the strongest. The model required 35 iterations for a solution. Figures 4.19 and 4.20 show the normal behavior of convergence. It is also possible to show the convergence of the effective temperature and electron density in similar graphs, however as they converge much faster the convergence of population numbers alone is adequate.

Convergence log graphs are continuously updated and displayed during the calculations at a user-defined frequency. This helps to be aware of convergence properties and to improve the parameters which control the calculation. Graphs for both ionization fractions, departure coefficients and convergence logs are automatically generated by TGRID.

## 4.2 Trends in the model grid

In order to experience the effects of effective temperature, gravity, different abundances and other variables on the final spectra model sequences were calculated. All models were constructed with parameters from Table 4.2 unless otherwise noted.

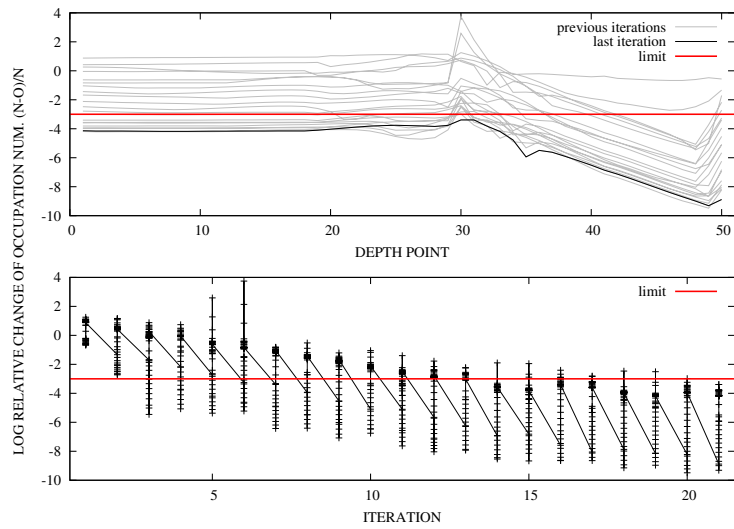


Figure 4.19: Convergence log of the non-LTE continuum model. Upper panel shows relative change vs. depth points. Gray lines represent the relative change of population numbers at each depth point, the thin black line is the relative change for the last iteration. Thick horizontal line shows the convergence limit,  $\delta n_i/n_i = 10^{-3}$ . The lower panel is the relative change vs. iteration number, like looking at the top panel from the side.

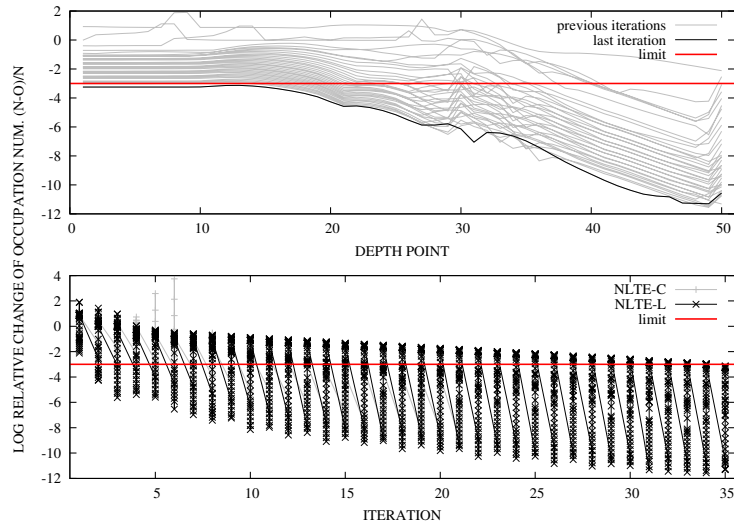


Figure 4.20: Convergence of the full non-LTE model.

### Gravity sequence

The effects of gravity were examined in the range of  $\log g = 8.00 - 9.50 \text{ cm/s}^2$  at  $T_{\text{eff}} = 600,000 \text{ K}$ . These models are shown in Figure 4.21. The atmospheric composition was kept unchanged. The most important effect of gravity is on the flux below  $30 \text{ \AA}$ . In this region with increasing gravity ionization edges become stronger and the energy distribution becomes softer. Observed continuum emission below  $25 \text{ \AA}$  confirms that novae in the constant bolometric luminosity phase are close to, or over the Eddington limit. The atmospheric structure for these models can be seen in Figure 4.22, where temperature and density are plotted as function of optical depth between  $\tau_{\text{Ross}} = 10^4 - 10^{-7}$ . The surface gravity does not affect the temperature profile of the atmosphere. There are only small differences above the photosphere between  $\tau_{\text{Ross}} = 1$

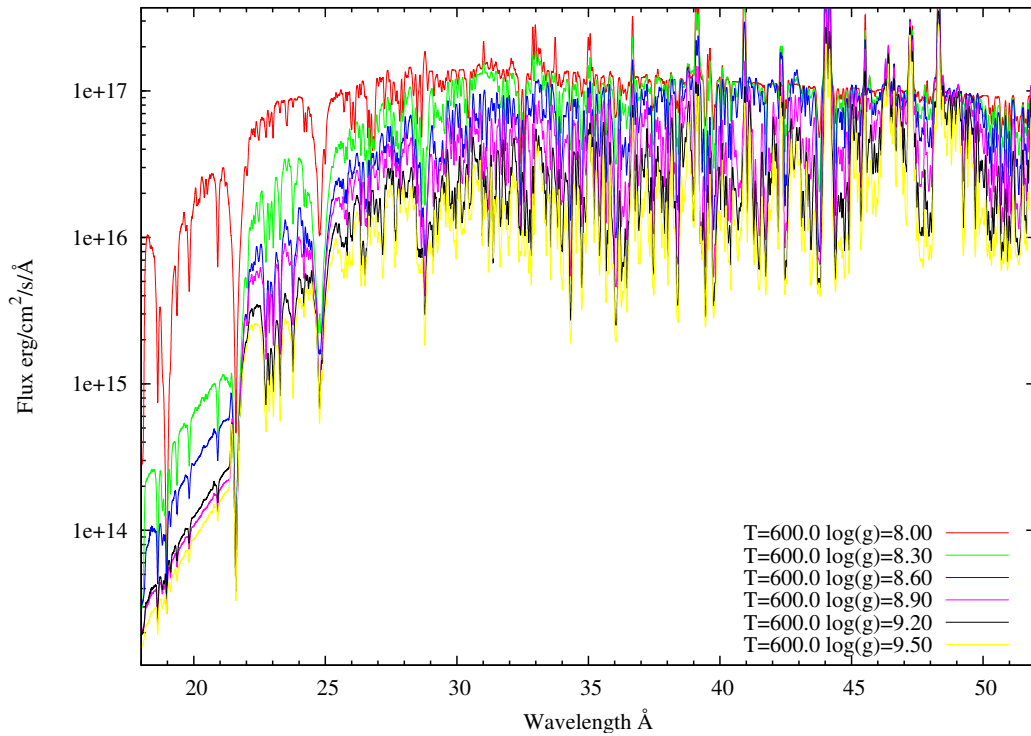


Figure 4.21: Effects of surface gravity on the spectra. Models were calculated at the same composition, at effective temperature of 600,000 K, gravity is indicated in cgs units.

and  $10^{-4}$ . The density profile shows gradual change with surface gravity (WD mass) which increases the density throughout the atmosphere.

The effects of surface gravity are in good agreement with the calculations of van Rossum and Ness (2010). Figure 4.23 shows their models with different mass-loss rates calculated with PHOENIX<sup>1</sup>. PHOENIX is a general purpose stellar atmosphere code for calculating hydrodynamic model atmospheres in spherical geometry. Their models show that the softening of the energy distribution with increasing gravity is continued over the Eddington limit as well.

<sup>1</sup><http://www.hs.uni-hamburg.de/EN/For/ThA/phoenix/index.html>



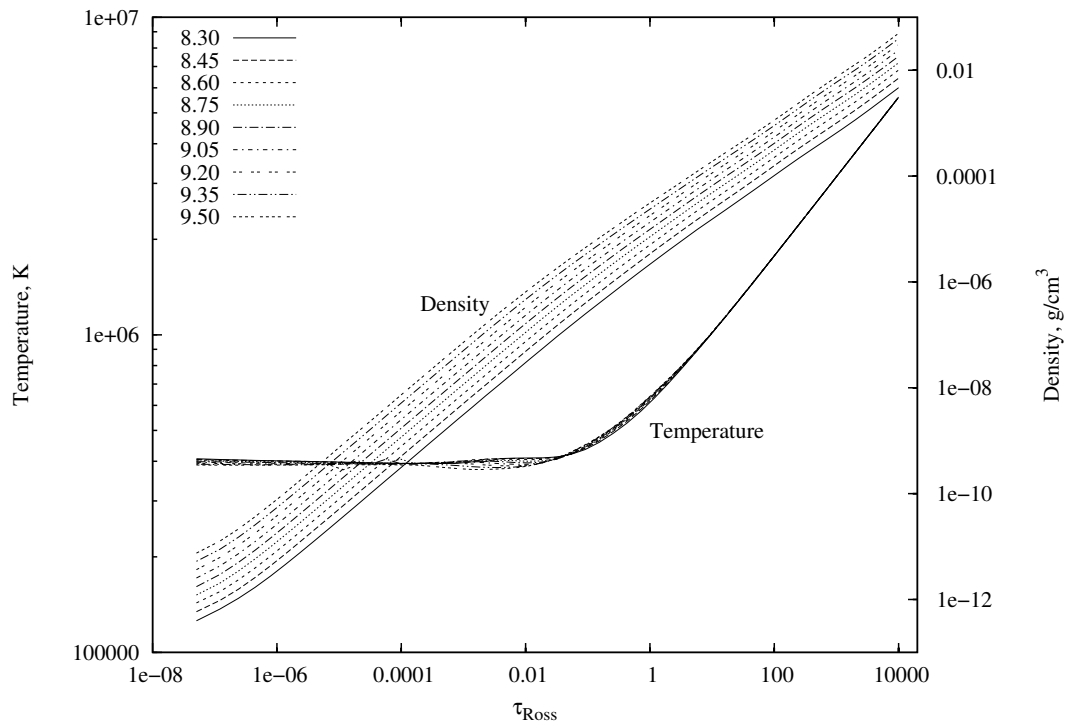


Figure 4.22: Effects of surface gravity on the atmospheric structure. Models were calculated with same composition, at effective temperature of 600,000 K, gravity is indicated in cgs units.

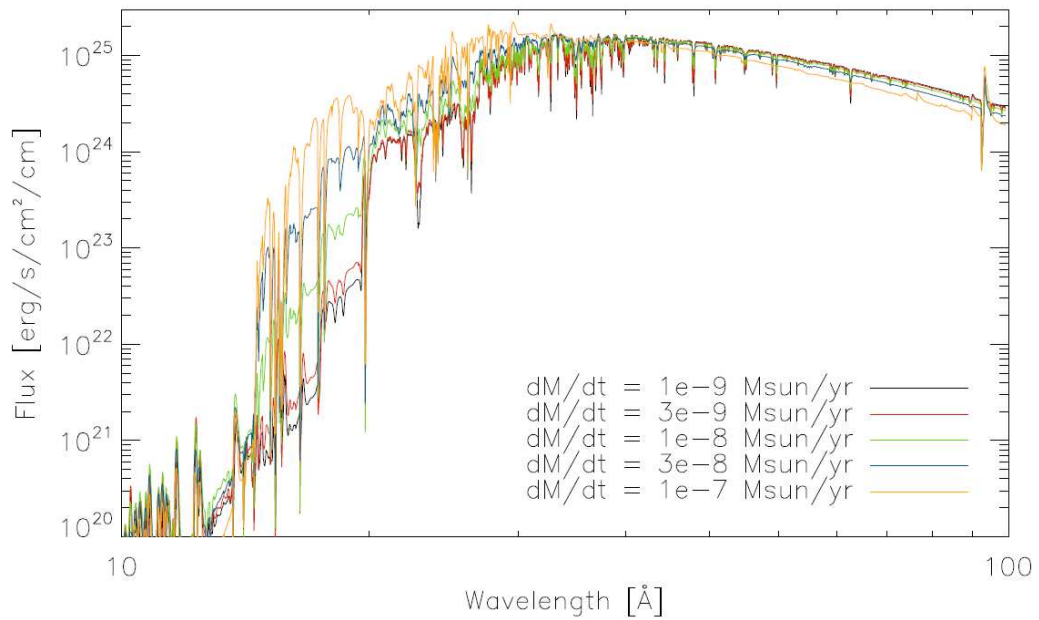


Figure 4.23: Impact of the mass-loss rate on the spectrum. Five spectra are shown at different mass loss rates calculated with PHOENIX with  $T_{\text{eff}} = 600,000 \text{ K}$  and  $v_{\infty} = 2400 \text{ km/s}$ . Figure is taken from van Rossum and Ness (2010).

## Temperature sequence

Other interesting trend is how the effective temperature changes the energy distribution. This sequence can be seen in Figure 4.24. At high energy an opposite effect can be seen like at the gravity sequence, increasing temperature decreases the ionization edges and makes the spectra harder. The change of the ionization balance can also be noticed when the relative strengths of Ly $\alpha$  lines of N VI (28.8 Å) and N VII (24.8 Å) are compared. Figure 4.25 shows the structure of model atmospheres when

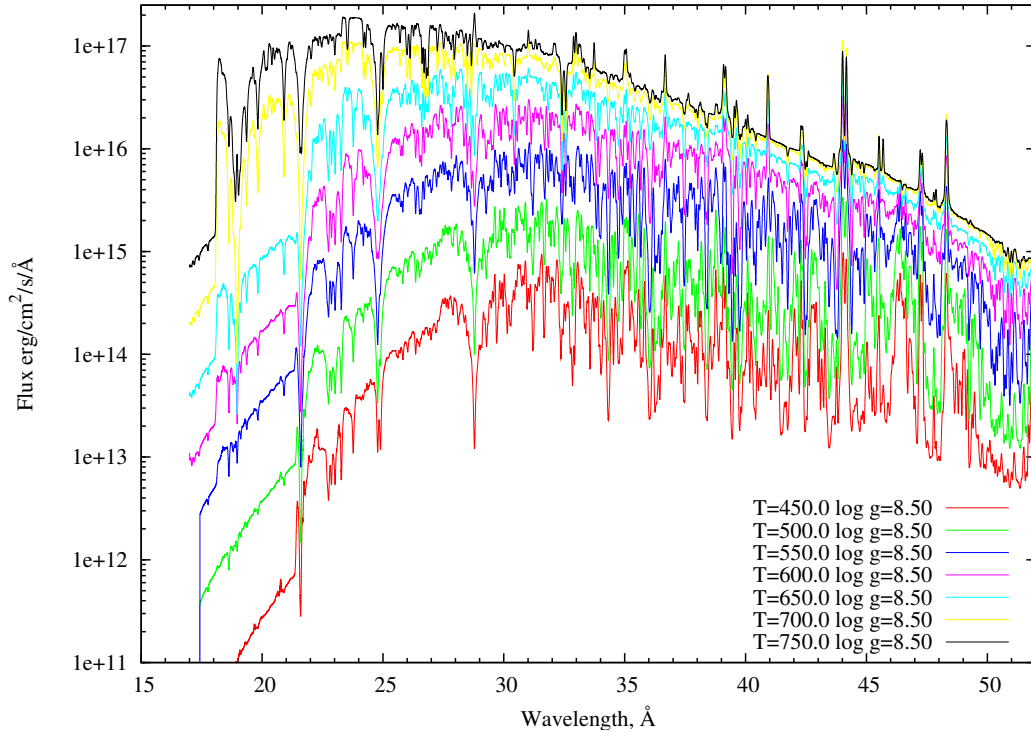


Figure 4.24: Temperature sequence. Models were calculated from  $T_{\text{eff}} = 450,000$  to  $750,000$  K with  $50,000$  K increments at  $\log g = 8.5 \text{ cm/s}^2$  and composition listed in Table 4.2.

only temperature was changed. The gravity and temperature profiles are independent from each other. Only a small change of the density can be seen and variations

around the photosphere are particularly small. The effective temperature scales the local temperature homogeneously throughout the atmosphere.

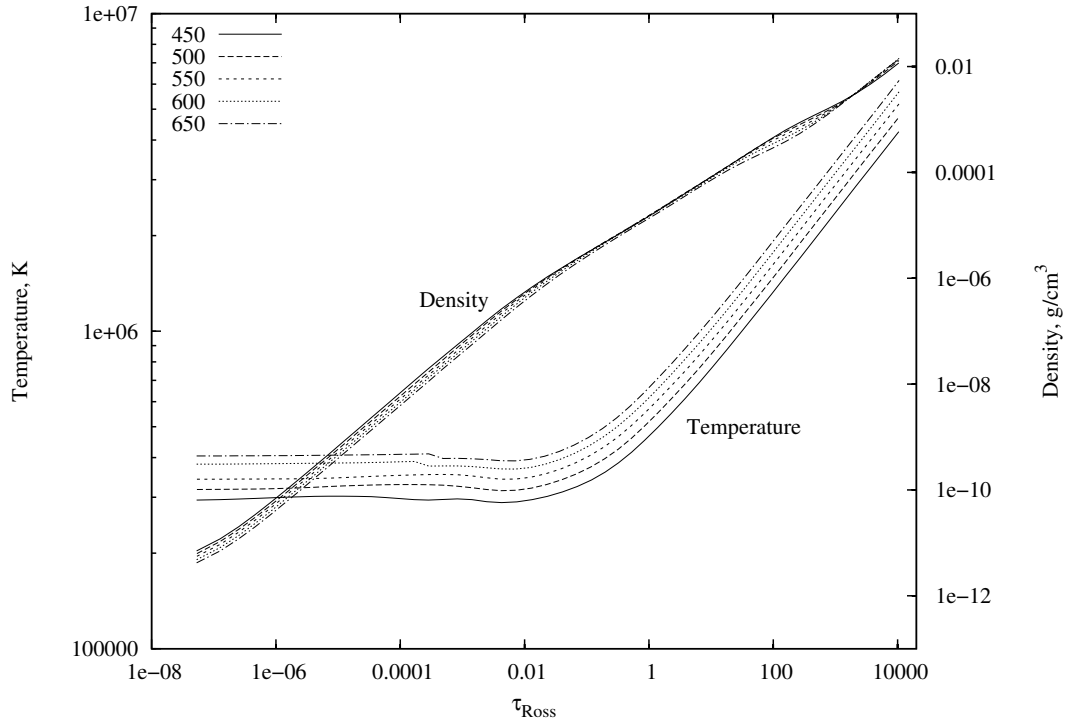


Figure 4.25: Effects of the effective temperature on the atmospheric structure.

### Temperature – Gravity sequence

From the characteristic changes of Figures 4.21 and 4.24 a more interesting trend can be outlined. By changing both the gravity and the temperature in a coordinated way, the two effects nearly cancel out and the spectra remain the same as shown in Figure 4.26. This approximately linear correlation along  $\log g = (0.011 \pm 0.0006)T + (1.8 \pm 0.4)$  at 550,000 K is valid at other temperatures as well. This correlation causes difficulty in determining the temperature and gravity and can lead to overestimation of both.

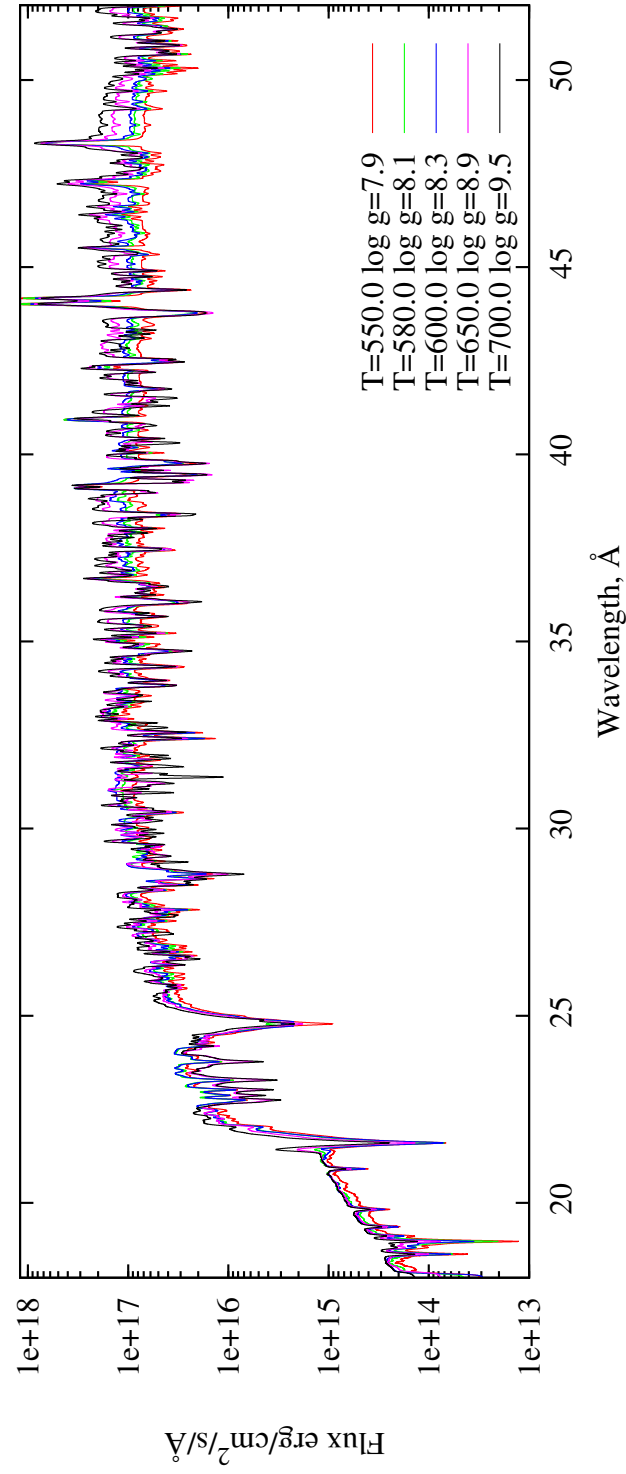


Figure 4.26: Change of spectral appearance when both temperature and gravity are varied.

## Close to the Eddington limit

The spectral appearance just below the Eddington limit was also investigated. Equation 4.5 was used to calculate the surface gravity for a given temperature at Eddington luminosity. Then to avoid convergence problems the surface gravity was increased by 0.1 dex for each model from  $T_{\text{eff}} = 433,000$  to  $T_{\text{eff}} = 933,000$  K. The spectral sequence of these models are shown in Figure 4.27. All models show a smooth continuum energy distribution with relatively weak ionization edges. Flux below  $25 \text{ \AA}$  is higher than for models with higher gravities. These features are also in accordance with the conclusion of van Rossum and Ness (2010) and Figure 4.23.

The strong absorption lines of N VII at  $24.8 \text{ \AA}$  and N VI at  $28.8 \text{ \AA}$  can be found in all spectra of the entire sequence. With increasing temperature and changing ionization balance both lines get weaker and the N VI  $28.8 \text{ \AA}$  line goes into emission. Due to the observed high abundance of nitrogen in novae these spectral lines are good indicators of effective temperature. Similarly, the lines of O VIII at  $18.97 \text{ \AA}$  and O VII at  $21.6 \text{ \AA}$  can be used for temperature diagnostics. However, these lines are present at higher temperatures where they are accompanied by strong continuum emission.

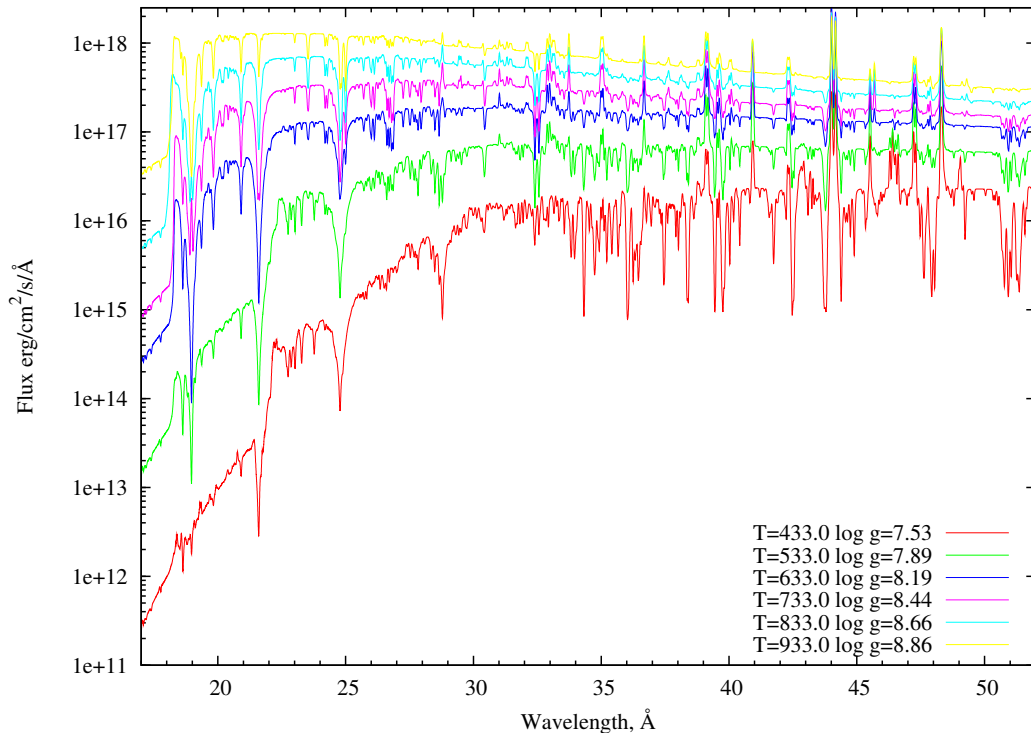


Figure 4.27: Model sequence close to the Eddington limit.

### Effects of different model atoms

Also important is to look at the effects of higher energy levels. This comparison can be seen in Figure 4.28, where spectra with two-level atoms and full model atoms are compared. These models were calculated at  $T_{\text{eff}} = 533,000$  K,  $\log g = 7.89$  cm/s<sup>2</sup> with identical abundances. The effects of opacities of the high energy levels are obvious. The new opacity sources redistribute the energy and make the spectrum softer. Some lines appear in emission with only a few energy levels in the model atoms, these are in absorption if higher levels are considered.

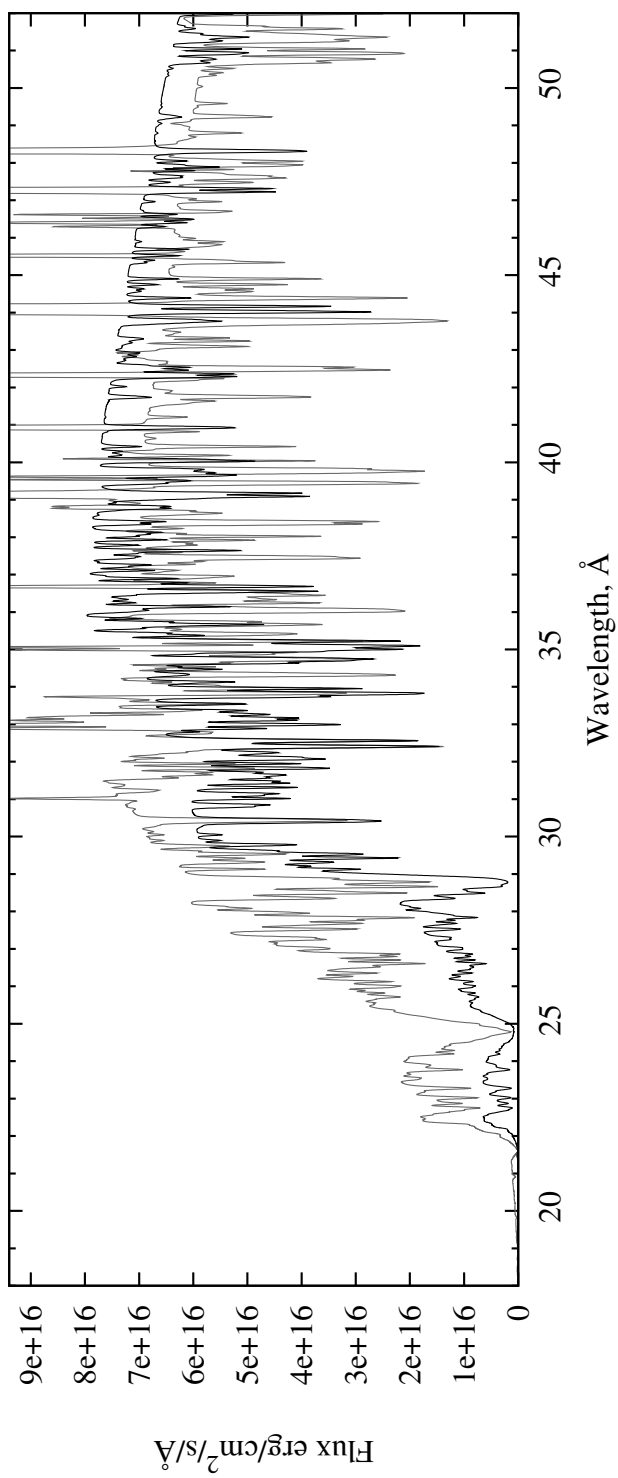


Figure 4.28: Effects of higher energy levels. Models were calculated at  $T_{\text{eff}} = 533,000$  K and  $\log g = 7.9$   $\text{cm/s}^{-2}$  with two-level atoms (grey) and full model atoms (black).



## Abundance sequence

The effects of individual abundances has already been shown for some elements in Figures 4.2 – 4.5, however abundances can be changed for all elements simultaneously. This was done for  $T_{\text{eff}} = 600, 500$  K and  $\log g = 8.23$  cm/s<sup>2</sup> at 1, 3, 10, 30, 100 and 10<sup>3</sup> times solar abundances and is shown in Figure 4.29. Model atoms with at most five levels were used to avoid convergence problems. These models show the important opacity of CNO elements below 25 Å, what significantly reduces the flux in this range. The strong line blanketing is also noticeable between 25 and 40 Å.

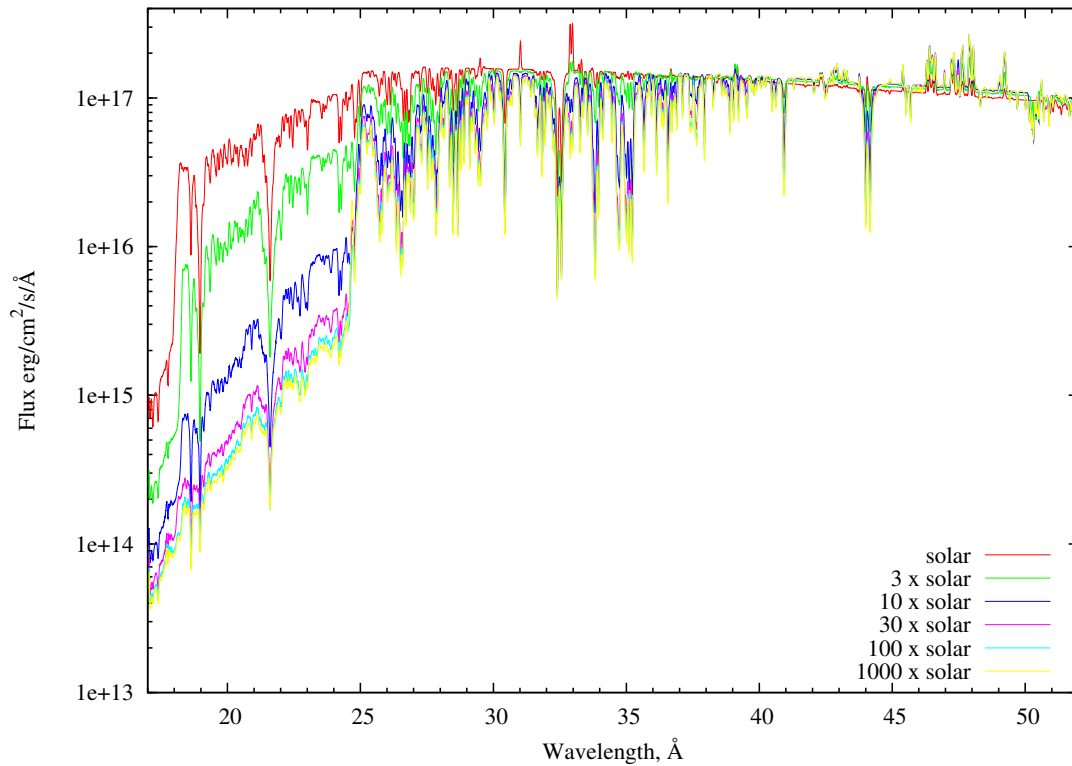


Figure 4.29: Effects of different metallicity. Models were calculated at  $T_{\text{eff}} = 600, 500$  K and  $\log g = 8.23$  cm/s<sup>2</sup> with solar, and 3, 10, 30, 100 and 10<sup>3</sup> times the solar values.

The temperature and density profiles for these atmospheres are shown in Figure

4.30. Temperature structure does not change in the inner part of the atmosphere where LTE is valid. At, and above the photosphere, however, differences are more prominent. The strong opacity introduced by spectral lines increases the temperature in the atmosphere by about 80,000 Kelvins when abundance was changed from solar to  $10^3$  times the solar value.

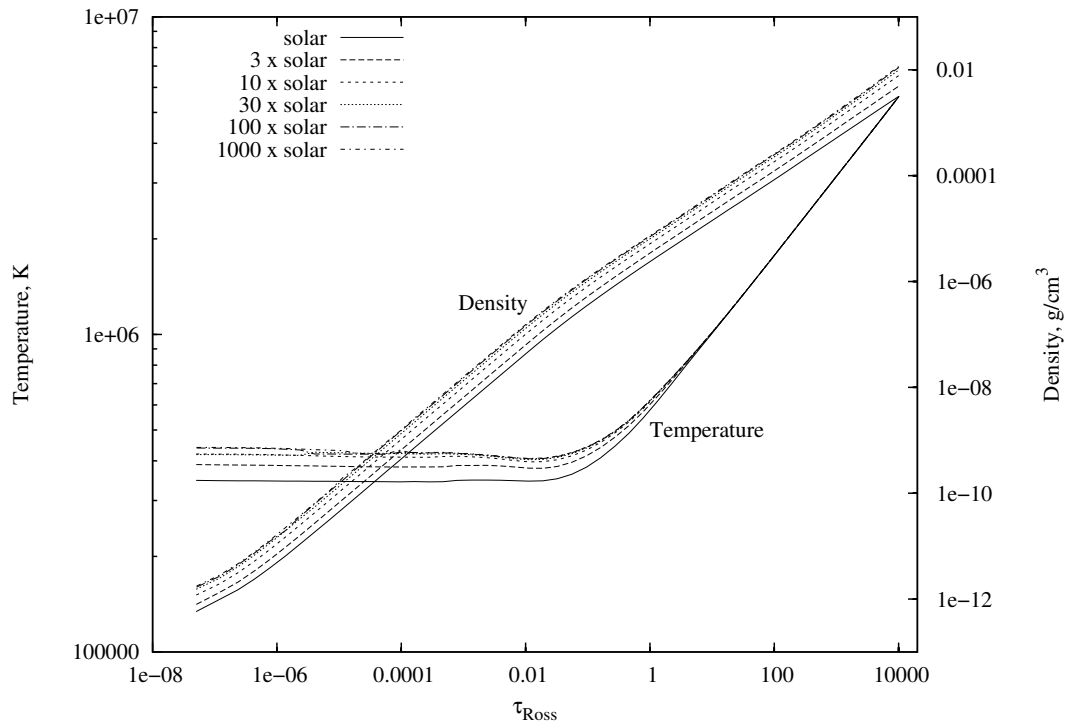


Figure 4.30: Temperature and density as function of Rosseland optical-depth at solar and 3, 10, 30, 100 and 1000 times solar abundances.

## Radial extension

The radial extension of model atmospheres can be derived from optical depth, opacity, mass-density and column-mass. TLUSTY provides these quantities for fully converged

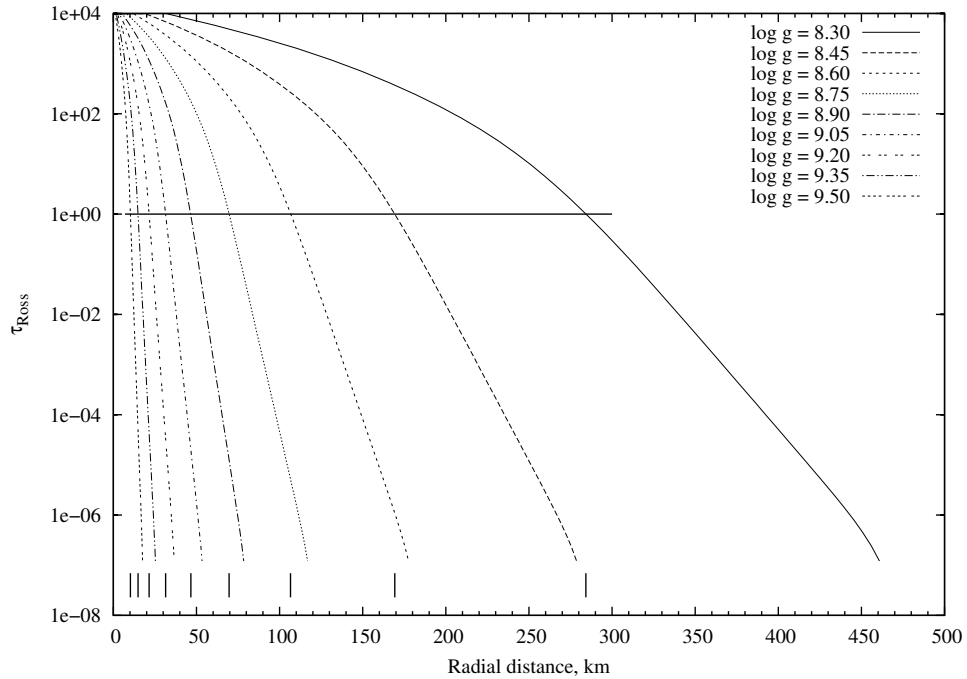


Figure 4.31: Radial size of atmospheres as function of surface gravity (WD mass). Models were calculated at  $T_{\text{eff}} = 600,000$  K and composition from Table 4.2 from  $\log g = 8.3$  to  $\log g = 9.5$   $\text{cm/s}^2$ . The photosphere was defined at  $\tau_{\text{Ross}} = 1$ , indicated by the horizontal line. Short vertical ticks at the bottom show the distance of the photosphere from base of the atmosphere ( $\tau_{\text{Ross}} = 10^4$ ) for each model.

models at each depth point. The photosphere is defined at  $\tau_{\text{Ross}} = 1$  from where about 37% of light escapes. Rosseland optical depths are shown in Figure 4.31 as function of radial geometrical distance in the atmosphere. The horizontal line at  $\tau_{\text{Ross}} = 1$  shows the location of the photosphere. Short vertical lines on the bottom of the graph help to read the radial distance between  $\tau_{\text{Ross}} = 10^4$  and 1. The size of the atmosphere grows progressively faster for lower surface gravities. Assuming that at low effective temperatures ( $T_{\text{eff}} < 50,000$  K) the radius of the atmosphere is negligible compared to the radius of the WD, one can use the mass-radius relationship to find the relative

size of the atmosphere at higher temperatures. At  $\log g = 8.3 \text{ cm/s}^2$  this is about 29%, at  $\log g = 8.5 \text{ cm/s}^2$  about 20% and at  $\log g = 9.0 \text{ cm/s}^2$  about 7% of the WD radius.

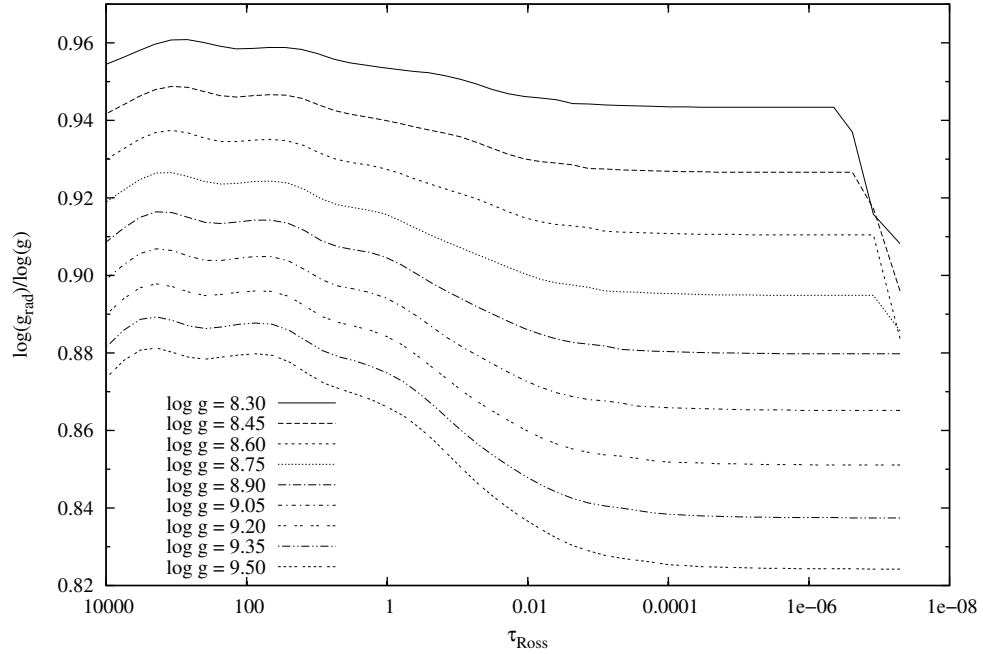


Figure 4.32: Radiation pressure as function of surface gravity. Atmospheric parameters are identical with those in Figure 4.31. Radiation pressure is expressed as fraction of the surface gravity for each model.

Figure 4.32 shows the radiation pressure versus optical depth at different surface gravities. The radiation pressure is expressed as fraction of the surface gravity. At  $\log g_{\text{Rad}}/\log g = 1$  the force by radiation balances gravity and the model cannot be considered hydrostatic. This transition happens for  $T_{\text{eff}} = 600,000 \text{ K}$  at around  $\log g = 8 \text{ cm/s}^2$ , however, due to numerical effects convergence breaks down around  $\log g = 8.3 \text{ cm/s}^2$ . This can be seen in Figure 4.32, the discontinuities at the top of the atmosphere grow larger for lower surface gravities. Models below  $\log g = 8.3 \text{ cm/s}^2$

failed to converge.

### 4.3 Comparison with TMAP

Figures 4.33 and 4.34 are comparisons between TMAP<sup>2</sup> and TLUSTY models, Figure 4.33 was taken from Rauch et al. (2005). TMAP (Tübingen NLTE Model Atmosphere Package) calculates stellar atmospheres in spherical or plane-parallel geometry in hydrostatic and radiative equilibrium. The spectra shown here were calculated in plane-parallel geometry. As both TLUSTY and TMAP share the same model assumptions, their outputs are comparative. Beside the general agreement of the results there are three important things to note: there are more lines in the TLUSTY model, the super-solar oxygen abundance causes much broader lines in the TLUSTY model, and the continuum is a factor of three higher than TMAP's when the Rauch et al. (2005) abundance ( $H/H_{\odot} = 1$ ,  $He/He_{\odot} = 10.26$ ,  $C/C_{\odot} = 0.007$ ,  $N/N_{\odot} = 0.544$  and  $O/O_{\odot} = 23.38$ ) was used. This can be seen at the flux levels of the solar spectra as well.

---

<sup>2</sup> <http://astro.uni-tuebingen.de/~rauch/TMAP/TMAP.html>

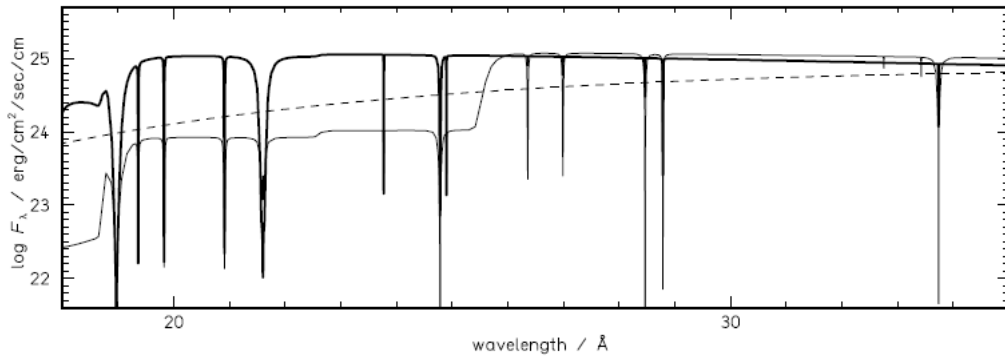


Figure 4.33: Comparison of fluxes for a model with  $T_{\text{eff}} = 700,000$  K and  $\log g = 9.0$  cm/s<sup>2</sup> at different abundance ratios. The thin line shows solar composition and the thick line was calculated at  $\text{H}/\text{H}_{\odot} = 1$ ,  $\text{He}/\text{He}_{\odot} = 10.26$ ,  $\text{C}/\text{C}_{\odot} = 0.007$ ,  $\text{N}/\text{N}_{\odot} = 0.544$  and  $\text{O}/\text{O}_{\odot} = 23.38$  by number. Both models were calculated with TMAP (Rauch et al., 2005). Dashed line is a blackbody model.

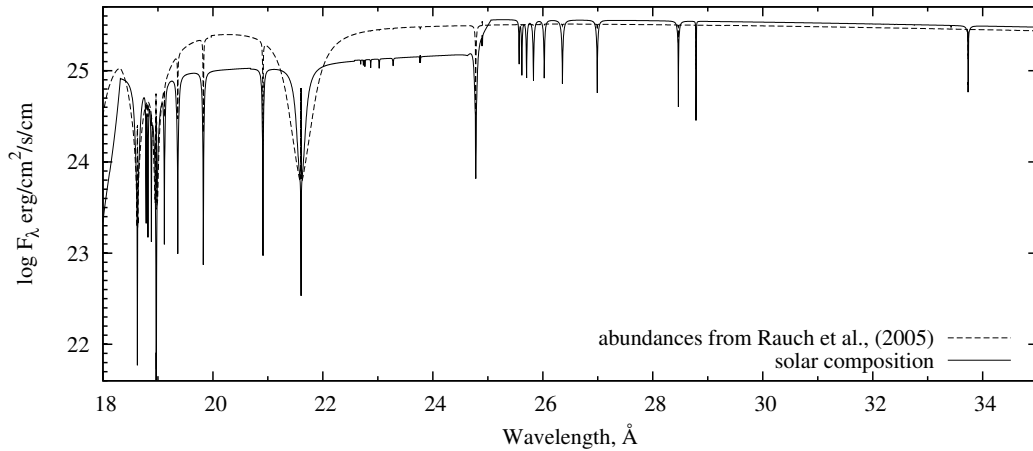


Figure 4.34: Same models as in Figure 4.33 calculated with TLUSTY. Thin line shows solar abundance, the other was calculated with abundance ratios used by Rauch et al. (2005).

## Chapter 5

# Observations of Classical Novae

X-ray measurements of celestial objects began with the era of space-borne observatories and the Einstein Observatory (HEAO-2) in 1978. During its three-year mission, Einstein discovered numerous X-ray sources in the Andromeda Galaxy and the Magellanic Clouds, conducted deep X-ray surveys and discovered that coronal emission in normal stars is stronger than expected. Einstein's observations also helped the morphological studies of supernova remnants. It was followed by EXOSAT from 1983 to 1986. EXOSAT observed Low Mass X-ray Binaries, pulsars and AGN variability. The first nova detected by EXOSAT in soft X-rays was GQ Mus 1983.

An important breakthrough came with the launch of ROSAT in 1990. Its higher sensitivity, resolution and nine year mission significantly contributed to the advancement of high energy astrophysics. The new class of Supersoft X-ray Sources (SSS) was discovered with ROSAT. They were thought to be white dwarfs accreting matter from a binary companion star at a rate sufficient to produce steady nuclear burning

on the white dwarf surface, or perhaps classical novae after outburst. However, due to the relatively low resolution of ROSAT only the spectral energy distribution (SED) was measurable and not line spectra. Unlike other accreting X-ray binaries where the gravitational potential energy powers the X-ray source nuclear burning is the primary energy source in SSS. That their SED can not be sufficiently modeled by black bodies, so detailed white dwarf atmosphere models are essential was realized by MacDonald and Vennes (1991). ROSAT observed 30 galactic and nine LMC novae for up to ten years and found only three of them (V1974 Cyg 1992, GQ Mus 1983 and N LMC 1995) active in soft X-rays, (Orio et al., 2001).

Detailed modeling requires even higher resolution spectra than ROSAT provided. Since 1999 Chandra and XMM-Newton observatories have met this need. These are the data sources that provide sufficiently high resolution observations for my work. In the next sections I give more details on them. Also worth mentioning are the RXTE, Swift, INTEGRAL, Suzaku, BeppoSAX X-ray satellites; their measurements also greatly contributed to the study of supersoft sources, although this study does not use these data.

## 5.1 Chandra

Chandra was launched by Space Shuttle Columbia on July 23, 1999. It was the third of NASA's four Great Observatories. Its original mission was planned for five years. Chandra has an elliptical orbit with a 133,000 km apogee and a 16,000 km perigee with  $28.5^\circ$  inclination to the ecliptic and a period of 64.2 hours. This allows integrations



of up to two days.

The scientific instruments include the High-Resolution Mirror assembly (HRMA), the Low and High-Energy Transmission Gratings (LETG and HETG), and the Science Instruments Module (SIM) which has two focal plane instruments, the Advanced CCD Imaging Spectrometer (ACIS) and the High Resolution Camera (HRC). Since it is relevant to this subject the HRMA, LETG and the HRC are explained below in detail.

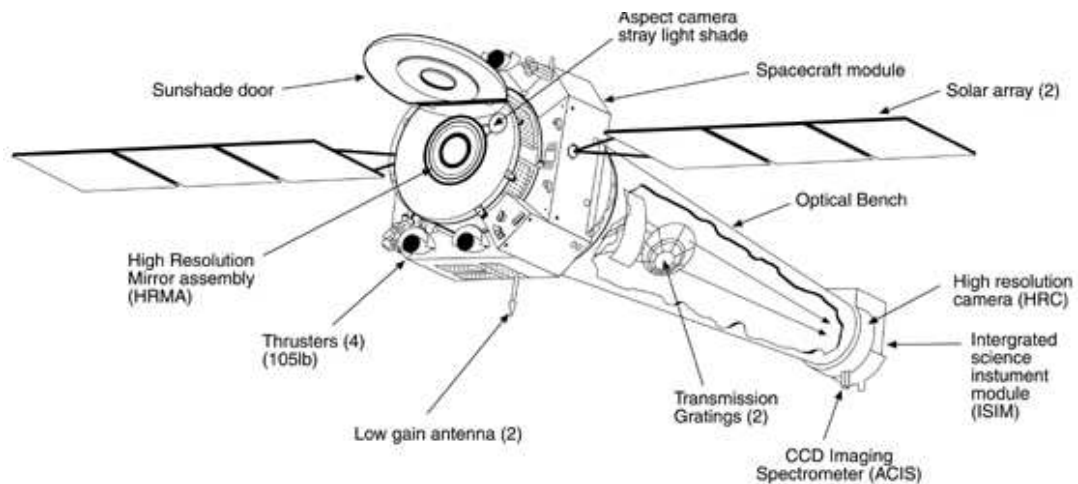


Figure 5.1: The Chandra Observatory. Source: <http://www.shuttlepresskit.com/STS-93/payload45.htm>

The HRMA consists of four pairs of mirrors with focal length of 10 m. Mirrors are coated with iridium and the pair diameters range from 0.65 m to 1.23 m. Their total effective area is 1100 cm<sup>2</sup>. The LETG is located behind the HRMA and can be rotated into the converging beam to disperse X-rays to the focal plane where X-rays can be recorded by either HRC or ACIS. Both cameras have spectroscopy and imaging modes. The LETG consists of 180 segments having three modules each.

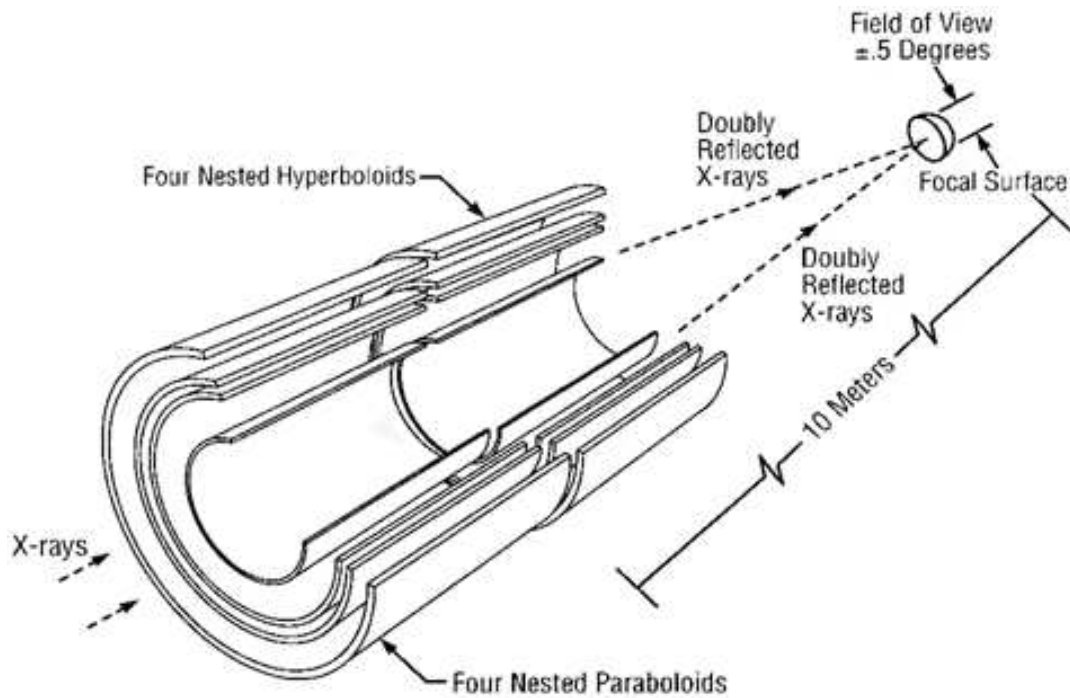


Figure 5.2: The structure of HRMA. Source: <http://www2.jpl.nasa.gov/basics/axafmirror.gif>

These modules have gold wires with about 991 nm spacing and provide a high spectral resolution  $E/\Delta E \approx 10^3$  in the 80 – 175 Å range and moderate resolution  $E/\Delta E \approx 20$  between 3 and 50 Å. LETG is most commonly used for studies of on-axis observations of bright point sources. The LETG/HRC-S combination is used for high resolution spectroscopy of soft sources such as WDs and cataclysmic variables.

The HRC is a 10 cm<sup>2</sup> microchannel plate instrument with two detectors: the HRC-I is optimized for imaging and the HRC-S is for spectroscopy. The HRC-S is well-suited to serve as the readout detector for the LETG; it can also be used in a very fast readout timing mode. The HRC provides a 30×30 arcmin field of view in imaging mode, and a 6×99 arcmin field in spectroscopy mode.

Chandra is the primary data source in this dissertation, since its spectral window covers the entire supersoft range and has the necessary resolution for spectral modeling.

## 5.2 XMM-Newton

XMM-Newton was launched on Dec 10, 1999 by an Ariane 5 rocket from Guiana Space Center at Kourou. Its orbit is a very eccentric 48 hour ellipse with  $40^\circ$  inclination. Its apogee is 114,000 km and perigee is only 7000 km. Similar to Chandra, the eccentric orbit makes long exposures possible, here up to 40 hours.

Scientific instruments related to my work are the Telescopes, the two Reflection Grating Spectrometers (RGS) each consisting of a Reflection Grating Array (RGA) and an RGS Focal-plane Camera (RFC).

XMM is equipped with three X-ray telescopes, each of them consists of 58 Wolter I type grazing-incidence mirrors nested in a coaxial and confocal configuration. The diameter of the largest mirror is 70 cm, which are made of gold-coated nickel. Two telescopes are equipped with RGAs, which disperse about 58% of collected light at the RFCs in the secondary focus. About 42% of the light is directed to the EPIC MOS cameras in the prime focus. The third is an open X-ray telescope for imaging. The total effective area of the three telescopes is  $4650 \text{ cm}^2$  and their focal length is 7.5 m with PSF (FWHM) 6 arcsec (HEW = 15 arcsec).

The grating plates in the RGAs have mean groove densities of about 645.6 lines/mm. Dispersion is a varying function of dispersion angle; at  $15 \text{ \AA}$  it is about  $8.3 \text{ mm/\AA}$  in

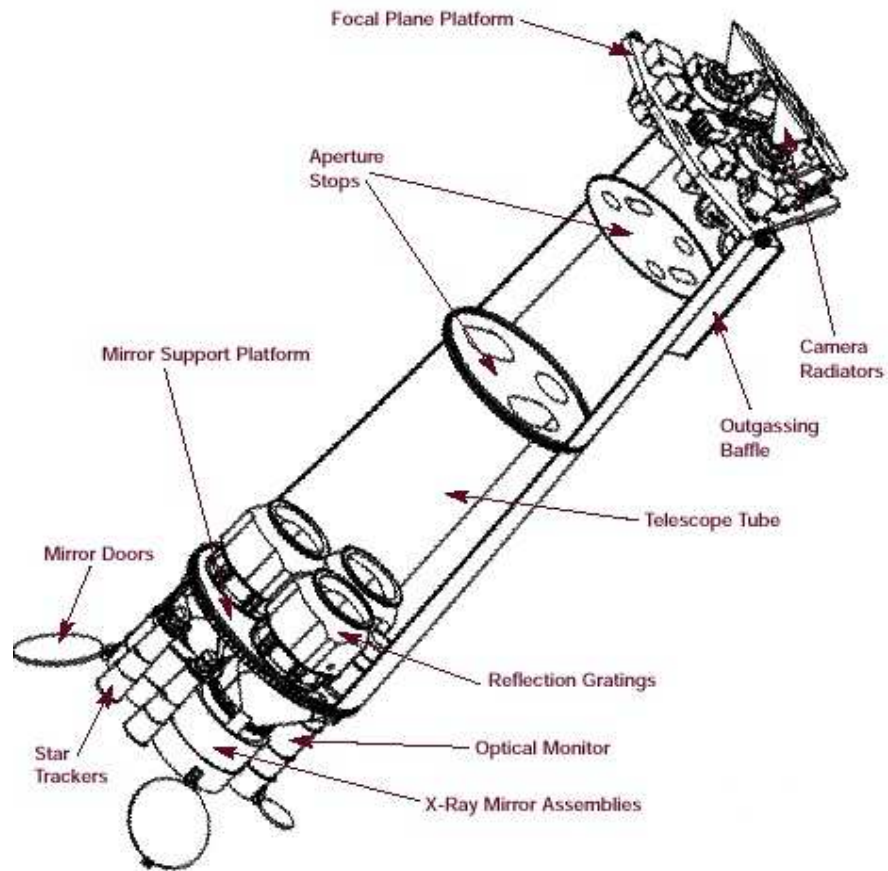


Figure 5.3: The XMM-Newton Observatory. Source: [http://xmm.esac.esa.int/external/xmm\\_user\\_support/documentation/technical/Spacecraft/barrel.jpg](http://xmm.esac.esa.int/external/xmm_user_support/documentation/technical/Spacecraft/barrel.jpg)

first order. The wavelength accuracy is  $7 \text{ m}\text{\AA}$  ( $1 \sigma$ ) or better for both RGS1 and RGS2.

RFCs consist of linear arrays of nine MOS CCD chips along the dispersion axis. The chips are back-illuminated to maximize the soft energy response and aluminum coated on the exposed side to suppress UV and optical light. Each detector has  $1024 \times 768$  ( $27 \mu$ ) pixels, half-exposed to the sky and half used as storage area. At readout, pixels are binned to  $81 \mu\text{m}$ , which is sufficient to fully sample the RGS line spread function.

One bin corresponds to about 7, 10, and 14 mÅ in first order for wavelengths of 5, 15, and 38 Å. Due to CCD failures on orbit, effective areas are reduced by half between 20 and 24.1 Å for RGS1 and between 10.6 and 13.8 Å for RGS2.

Although XMM-Newton has a narrower spectral window (5-38 Å) than Chandra, there are many K-shell transitions and He-like triplets of C, N, O, Ne, Mg and Si, and L-shell transitions of heavier elements in its range. Furthermore, beyond 40 Å the strong interstellar absorption limits X-ray spectroscopy. Thanks to its higher sensitivity and contribution to temporal coverage, XMM data complements the Chandra observations.

### 5.3 Data Reduction

Instead of CIAO, the X-ray data analysis software of Chandra, a simpler procedure was applied. From the primary data products, the spectra were extracted by using the tasks of IRAF<sup>1</sup> and STSDAS<sup>2</sup> for binary tables. Positive and negative first-order spectra were processed separately and coadded to increase signal-to-noise ratio. The effective area contains the properties of the telescope, the gratings and the detector system. This function describes the total efficiency of the instrument. With its help one can convert count rate to photon counts. The first order effective area for the negative arm of LETG can be seen in Figure 5.4.

XMM-Newton data reduction was done in SAS version 8.0.1., using the standard

---

<sup>1</sup><http://iraf.noao.edu/>

<sup>2</sup>[http://www.stsci.edu/resources/software\\_hardware/stsdas](http://www.stsci.edu/resources/software_hardware/stsdas)

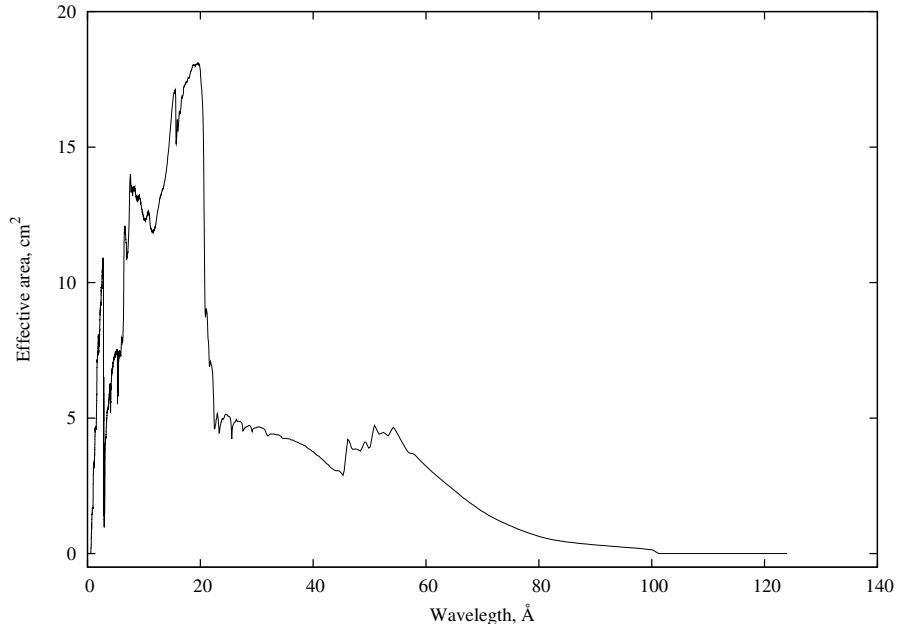


Figure 5.4: LETG first order effective area for V4743 Sgr.

procedure presented for point-like sources on XMM's page<sup>3</sup> and in The XMM-Newton ABC Guide<sup>4</sup>. Calibration files were checked and updated automatically at startup. Data processing was kept minimal, and only good time intervals (GTI) and background subtraction were applied. Light curves were extracted and displayed to filter out flares. During flares an abnormal high count rate can be identified over a short period of time what is not related to the source. During X-ray-on stages sources were bright enough and did not need rebinning.

<sup>3</sup>[http://xmm.esa.int/sas/current/documentation/threads/rgs\\_thread.shtml](http://xmm.esa.int/sas/current/documentation/threads/rgs_thread.shtml)

<sup>4</sup><http://heasarc.nasa.gov/docs/xmm/abc/>

## 5.4 Interstellar absorption

Interstellar absorption is an important and poorly understood factor in X-ray modeling. The extinction curve is changing rapidly with wavelength. About 40% of light extinction can be accounted for by interstellar matter around 20 Å and about 94% at 50 Å (Lanz et al., 2005). In my work I used the interstellar abundance and absorption cross-sections for the 17 astrophysically important elements from Morrison and McCammon (1983) and Bałucińska-Church and McCammon (1992)<sup>5</sup>. Instead of their polynomial fits, I used their functions to calculate the total absorption cross-section at each data point individually.

I considered interstellar extinction as a sum of the standard Galactic extinction plus the contribution of the circumstellar material. Galactic extinction was calculated from published hydrogen column-densities ( $N_{\text{H}}$ ) and relative interstellar abundances ( $a_i^{\text{mm}}$ ) from Morrison and McCammon (1983) using the formula:

$$\varphi(E, N_{\text{H}}, a_1^{\text{mm}}, \dots, a_{17}^{\text{mm}}) = e^{-N_{\text{H}} \sum_i a_i^{\text{mm}} \chi_i(E)}, \quad (5.1)$$

where  $\chi_i(E)$  is the photoelectric absorption cross-section of element  $i$  at energy  $E$ . If there were no available data on column density I estimated the standard extinction based on the distance of the object (Binney and Merrifield, 1998):

$$N_{\text{H}} \approx 3.1 \times 10^{21} \left( \frac{d}{\text{kpc}} \right) \frac{1}{\text{cm}^2}. \quad (5.2)$$

---

<sup>5</sup><http://cdsweb.u-strasbg.fr/viz-bin/Cat?VI/62>.

This provided a starting point for estimating the Galactic absorption along the line of sight at each observed wavelength. However, Equation 5.2 overestimates the column density for each nova. Their values were determined from model fits.

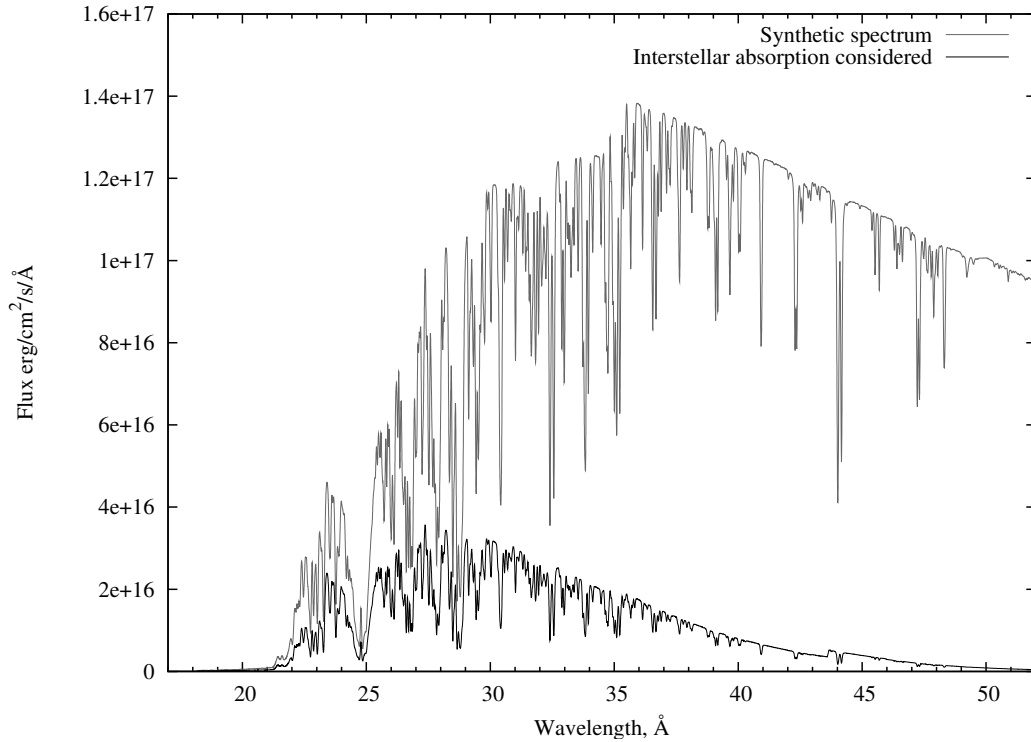


Figure 5.5: Correction for interstellar absorption. Galactic abundance was taken from Morrison and McCammon (1983) and a hydrogen column density  $N_H = 4 \times 10^{20}$  was used.

Also important is the extinction due to circumstellar material, which is even more difficult to take into account for novae. The composition of the shell, its clumpiness, geometry and evolution make this a very complex problem. The column density of the shell can change significantly over time as well. Assuming that the composition of circumstellar material reflects the composition of the nova shell, I modified the



individual abundances in Equation 5.1:

$$a_i^{total} = a_i^{mm} + C a_i^{cs} \quad (5.3)$$

where  $a_i^{cs}$  is the abundance of a given element relative to hydrogen by number density in the shell and  $C$  is a scaling parameter which describes the amount of excess hydrogen in the column relative to the standard column density.

## 5.5 Instrumental resolution

The instrumental profiles of both Chandra and XMM was considered to be Gaussian. The spectral resolution of XMM's RGS spectrometers can be seen in Figure 5.6. Only first-order spectra were used in my work. These were approximated with linear functions between 10 and 60 Å. Here  $\lambda_s$  is the numeric value of the wavelength without unit, taken as the slope:

$$\text{RGS1 : } \quad \frac{\lambda}{\Delta\lambda} = 17.66\lambda_s - 33.33 \quad (5.4)$$

$$\text{RGS2 : } \quad \frac{\lambda}{\Delta\lambda} = 21\lambda_s - 35 \quad (5.5)$$

and for Chandra LETG/HRC-S:

$$\text{Chandra : } \quad \frac{\lambda}{\Delta\lambda} = 20\lambda_s. \quad (5.6)$$

However, the difference in resolution between the instruments is practically neg-

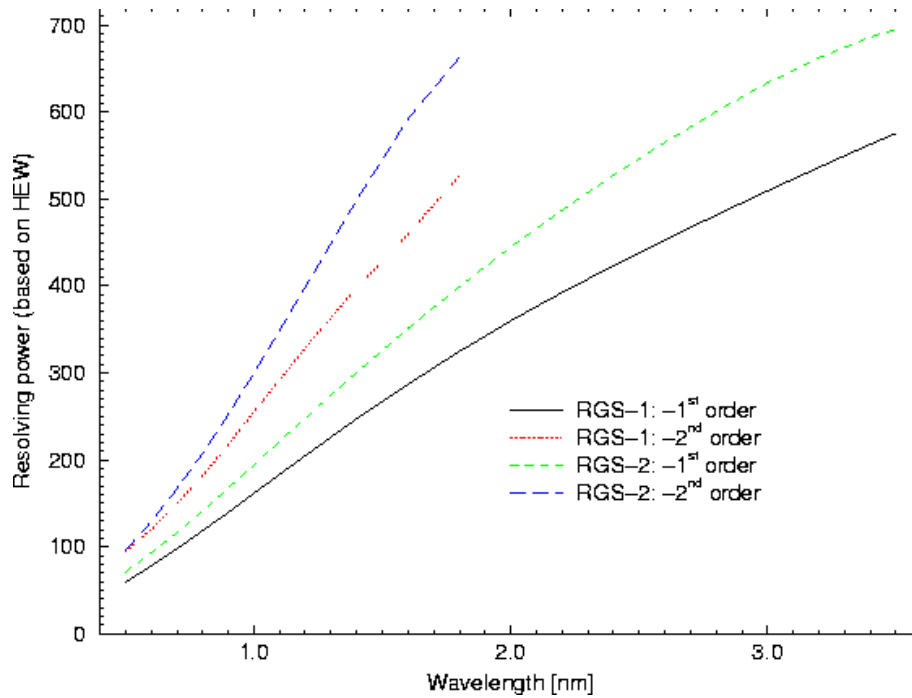


Figure 5.6: Spectral resolution of XMM's RGS instruments, (Dahlem, 1999)

ligible. Figure 5.7 is a plot of a synthetic and a convolved model spectrum at the Chandra resolution. The convolution function was calculated and normalized for the resolution of each data point. Next the spectrum was evaluated with a variable step size to sample both the synthetic spectrum and the Gaussian well and the flux was then linearly interpolated for locations of the Gaussian sampling points. Figure 5.8 shows the sampling of the kernel function.

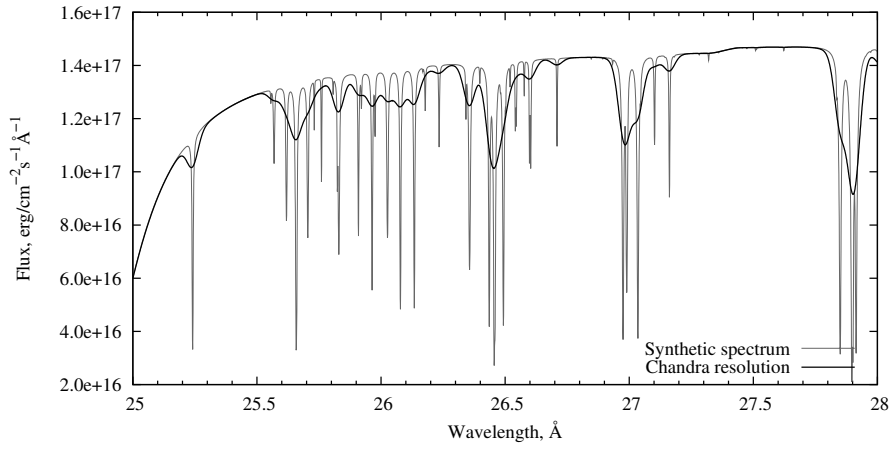


Figure 5.7: Correction for instrumental resolution.

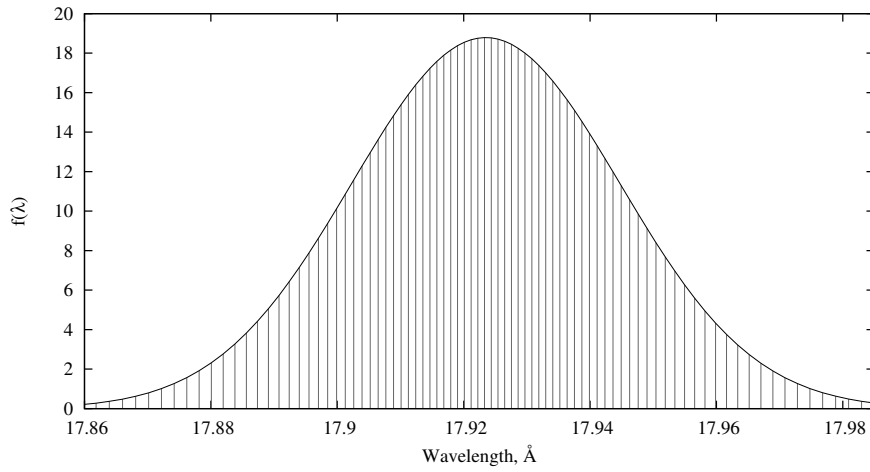


Figure 5.8: Sampling of the convolution function for the calculation of the instrumental resolution.

## 5.6 Application to Observations

In this chapter, I present public data on V4743 Sgr and V2491 Cyg retrieved from the Chandra and XMM data archives. The data on these two targets and the recurrent nova RS Oph are the most comprehensive data sets available on CNe. However, both V2491 Cyg and RS Oph proved to be too luminous for static modeling. Their spectra showed strong continuum emission below  $18 \text{ \AA}$  what can be reproduced only at relatively high effective temperatures and low surface gravities. This regime lies in the super Eddington area indicated in Figure 4.7 and cannot be modeled with TLUSTY. Both the Chandra and XMM observations are released after one year of proprietary periods. As the duration of the supersoft stage is relatively short, lasting only a few months, and novae appear randomly, scheduling observations is difficult and mostly done as targets of opportunity.

### 5.6.1 V4743 Sgr

V4743 Sgr (Nova Sgr 2002c) was discovered on September 20, 2002 by Haseda et al. (2002) at its optical maximum of  $V = 5^m$ . It was a very fast nova ( $t_3 = 15$  days) and showed large expansion velocities. The FWHM of  $H_\alpha$  reached 2400 km/s. The distance to the nova is uncertain, but estimated to be about 6.3 kpc by Lyke et al. (2002),  $3.9 \pm 0.3$  kpc by Vanlandingham et al. (2007) and  $1.2 \pm 0.3$  kpc by Nielbock and Schmidtobreick (1997). This makes direct radius and mass determinations impossible. In March 2003 this nova was the brightest supersoft source in the sky. It was a target of Chandra and XMM observatories over the following 18 months. Follow up observations

were made three years later. The log of observations can be found in Table 5.6.1 and the spectral evolution is shown in Figure 5.6.1.

Table 5.1: Chandra LETG/HRC-S and XMM RGS X-ray observations of V4743 Sgr.

Observation ID	Date	Exposure (s)	Instrument	comment
3775	2003/03/19	24713	Chandra LETG/HRC-S	X-on
0127720501	2003/04/05	35214	XMM RGS	X-on
3776	2003/07/18	11681	Chandra LETG/HRC-S	X-on
4435	2003/09/25	11485	Chandra LETG/HRC-S	X-on
5292	2004/02/28	10237	Chandra LETG/HRC-S	X-on
0204690101	2004/10/01	22317	XMM RGS	X-off
0304720101	2006/03/29	33896	XMM RGS	X-off

V4743 Sgr was observed on March 19th and April 4th by Chandra and XMM, respectively. A comparison of these spectra is shown in Figure 5.10. There were only 16 days between the two observations, so the flux level did not change much; it was around 0.2 cts/s in both observations, or at  $1.5 \times 10^{-10}$  erg/cm<sup>2</sup>/s/Å. However the peak flux decreased in April and line strengths of both nitrogen and oxygen decreased compared to the earlier spectrum, while the high energy flux below 23 Å increased. However, the line strength variations are minor effects. By mid-July the peak of the observed energy distribution reached  $1.9 \times 10^{-10}$  erg/cm<sup>2</sup>/s/Å followed by a gradual decrease to  $1 \times 10^{-10}$  erg/cm<sup>2</sup>/s/Å in September 2003 and to  $2 \times 10^{-11}$  erg/cm<sup>2</sup>/s/Å in February 2004. V4743 Sgr was visited later by XMM and no measurable X-ray spectra was found. It is important to note that supersoft sources in general show rapid variability up to 40% of the total X-ray flux. In novae this can be modulated further by the orbital period of the binary. Leibowitz et al. (2006) found six periodicities, ranging from a

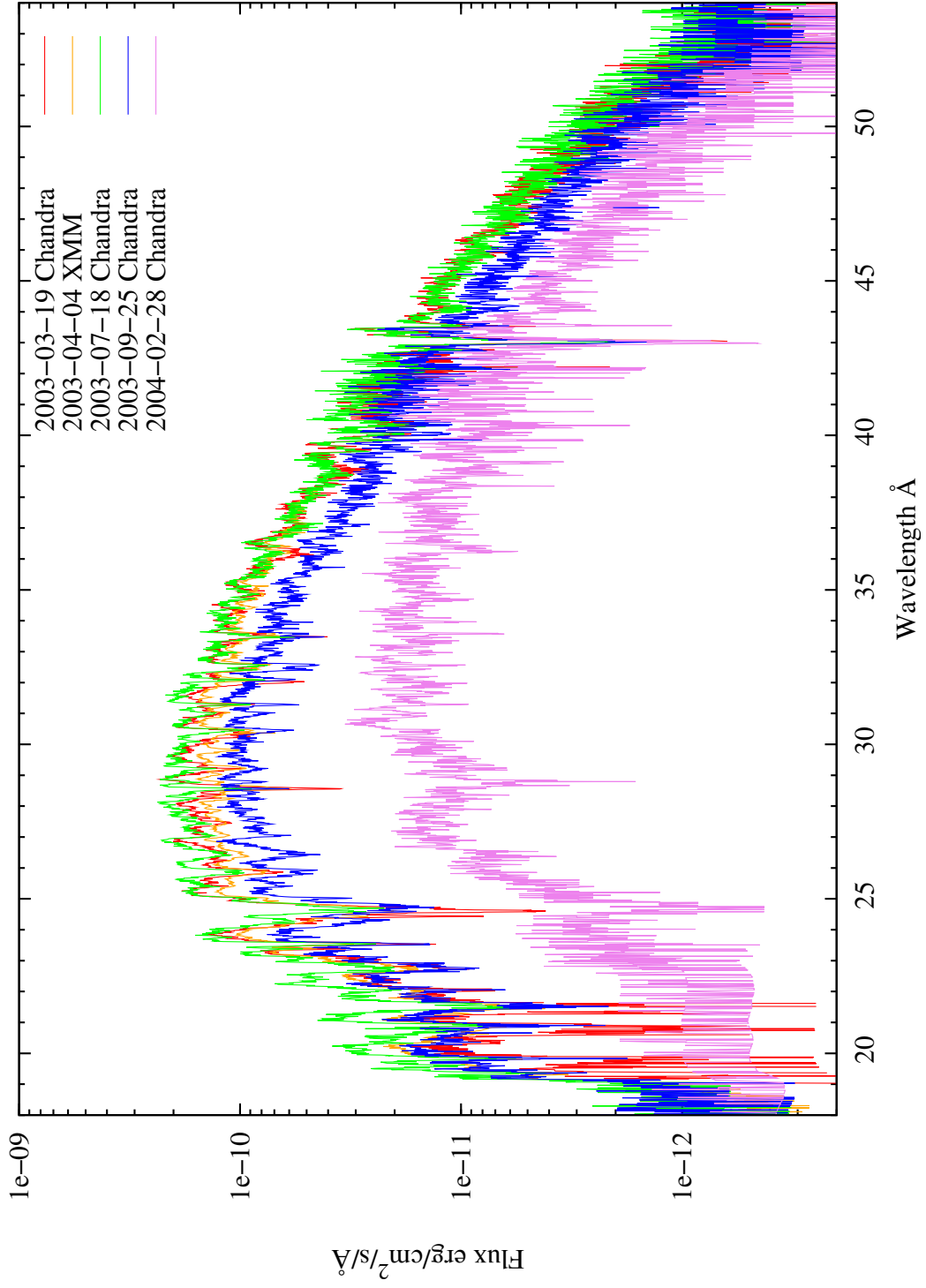


Figure 5.9: Spectral evolution of V4743 Sgr between March 2003 and February 2004.

few hundred seconds up to six hours. Two variations were particularly intense, with periods 1371 and 1310 seconds. The sum of these two frequencies was also identified. These rapid variations may be related to the spin of the WD and/or to non-radial pulsations. The relatively short timescale of these variations relative to the length of spectroscopic observations were not accounted for in this work. However, there was a dramatic change during the March 2003 observation. At around 20,000 seconds into the the observation the flux suddenly faded more than two orders of magnitude. This variation might be related to the 6.6 hours orbital period also observed in the optical or to other not yet identified mechanism. To account for this event the last 5000 seconds of the March 2003 spectrum was deleted.

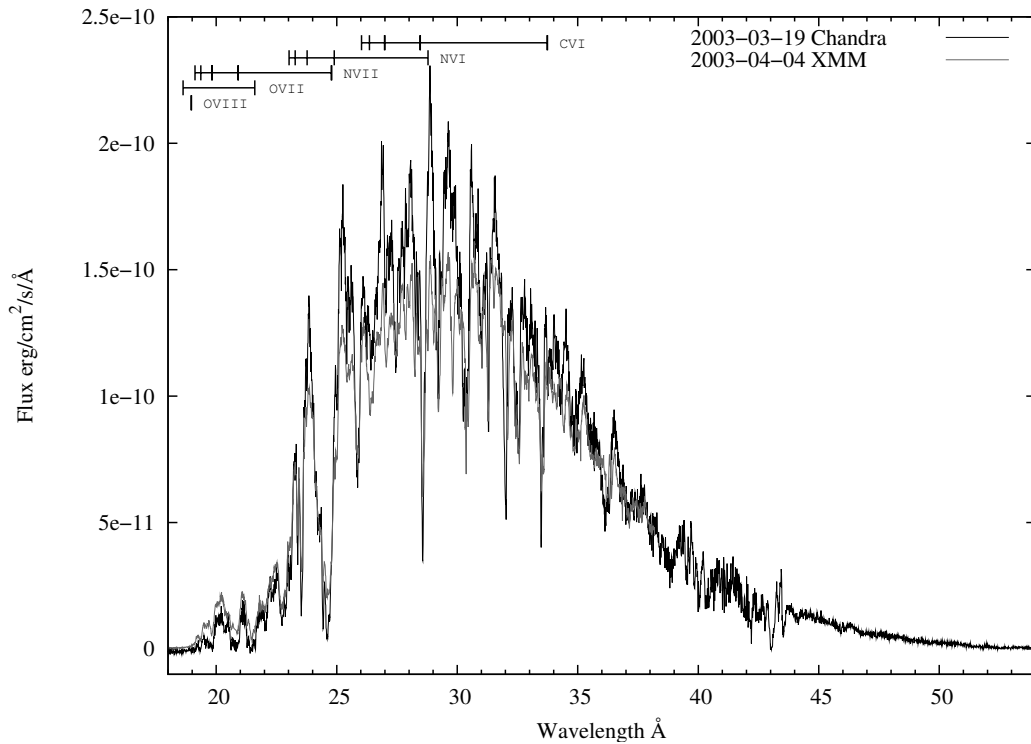


Figure 5.10: Comparison of Chandra LETG/HRC-S and XMM RGS observations.

The strong resonance lines of nitrogen and oxygen in the spectrum suggest over-abundance of these elements. A hydrogen deficiency and element ratio of  $N/C \approx 1000$  and  $N/O \approx 50$  is a signature of CNO-cycle processed material and typical for novae (Clayton, 1968). Such extreme compositions were not seen here, but the super abundances of these elements relative to the Sun are obvious. The model composition was set up according to this over-abundance of light metals, keeping all other elements at their solar value. However, models can be fit with an increased abundance of Ne, Mg, Al, and Si, as shown in Table 4.2. Individual element abundances are very uncertain. The most reliable values could have been set up for nitrogen and oxygen; for them uncertainties are  $\pm 20\%$ . Confining the error ranges of other element abundances are more difficult. Helium is about four to ten times more abundant than in the solar atmosphere. It changes the spectral distribution homogeniously and does not have lines in this range. However, a helium abundance over ten times the solar value raised convergence problems. Carbon is somewhat different, as it regulates the flux at the high energy end. Its spectral lines do not show up at the calculated abundances and models failed to converge with an increased amount of carbon. Based on its expected effects on the continuum the estimated abundance error is  $\pm 40\%$  for carbon. Neon and aluminum showed very similar behavior to helium. Neon does not have spectral lines in the part of the spectrum where both the signal-to-noise ratio is good and the interstellar absorption is low. It does not make a significant contribution to the spectrum up to 100 times the solar abundance. Aluminum has also a low effect on the spectra. Magnesium has important lines in the supersoft spectra, but these were



not found to be dominant, suggesting an upper limit on magnesium abundance at 50 times solar. Silicon lines could not have been identified in the spectra suggesting a low abundance close to the solar value. Heavier elements were not detectable, but they were considered to be near solar values. It is important to note that the simple model atoms of these elements do not allow detailed modeling. Only some features of sulfur were identified in the spectra.

By fitting the interstellar absorption for PHOENIX models Petz et al. (2005) derived the hydrogen column density  $N_H = 4.0 \times 10^{21} \text{ cm}^{-2}$ . In this work it was found to be about a factor of ten lower,  $N_H = (4.8 \pm 0.3) \times 10^{20} \text{ cm}^{-2}$ , much closer to  $N_H = 3.47 \times 10^{20} \text{ cm}^{-2}$  found by Rauch et al. (2005) using TMAP.

From the model grid the possible temperature ( $T_{\text{eff}}$ ) range could have been limited to  $T_{\text{eff}} = 600,000 - 450,000 \text{ K}$ , at surface gravities ( $\log g = 8.2 \text{ cm/s}^2$ ) indicating a luminosity close to the Eddington limit at the beginning and later decreasing ( $\log g = 8.0 \text{ cm/s}^2$ ). The gravity did not change more than 0.2 dex between March 2003 and February 2004. The error in  $\log g$  is  $\pm 0.1$  dex and the estimated error in effective temperature is  $\pm 10,000 \text{ K}$  based on the resolution of the model grid. Considering the many free parameters affecting the final spectrum and their complex interactions these values might not be accurate.

Model fits for the Chandra data are shown in Figures 5.11 – 5.14. The parameters of model atmospheres are shown in Table 5.2 for the 4 Chandra observations of V4743 Sgr. The luminosity of the nova was close to the Eddington limit at the beginning and decreased significantly to the end of the supersoft phase. Figure 5.15 shows its

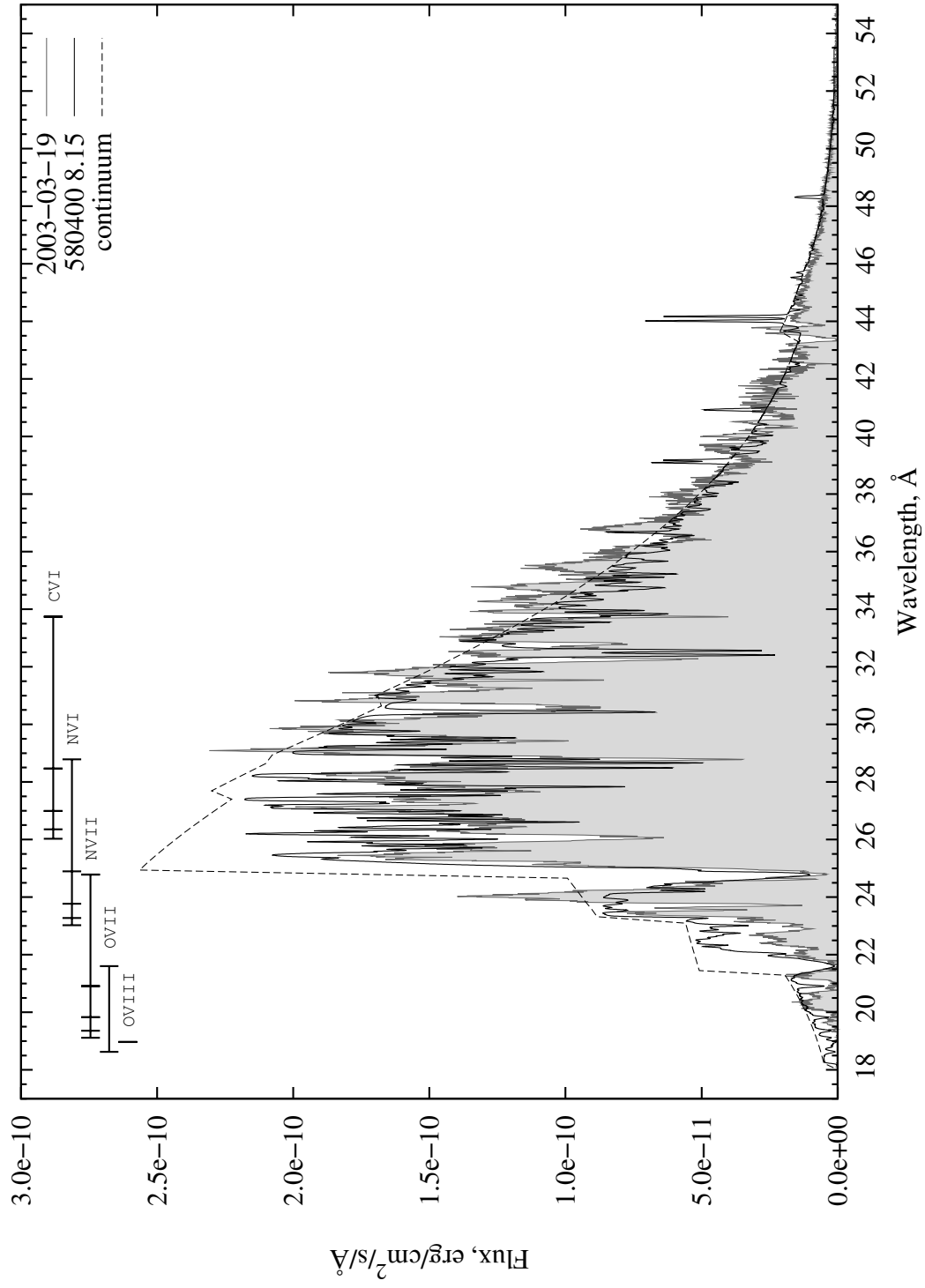


Figure 5.11: Model fit for V4743 Sgr. March 19, 2003

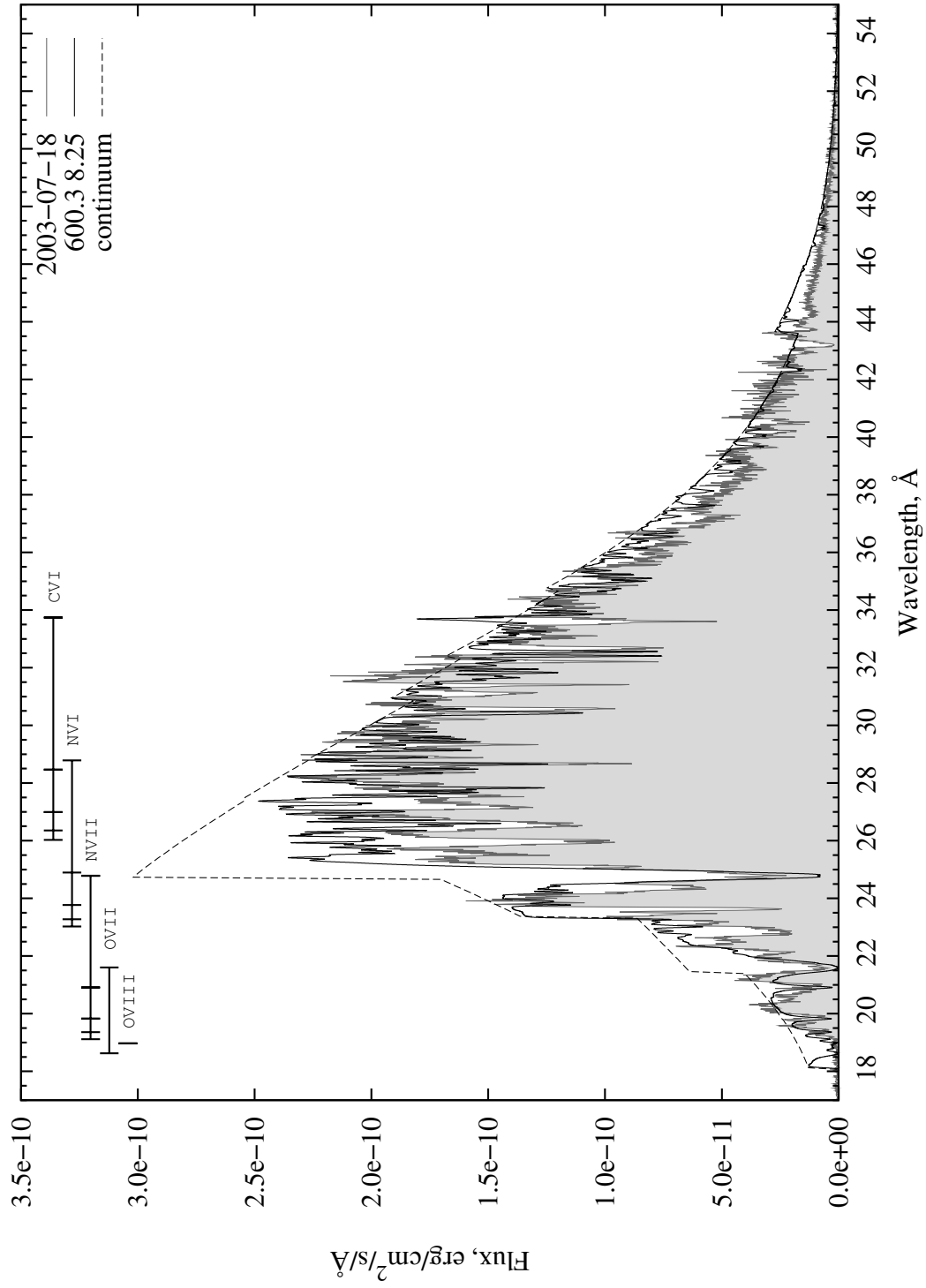


Figure 5.12: Model fit for V4743 Sgr. July 18, 2003.

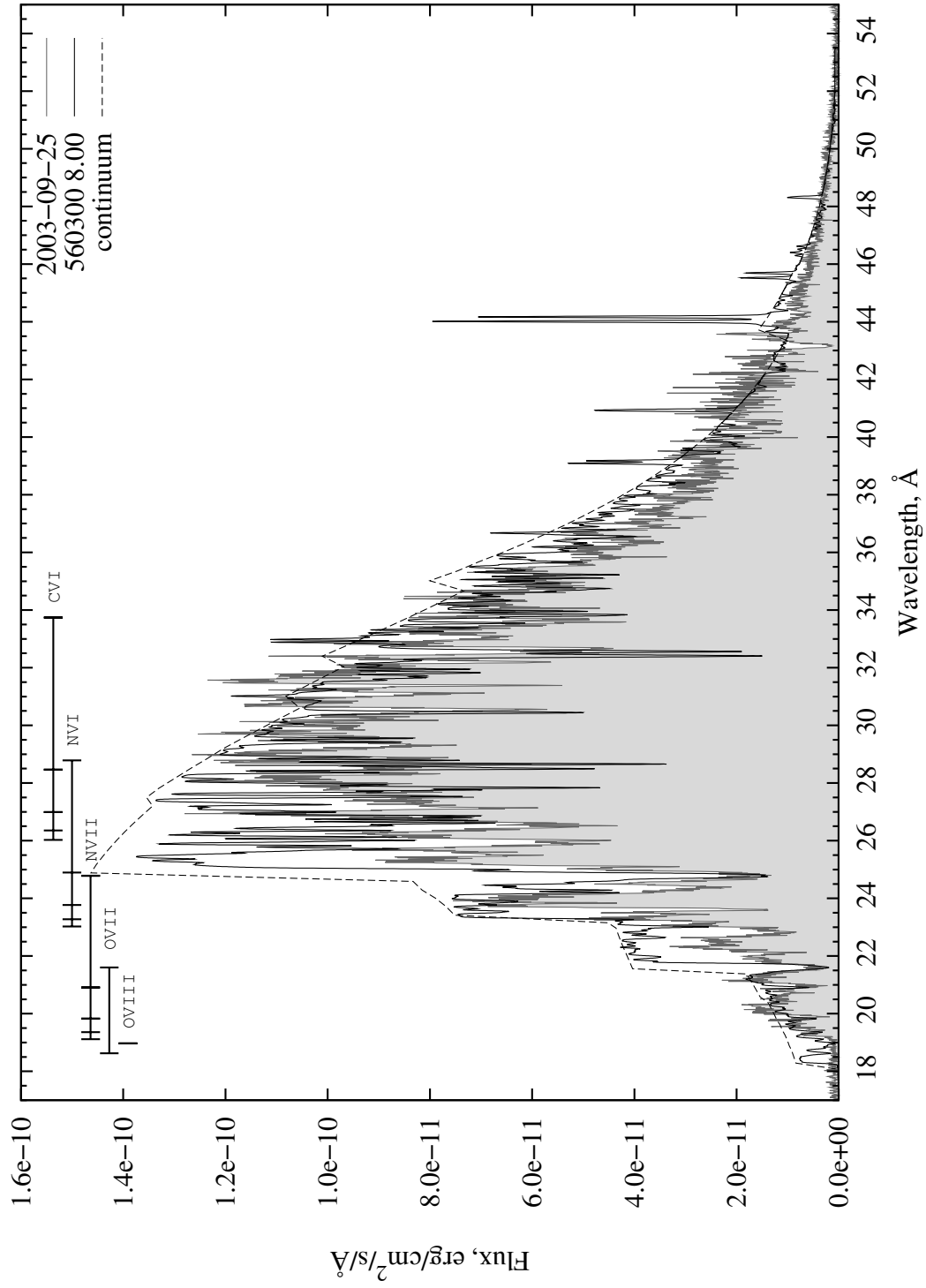


Figure 5.13: Model fit for V4743 Sgr. September 25, 2003

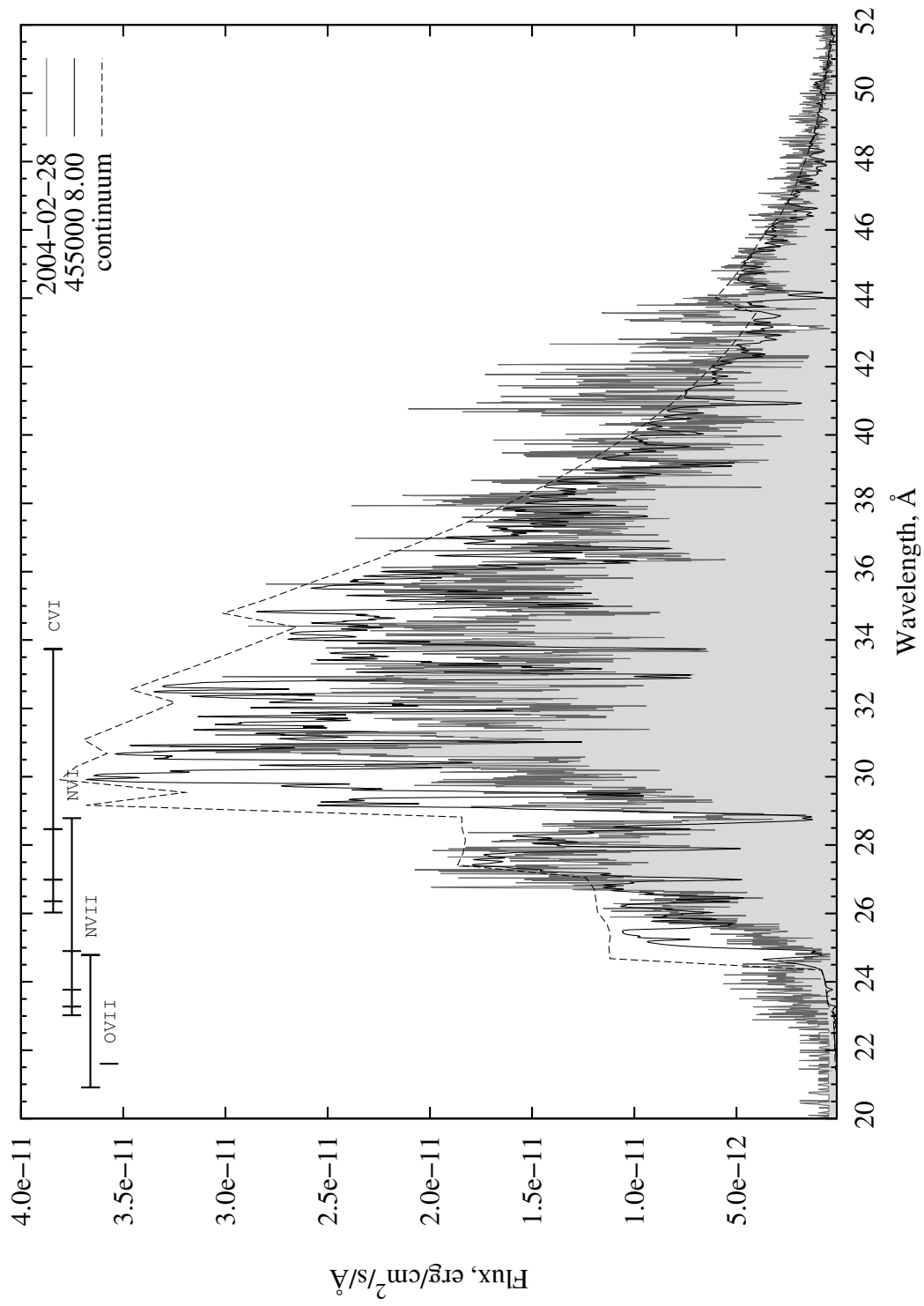


Figure 5.14: Model fit for V4743 Sgr. February 28, 2004

Table 5.2: Model parameters for V4743 Sgr.

Parameter	3775	3776	4435	5292
$T_{\text{eff}} [\times 1000 \text{ K}]$	580.4	600.0	560.3	455.0
$\log g [\text{cm/s}^2]$	8.15	8.20	8.00	8.00
$N_{\text{H}} [\times 10^{21} \text{ cm}^{-2}]$	0.46	0.51	0.51	0.51
$H_{\nu} [10^{17} \text{ erg/cm}^2/\text{s/Hz}]$	5.122	5.861	4.448	1.935
$d^2/R^2 [\times 10^{26}]$	1.5	1.2	1.2	1.2
He/He $_{\odot}$	7.5	5.0	3.0	4.0
C /C $_{\odot}$	5.0	25.0	3.0	2.0
N /N $_{\odot}$	140.0	70.0	26.0	60.0
O /O $_{\odot}$	12.0	16.0	2.5	14.0
Ne/Ne $_{\odot}$	200.0	250	50.0	10.0
Mg/Mg $_{\odot}$	1.0	30	50.0	9.0
Al/Al $_{\odot}$	100.0	30	100.0	100.0
Si /Si $_{\odot}$	0.2	0.2	2.0	5.0
S /S $_{\odot}$	1.0	1.0	1.0	1.0
Ar /Ar $_{\odot}$	2.0	0.0	2.0	0.06
Ca/Ca $_{\odot}$	0.05	0.0	0.05	0.01
Fe /Fe $_{\odot}$	0.1	0.0	0.1	0.1
$\Delta\lambda/\lambda \text{ N VI}$	$7.6 \times 10^{-3}$	0.0	0.0	0.0
$\Delta\lambda/\lambda \text{ N VII}$	$6.1 \times 10^{-3}$	$4 \times 10^{-3}$	$3.2 \times 10^{-3}$	$4 \times 10^{-3}$
$\Delta\lambda/\lambda \text{ O VII}$	$6.9 \times 10^{-3}$	$3.2 \times 10^{-3}$	$3.2 \times 10^{-3}$	–
R /R $_{\odot}$	0.014	0.016	0.016	0.016
L /L $_{\odot}$	20300	29000	22100	9600
M /M $_{\odot}$	1.03	[1.44]	0.91	0.91

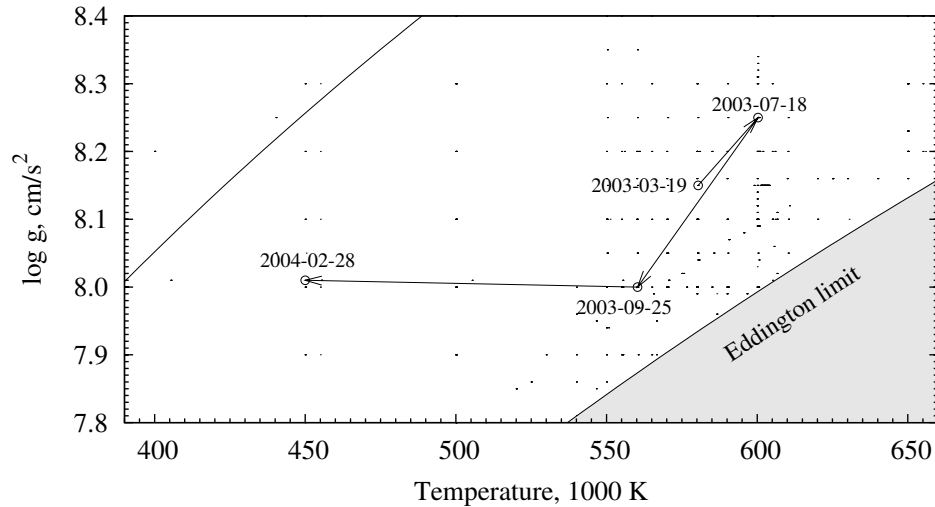


Figure 5.15: Spectral evolution of V4743 Sgr between March 2003 and February 2004.

evolution in the  $\log g - T_{\text{eff}}$  diagram. The models of the first three observations fall on a line near the Eddington luminosity and this indicates evolution at nearly constant luminosity. The spectral evolution is primarily due to the change of effective temperature, abundance evolution has lower order effects. The February 2004 spectrum shows a significant decrease in energy production. Assuming that the mass of the nova was constant the change of surface gravity indicate only a few percent variation of the radius.

The stellar radius derived from model fits is  $R = 0.015 R_{\odot}$ , or 10500 km. Adopting a WD mass of  $1 M_{\odot}$ , which has a core radius of about 6000 km, the extension of the atmosphere is around 75%. This result is somewhat lower, but it is still in agreement

with earlier studies.

### 5.6.2 V2491 Cyg

The classical nova V2491 Cyg was discovered on April 10, 2008 at visual magnitude  $V=7.7$ , (Nakano et al., 2008). The outburst occurred only six months after installation of the Ortega telescope at Florida Institute of Technology. Optical spectra were taken near optical maximum, these data are shown in Figure 1.5. The nova reached its optical maximum at  $V=7.54^m$  on Apr 11th. Using the reddening  $E(B - V) = 0.43$  (Rudy et al., 2008) the distance to the nova was estimated by Helton and Woodward (2008) to be  $d = 10.5$  kpc. V2491 Cyg was a very fast nova with  $t_2=5.65$  days. The broad spectral lines of He and N shown in Figure 1.5 indicated extreme expansion velocities. The  $H_\alpha$  FWHM was  $161.2 \text{ \AA}$ , implying an expansion velocity over 3600 km/s on May 17th (Nemeth et al., in prep.).

Table 5.3: X-ray observations of V2491 Cyg.

Observation ID	Date	Exposure (s)	Instrument	Comment
0552270501	2008/05/20	39339	XMM RGS	X-on
0552270601	2008/05/30	29980	XMM RGS	X-on

V2491 Cyg was observed with XMM two times in May 2008 (Table 5.3), and already has shown strong supersoft radiation. The spectra (Figure 5.16) indicated a hot continuum with strong nitrogen and oxygen absorption lines and very strong interstellar absorption. The first spectrum showed a peak flux at  $6 \times 10^{-11} \text{ erg/cm}^2/\text{s}/\text{\AA}$ , or 0.08 c/sec. The blue-shifted spectral features suggest an expanding atmosphere



as to be expected. The measured expansion velocity of O VII absorption lines was  $v_{\text{exp}} = 3330 \pm 140$  km/s and for O VIII  $v_{\text{exp}} = 3810 \pm 300$  km/s. The expansion velocity based on N VII lines was  $v_{\text{exp}} = 3280 \pm 240$  km/s and  $v_{\text{exp}} = 3100 \pm 300$  km/s for N VI lines. Individual spectral features of heavier elements are very hard to distinguish. Some blends suggest much lower velocities for these elements. The strong N VI and NVII lines as well as the differences in Doppler-shifts suggest an extended line-forming region with different dominant ions and wind velocities. A similar trend was

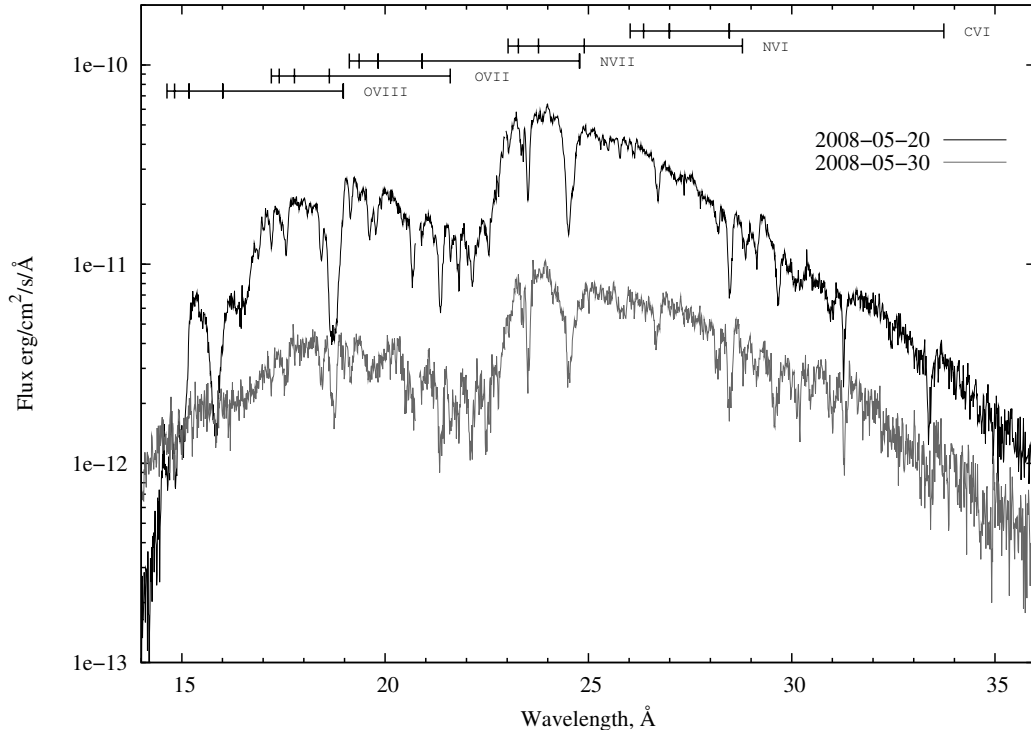


Figure 5.16: Spectral evolution of V2491 Cyg in May 2008. Both spectra were taken with XMM/RGS spectrometers.

found for oxygen lines in accordance with the results of Ness (2010). The line shifts indicate a strong wind and super Eddington luminosity. Such atmospheres cannot be

reliably modeled with TLUSTY 200. Figures 5.17 and 5.18 show the best-fit models using the parameters in Table 5.4. For comparison, a model with  $T_{\text{eff}} = 600,100$  K,  $\log g = 8.1$  cm/s<sup>2</sup> and solar abundances is shown in Figure 5.19. With solar composition there is more flux below 18 Å and the oxygen lines show similar strength like the data. The computed nitrogen lines are much weaker than observed and by increasing its abundance the high energy flux decreases rapidly, giving rise to strong ionization edges. However, a closer look reveals that the model is not terribly off compared to either the static WD or extended dynamical model presented in van Rossum and Ness (2010). The hydrogen column density was found to be  $N_{\text{H}} = (2.5 \pm 0.4) \times 10^{21}$  cm<sup>-2</sup> in the direction of V2491 Cyg. This is in good agreement with the column density  $N_{\text{H}} = 2.8 \times 10^{21}$  cm<sup>-2</sup> used by van Rossum and Ness (2010). However in this work interstellar absorption was calculated with Galactic abundances, while they used solar composition.

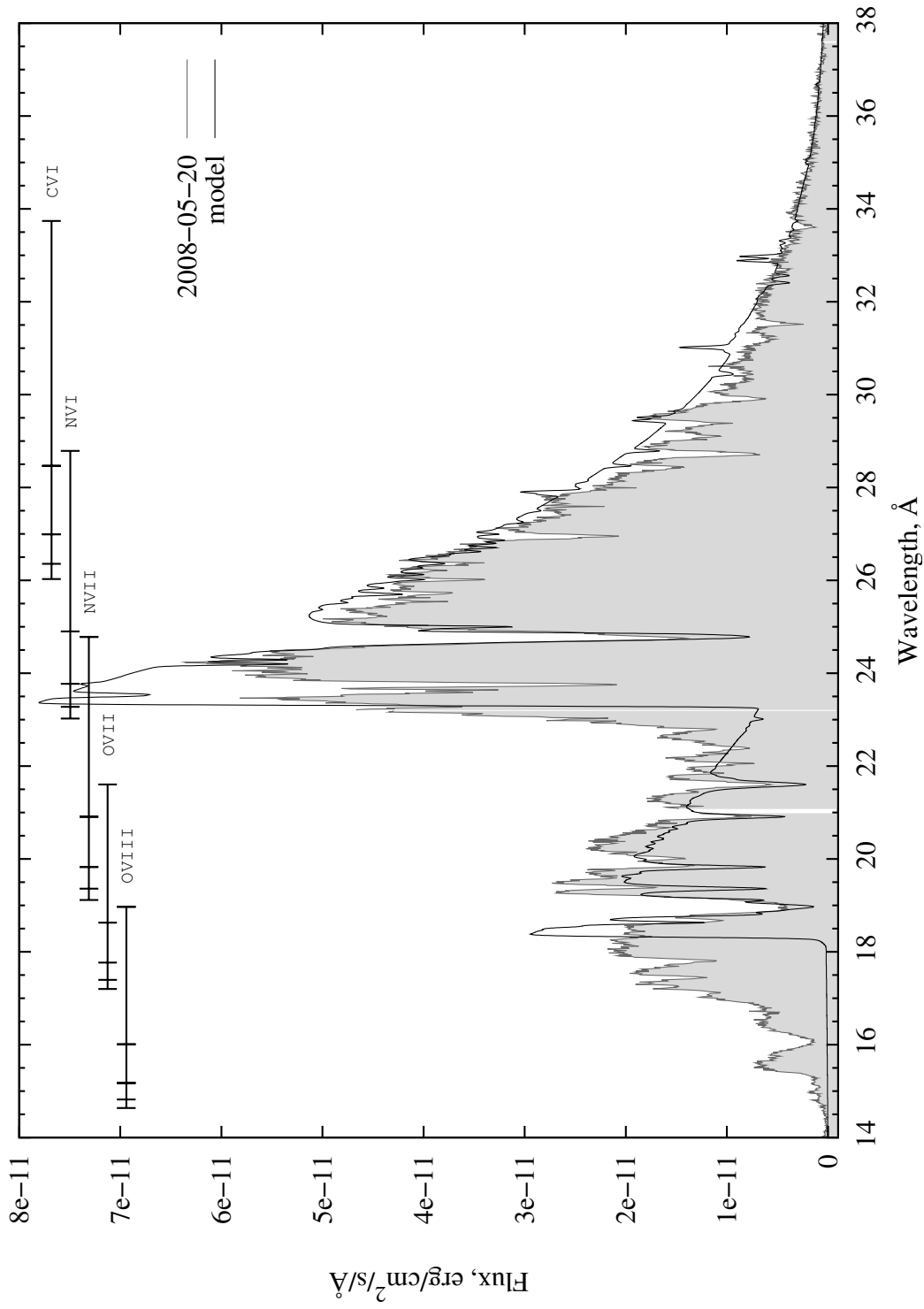


Figure 5.17: Best fit model for the May 20th spectrum. The strong discontinuity at 23 Å is due to interstellar absorption, the other at 18 Å is due to static, plane-parallel modeling.

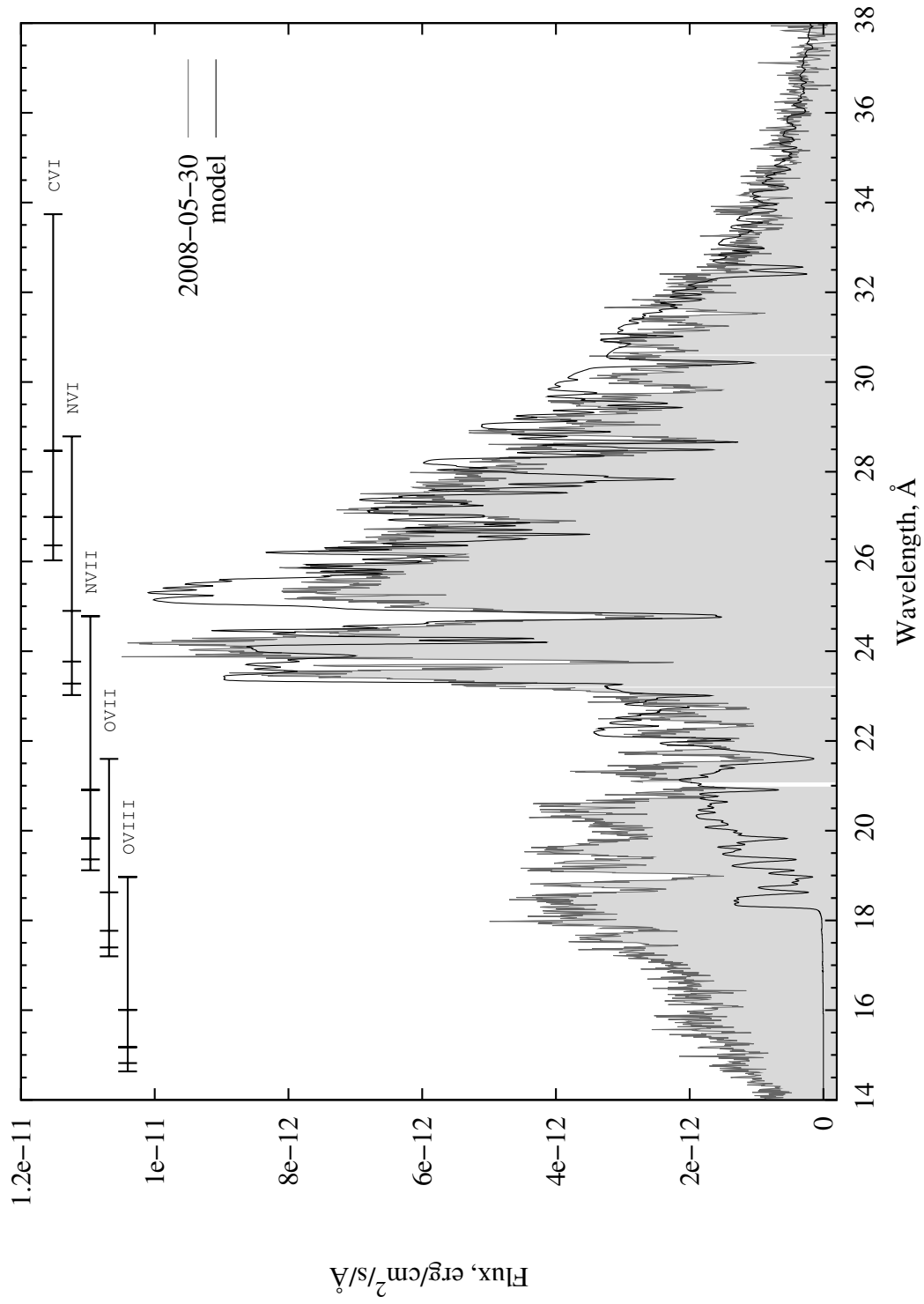


Figure 5.18: Best fit model for the May 30th spectrum.

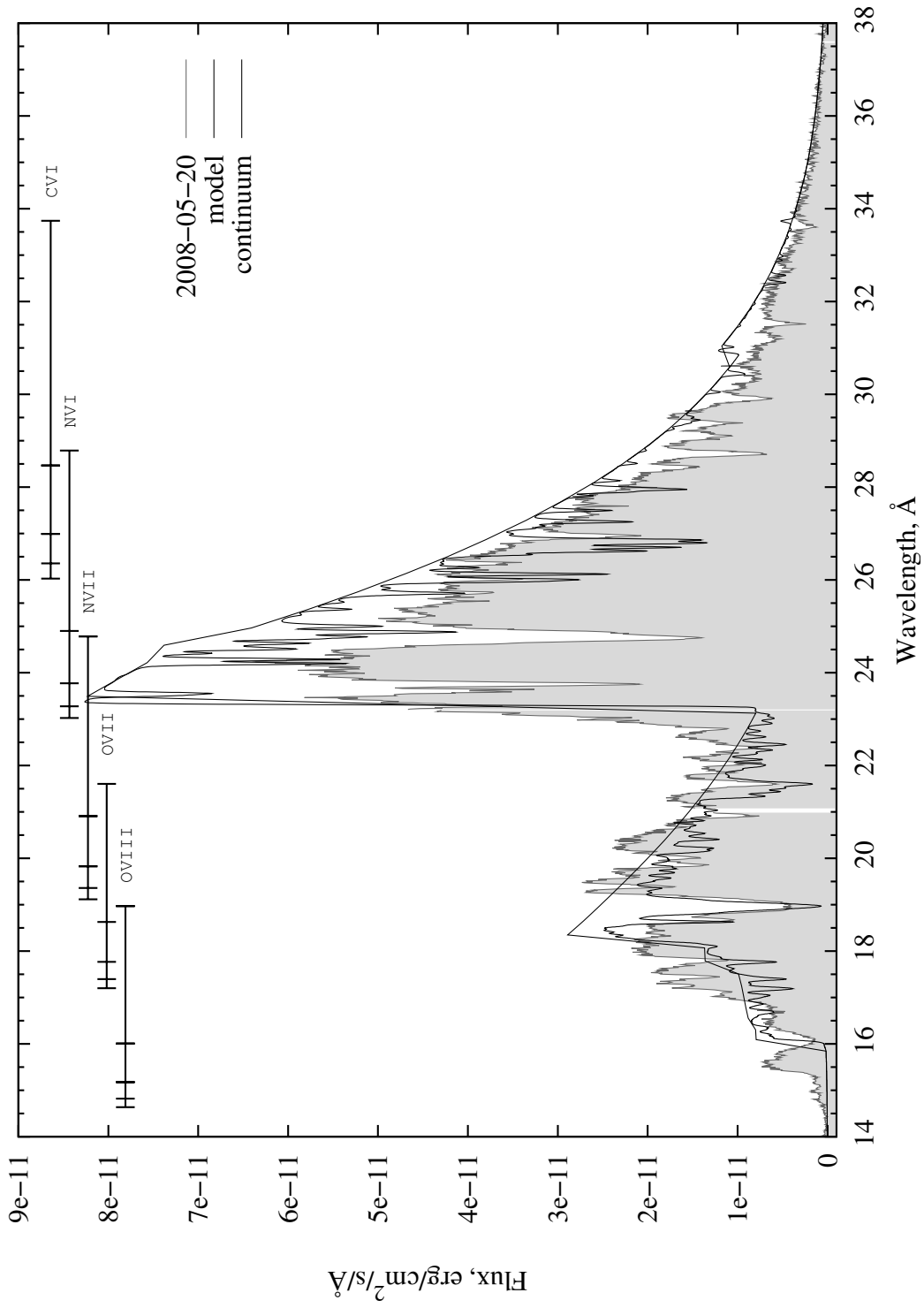


Figure 5.19: Model fit with solar abundances for the May 30th spectrum.

Table 5.4: Model parameters for V2491 Cyg.

Parameter	0552270501	0552270601	0552270501
$T_{\text{eff}} [\times 1000 \text{ K}]$	650.2	560.0	600.1
$\log g [\text{cm/s}^2]$	8.2	8.2	8.1
$N_{\text{H}} [\times 10^{21} \text{ cm}^{-2}]$	2.5	2.5	2.5
$H_{\nu} [10^{17} \text{ erg/cm}^2/\text{s/Hz}]$	8.064	4.444	5.852
$d^2/R^2 [\times 10^{26}]$	2.5	7.5	2.5
He/He $_{\odot}$	4.0	10.0	1.0
C/C $_{\odot}$	1.0	2.0	1.0
N/N $_{\odot}$	100.0	1000.0	1.0
O/O $_{\odot}$	2.0	80.0	1.0
Ne/Ne $_{\odot}$	50.0	50.0	1.0
Mg/Mg $_{\odot}$	50.0	50.0	1.0
Al/Al $_{\odot}$	100.0	1000.0	1.0
Si/Si $_{\odot}$	10.0	2.0	1.0
S/S $_{\odot}$	0.1	2.0	1.0
Ar/Ar $_{\odot}$	0.1	10.0	1.0
Ca/Ca $_{\odot}$	0.01	0.05	1.0
Fe/Fe $_{\odot}$	0.1	0.1	0.0
$\Delta\lambda/\lambda \text{ C VI}$	$1.05 \times 10^{-2}$	–	
$\Delta\lambda/\lambda \text{ N VI}$	$1.04 \times 10^{-2}$	–	
$\Delta\lambda/\lambda \text{ N VII}$	$1.01 \times 10^{-2}$	$9.68 \times 10^{-3}$	
$\Delta\lambda/\lambda \text{ O VII}$	$1.07 \times 10^{-2}$	$1.07 \times 10^{-2}$	
$\Delta\lambda/\lambda \text{ O VIII}$	$1.26 \times 10^{-2}$	$1.05 \times 10^{-2}$	

## Chapter 6

# Conclusions

Starting out from simple continuum models of light metals including only their ground states (black line in Figure 6.1) I built multi-level model atoms from NIST/ASD and TOPbase atomic data. I collected atomic data on radiative transition strengths and natural broadening for about 70,000 spectral lines in the supersoft range from low ionization degrees of C, N, O, Ne, Mg, Al, Si, S, Ar, Ca and Fe, up to hydrogenic ions. Altogether 21,148 energy levels and 542,914 transitions were included. On bound-free cross sections, data were extracted from TOPbase for all multiplets. With these opacity sources it is now possible to calculate full non-LTE line blanketed spectra in the supersoft range (the grey line shows in Figure 6.1) with TLUSTY and SYNSPEC. SYNSPEC also required slight modifications to increase the highest ionization degrees to match the new input files.

With an extensive grid I showed the effects of surface temperature, gravity, abundance and the influence of model atoms on the final spectrum. These relationships

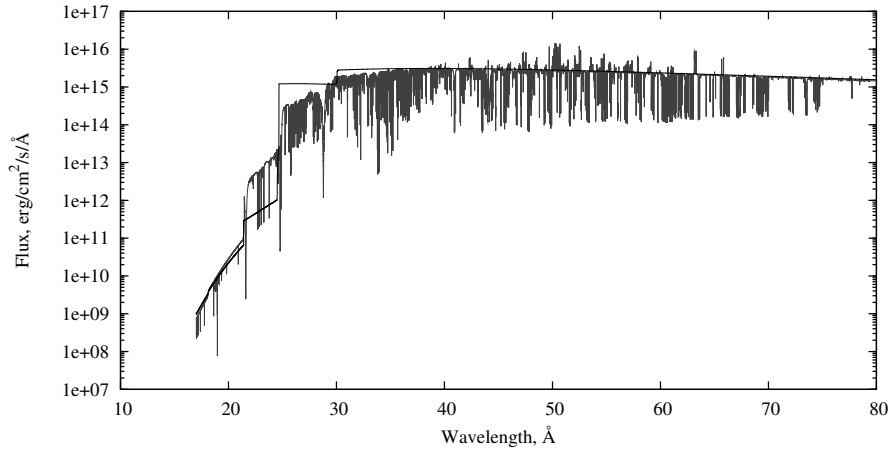


Figure 6.1: Comparison of a non-LTE CNO continuum spectrum (black line) and a full non-LTE spectrum (grey line) including H, He, C, N, O, Ne, Mg, Al and Si with detailed model atoms. Energy levels of S, Ar and Ca were averaged into 9–10 superlevels, Fe was included only with its ground states.

suggest that static plane-parallel models over-estimate the effective temperature and surface gravity for classical novae.

My work also required numerous little programs to effectively manipulate TLUSTY and SYNSPEC input and output files for spectral modeling. For example, model atoms have complex structures and any change in the level structure must be propagated through the entire model atom. By deleting one level, all higher level indices will change. Bound-free transition of the given level must be removed and all transitions originating from or ending on the given level must be removed. Such tasks can be done easily by hand for a few levels, but certainly not for hundreds of levels. Level averaging requires similar automated methods as well. TLUSTY stores



the atmospheric structure and level populations in its own format. These data blocks must be processed for graphing or to calculate ionization balance and conditions in the atmosphere. Short Python scripts create Grotrian diagrams from model atoms, convergence logs during model calculation, carrying out Gaussian convolution of the spectra or calculating interstellar absorption.

With TOPAtom one can build arbitrarily complex model atoms directly from the original TOPbase or NIST data files. Any other atomic data sets can be easily incorporated by reformatting them to the original format of one of these primary atomic data tables. Model atoms with superlevels and superlines (OS mode) are also available.

As part of this work a task-oriented pipeline (TGRID) was developed. TGRID can do spectral analysis from grid calculations up to abundance analysis. However, inaccuracies in the input atomic data, coupled with strong blanketing and the enormous interstellar reddening, made quantitative fits impossible. Steps of the spectral analysis are in modular format, which makes them scriptable and they can also be used independently in other applications.

Application of these techniques to some classical novae have shown the validity of the model atoms. I showed in the example of V4743 Sgr and V2491 Cyg how the new model atoms fit observed data of Chandra and XMM-Newton satellites. V4743 Sgr was very close to the Eddington limit in March – September 2003. The blue-shifted nitrogen and oxygen spectral lines confirm this. By February 2004 the luminosity decreased significantly and spectral lines appeared at their laboratory wavelengths,

which suggests that hydrogen burning was turned off, the stellar wind stopped and the WD returned to a static state. Abundance analysis showed enhancement of helium, nitrogen and oxygen compared to solar values. The abundance of nitrogen is about 10–20 times greater than was found by Petz et al. (2005). Oxygen is over-abundant by a factor of a few, while carbon is around solar values. Enhancement of neon, magnesium and aluminum of about 50 times the solar values were found. A slight over-abundance of silicon and sulfur is possible (up to twice the solar value). Argon and calcium are depleted compared to solar abundance. However, the abundance analysis is still uncertain and these figures should be considered only as approximations. These tests also showed the need for a comprehensive upgrade of TLUSTY/SYNSPEC to model CNe. The case of V2491 Cyg was a good example showing the limitation of static, plane-parallel modeling of luminous supersoft sources. The blue-shifted lines and the extended blue continuum indicate a strong wind. The simultaneous strong lines of NVI and NVII suggest an extended line-forming region and these features together cannot be modeled by static atmospheres. These objects need hydrodynamic calculations in spherical geometry, treating both the extended line formation region and stellar wind explicitly. This was beyond the scope of the current project. However, the technique used here work well for supersoft sources below the Eddington limit. Finally, for qualitative analysis on abundance and evolution of classical novae, many more spectroscopic observations are required.

## 6.1 Future directions

My work pointed out the need of Opacity Sampling for all metals heavier than Si. Their intermediate and high energy levels provide a lot of important lines in the X-ray region and contribute to bound-free transitions, which affects both the atmospheric structure as well as the final spectra. However, the increased computational cost introduced by many new frequency points (about 250,000 total) exceeds the capabilities of a single computer. For detailed analysis, a large number of models must be generated, and so it is preferable to use a computer grid.

Line broadening data can be updated with data for Stark broadening from STARK-B<sup>1</sup> maintained by M.S. Dimitrijević and S. Sahal-Bréchet. This extension requires further updates in SYNSPEC, which currently accepts broadening parameters as given in Griem (1974) for temperatures ranging up to 50,000 K.

The example of V2491 Cyg emphasized the importance of spherical geometry. Novae in their supersoft stage are luminous, usually well over the Eddington limit. Their modeling must be done in spherical geometry, and line formation considered in an extended and expanding non-LTE atmosphere. The most important update would be to reformulate TLUSTY for spherical geometry and incorporate stellar wind and hydrodynamics with a  $\beta$ -type velocity profile:

$$v = v_{\infty} \left(1 - \frac{R_0}{R}\right)^{\beta} \quad (6.1)$$

---

<sup>1</sup><http://stark-b.obspm.fr/index.php>

where,  $v_\infty$  is the terminal velocity of the stellar wind,  $R$  is the radial distance from the stellar surface and  $R_0$  is the radius of the star. The empirical exponent  $\beta$  defines the velocity profile in the wind.

It is also important to update and incorporate new and more reliable atomic data in the model atoms and the line list as they become available. For higher energy levels a further extension can be done using calculated data from The Atomic Line List<sup>2</sup> V2.05B12 by van Hoof. This work could be done with TOPAtom. Helium-like and lithium-like ions of metals are important in modeling and their energy levels and transitions are not calculated in TOPbase over azimuthal quantum number  $l > 4$ . These missing levels and transitions can be calculated with Cowan's Atomic Structure Code<sup>3</sup>. It is also important to update collision strengths for bound-free and bound-bound transitions. Although data are limited to the lowest levels up to  $N \leq 5$ , Chianti (Dere et al., 2009) provides spline fits for electron collision strengths for a wide range of temperatures and species.

At the current level of modeling and atomic databases all these updates are considered secondary compared to geometrical and dynamical considerations.

---

<sup>2</sup><http://www.pa.uky.edu/~peter/newpage/>

<sup>3</sup><http://tcd.ie/Physics/People/Cormac.McGuinness/Cowan/>

# Bibliography

Andreä, J., Drechsel, H., Starrfield, S., 1994. *Astronomy and Astrophysics* 291, 869.

Bałucińska-Church, M., McCammon, D., 1992. *Astrophysical Journal* 400, 699.

Bautista, M. A., Romano, P., Pradhan, A. K., 1998. *Astrophysical Journal Supplement Series* 118, 259.

Binney, J., Merrifield, M., 1998. *Galactic Astronomy*. Princeton University Press.

Burke, P. G., Seaton, M. J., 1971. *Methods in Computational Physics* 10, 1.

Cassatella, A., Lamers, H., Rossi, C., 2004. *Astronomy and Astrophysics* 420, 571.

Chandrasekhar, S., 1935. *Monthly Notices of the Royal Astronomical Society* 95, 207.

Clayton, D., 1968. *Principles of Stellar Evolution and Nucleosynthesis*. McGraw-Hill Book Company.

Cunto, W., Mendoza, C., Ochsenbein, F., Zeippen, C., 1993. *Astronomy and Astrophysics* 275, L5.

Dahlem, M., January 1999. *XMM User's Handbook*. 1st Edition.

- Della Valle, M., Livio, M., 1995. *Astrophysical Journal* 452, 704.
- Dere, K. P., Landi, E., Mason, H. E., Monsignori Fossi, B. C., Yound, P. R., 1997. *Astronomy and Astrophysics Supplement Series* 125, 149.
- Dere, K. P., Landi, E., Young, P. R., Del Zanna, G., Landini, M., Mason, H. E., 2009. *Astronomy and Astrophysics* 498, 915.
- Gehrz, R., Truran, J. W., Williams, R. E., Starrfield, S., 1998. *Publications of the Astronomical Society of the Pacific* 110, 3.
- Gilmozzi, R., Della Valle, M., 2003. *Lecture Notes in Physics: Stellar Candles for the Extragalactic Distance Scale*. Springer, Ch. 12.
- Greiner, J., 2000. *New Astronomy* 5, 137.
- Grevesse, N., Sauval, A. J., 1998. *Space Science Reviews* 85, 161.
- Griem, H., 1974. *Spectral Line Broadening by Plasmas*. Academic Press, New York.
- Hartmann, H. W., Heise, J., 1997. *Astronomy and Astrophysics* 322, 591.
- Haseda, K., West, D., Yamaoka, H., Masi, G., 2002. *International Astronomical Union Circulars* 7975.
- Helton, L. A., Woodward, C. E., 2008. *The Astronomer's Telegram* 1379.
- Hubeny, I., 1988. *Computer Physics Comm.* 52, 103.
- Hubeny, I., Lanz, T., 1992. *Astronomy and Astrophysics* 262, 501.

- Hubeny, I., Lanz, T., 1995. *Astrophysical Journal* 439, 875.
- Hubeny, I., Lanz, T., April 2000. *SYNSPEC - A User's Guide*, Version 43.
- Hubeny, I., Lanz, T., February 2003. *TLUSTY - A User's Guide*, Version 200.
- Kantorovich, L. V., 1949. *Trudy Mat. Inst. Steklov.* , 104.
- Kato, M., 2010. *Astronomische Nachrichten* 331, 140.
- Kohn, W., 1996. *Physical Review Letters* 76, 3168.
- Kolb, U., Politano, M., 1997. *Astronomy and Astrophysics* 319, 909.
- Kunasz, P. B., Olson, G. L., 1988 39, 1.
- Lada, C., 2006. *Astrophysical Journal* 640, L63.
- Lanz, T., Hubeny, I., 2003. *Astrophysical Journal Supplement Series* 146, 417.
- Lanz, T., Hubeny, I., 2007. *Astrophysical Journal Supplement Series* 169, 83.
- Lanz, T., Telis, G. A., Audard, M., Paerels, F., P., R. A., Hubeny, I., 2005. *Astrophysical Journal* 619, 517.
- Leibowitz, E., Orio, M., Gonzalez-Riestra, R., Lipkin, Y., Ness, J.-U., Starrfield, S., Still, M., Tepedelenlioglu, E., 2006. *Monthly Notices of the Royal Astronomical Society* 371, 424.
- Livio, M., 1992. *Astrophysical Journal* 393, 516.
- Lundmark, K., 1921. *Publications of the Astronomical Society of the Pacific* 33, 255.

- Lyke, J. E., Kelly, M. S., Gehrz, R. D., Woodward, C. E., 2002. *Bulletin of the American Astronomical Society* 34, 1161.
- MacDonald, J., Fujimoto, M., Truran, J., 1985. *Astrophysical Journal* 294, 263.
- MacDonald, J., Vennes, S., 1991. *Astrophysical Journal* 373, L51.
- McLaughlin, D. B., 1943. *Publications of the Observatory of the University of Michigan* 8, 149.
- McLaughlin, D. B., 1945. *Publications of the Astronomical Society of the Pacific* 57, 69.
- Mihalas, D., 1970. *Stellar Atmospheres*. W. H. Freeman and Company.
- Mihalas, D., 1978. *Stellar Atmospheres*. W. H. Freeman and Company.
- Morrison, R., McCammon, D., 1983. *Astrophysical Journal* 270, 119.
- Nakano, S., Beize, J., Jin, Z.-W., Gao, X., Yamaoka, H., Haseda, K., Guido, E., Sostero, G., Klingenberg, G., Kadoka, K., 2008. *International Astronomical Union Circulars* 8934.
- Ness, J.-U., 2010. *Astronomische Nachrichten* 331, 179.
- Ng, K. C., 1974. *Journal of Quantitative Spectroscopy and Radiative Transfer* 61, 2680.
- Nielbock, M., Schmidtobreick, L., 1997. *Astronomy and Astrophysics Supplement Series* 125, 149.



- Ninković, S., Trajkovska, V., 2006. *Serb. Astron. J.* 172, 17.
- Ögelman, H., Beuermann, K., Krautter, J., 1984. *Astrophysical Journal* 287, L31.
- Orio, M., Covington, J., Ögelman, 2001. *Astronomy and Astrophysics* 373, 542.
- Petz, A., 2005. Modeling atmospheres of classical novae in x-rays with phoenix. Ph.D. thesis, University of Hamburg.
- Petz, A., Hauschildt, P. H., Ness, J.-U., Starrfield, S., 2005. *Astronomy and Astrophysics* 431, 321.
- Rauch, T., Orio, M., Gonzales-Riestra, R., Still, M., A. A. G.-R. R., 2005 334, 423R.
- Rudy, R. J., Lynch, D. K., Russell, R. W., 2008. *International Astronomical Union Circulars* 8938.
- Rybicki, G. B., Hummer, D. G., 1991. *Astronomy and Astrophysics* 245, 171.
- Seaton, M., 1985. *Journal of Physics B* 18, 2111.
- Seaton, M., 1987. *Journal of Physics* 20, 6363.
- Shafter, A. W., 2002. *AIP Conference Proceedings* 637, 462.
- van Rossum, D., Ness, J.-U., 2010. *Astronomische Nachrichten* 331, 175.
- Vanlandingham, K. M., Schwarz, G., Starrfield, S., Woodward, C., Wagner, M., Ness, J.-U., Helton, A., 2007. *Bulletin of the American Astronomical Society* 38, 99.
- Vennes, S., 1999. *Astrophysical Journal* 525, 995.

Verner, D. A., Ferland, G. J., Korista, K. T., Yakovlev, D. G., 1996. *Astrophysical Journal Supplement Series* 103, 467.

Williams, R. E., 1992. *Astronomical Journal* 104, 725.

# Appendix A

## O VI model atom

The detailed output for O VI has more than 1600 rows, the averaged model atom file still has 340 rows, what cannot be presented here. Instead of the whole model atom, I show only the first ten levels, their bound-free cross sections and transitions. The line list consists of 471 transitions total; out of those I show are shown the first 64 lines, up to 200 Å. Although O VI is a low ionization stage to be significantly populated in the hot atmospheres of CNe, I generated this model atom to validate the procedure. This model atom file can be found in good agreement with the O VI data file built by Lanz and Hubeny (2003), at TLUSTY's web page:

<http://nova.astro.umd.edu/Tlusty2002/database/atom/o6.dat>

# Simplified output of TOPAtom

```

***** Levels
3.339711965517e+16      2.      2      '____1s2.2s'      0      0.      0      ! 1 2Se 0.000000
3.050786984119e+16      2.      2      '____1s2.2p'      0      0.      0      ! 2 2Po 96.375000
3.049190589280e+16      4.      2      '____1s2.2p'      0      0.      0      ! 3 2Po 96.907500
1.420920916918e+16      2.      3      '____1s2.3s'      0      0.      -103     ! 4 2Se 640.039800
1.342441846848e+16      6.      3      '____21lev____'      0      0.      -103     ! 5 2Po 666.217600
1.317143080819e+16     10.     3      '____21lev____'      0      0.      -103     ! 6 2De 674.656360
7.833936678490e+15      2.      4      '____1s2.4s'      0      0.      -104     ! 7 2Se 852.696000
7.513746341647e+15      6.      4      '____21lev____'      0      0.      -104     ! 8 2Po 863.376400
7.408323124622e+15     10.     4      '____21lev____'      0      0.      -104     ! 9 2De 866.892940
7.402624840890e+15     14.     4      '____21lev____'      0      0.      -104     ! 10 2Fo 867.083014

***** Continuum transitions
1 11      1 174 0 0 0 9.2359e-20 0.000e+00
0.019 0.039 0.059 0.078 0.097 0.116 0.135 0.153 0.171 0.190 0.208 0.226 0.279
0.372 0.448 0.513 0.569 0.619 0.664 0.704 0.705 0.706 0.708 0.709 0.725 0.740
0.756 0.771 0.787 0.802 0.818 0.833 0.849 0.865 0.880 0.896 0.911 0.927 0.942
0.958 0.973 0.989 1.004 1.020 1.035 1.051 1.067 1.082 1.098 1.113 1.129 1.144
1.160 1.175 1.191 1.206 1.222 1.237 1.253 1.269 1.284 1.300 1.315 1.331 1.346
1.362 1.377 1.393 1.408 1.424 1.440 1.455 1.471 1.489
-0.512 -0.547 -0.583 -0.620 -0.656 -0.692 -0.728 -0.764 -0.799 -0.836 -0.873
-0.910 -1.032 -1.219 -1.380 -1.521 -1.647 -1.761 -1.865 -0.955 -0.819 -0.730
-0.676 -0.639 -0.599 -0.637 -0.676 -0.714 -0.753 -0.792 -0.832 -0.872 -0.912
-0.952 -0.992 -1.032 -1.073 -1.114 -1.155 -1.197 -1.238 -1.280 -1.322 -1.364
-1.406 -1.448 -1.491 -1.533 -1.576 -1.619 -1.663 -1.706 -1.750 -1.793 -1.837
-1.881 -1.925 -1.970 -2.014 -2.059 -2.103 -2.148 -2.193 -2.238 -2.284 -2.329
-2.375 -2.420 -2.466 -2.512 -2.558 -2.604 -2.649 -2.661

2 11      1 168 0 0 0 1.1173e-19 0.000e+00
0.012 0.025 0.037 0.050 0.062 0.075 0.087 0.100 0.112 0.124 0.137 0.149 0.161
0.174 0.186 0.198 0.210 0.222 0.234 0.246 0.258 0.270 0.282 0.294 0.306 0.318
0.330 0.341 0.353 0.365 0.376 0.388 0.400 0.411 0.423 0.434 0.439 0.455 0.471
0.488 0.504 0.520 0.536 0.552 0.568 0.584 0.600 0.616 0.631 0.647 0.663 0.678
0.694 0.709 0.725 0.740 0.756 0.771 0.786 0.801 0.816 0.831 0.846 0.861 0.876
0.891 0.906 0.923
-0.429 -0.467 -0.504 -0.542 -0.580 -0.616 -0.655 -0.692 -0.730 -0.767 -0.807
-0.844 -0.879 -0.917 -0.958 -0.995 -1.032 -1.070 -1.108 -1.146 -1.184 -1.222
-1.260 -1.298 -1.336 -1.374 -1.412 -1.451 -1.489 -1.527 -1.565 -1.604 -1.642
-1.680 -1.719 -1.757 -1.772 -1.826 -1.880 -1.935 -1.990 -2.044 -2.099 -2.154
-2.209 -2.264 -2.318 -2.373 -2.428 -2.483 -2.538 -2.593 -2.648 -2.703 -2.758
-2.813 -2.868 -2.923 -2.978 -3.033 -3.088 -3.143 -3.198 -3.254 -3.309 -3.364
-3.419 -3.442

3 11      1 168 0 0 0 1.1173e-19 0.000e+00
0.012 0.025 0.037 0.050 0.062 0.075 0.087 0.100 0.112 0.124 0.137 0.149 0.161
0.174 0.186 0.198 0.210 0.222 0.234 0.246 0.258 0.270 0.282 0.294 0.306 0.318
0.330 0.341 0.353 0.365 0.376 0.388 0.400 0.411 0.423 0.434 0.439 0.455 0.471
0.488 0.504 0.520 0.536 0.552 0.568 0.584 0.600 0.616 0.631 0.647 0.663 0.678
0.694 0.709 0.725 0.740 0.756 0.771 0.786 0.801 0.816 0.831 0.846 0.861 0.876
0.891 0.906 0.923
-0.429 -0.467 -0.504 -0.542 -0.580 -0.616 -0.655 -0.692 -0.730 -0.767 -0.807
-0.844 -0.879 -0.917 -0.958 -0.995 -1.032 -1.070 -1.108 -1.146 -1.184 -1.222
-1.260 -1.298 -1.336 -1.374 -1.412 -1.451 -1.489 -1.527 -1.565 -1.604 -1.642
-1.680 -1.719 -1.757 -1.772 -1.826 -1.880 -1.935 -1.990 -2.044 -2.099 -2.154
-2.209 -2.264 -2.318 -2.373 -2.428 -2.483 -2.538 -2.593 -2.648 -2.703 -2.758
-2.813 -2.868 -2.923 -2.978 -3.033 -3.088 -3.143 -3.198 -3.254 -3.309 -3.364
-3.419 -3.442

4 11      1 174 0 0 0 1.5288e-19 0.000e+00
0.019 0.038 0.057 0.076 0.095 0.114 0.132 0.151 0.169 0.188 0.206 0.224 0.242
0.260 0.278 0.296 0.314 0.332 0.349 0.367 0.384 0.402 0.419 0.436 0.454 0.471
0.488 0.505 0.522 0.539 0.555 0.572 0.589 0.605 0.622 0.638 0.655 0.671 0.688
0.704 0.720 0.736 0.752 0.768 0.784 0.800 0.807 0.830 0.853 0.875 0.898 0.920
0.943 0.965 0.987 1.009 1.031 1.052 1.074 1.096 1.117 1.138 1.160 1.181 1.202
1.223 1.244 1.265 1.285 1.306 1.327 1.347 1.368 1.385
-0.293 -0.328 -0.363 -0.399 -0.434 -0.470 -0.504 -0.540 -0.575 -0.611 -0.646
-0.682 -0.717 -0.752 -0.788 -0.824 -0.860 -0.896 -0.932 -0.966 -1.002 -1.037
-1.073 -1.109 -1.144 -1.180 -1.216 -1.252 -1.287 -1.323 -1.359 -1.396 -1.431
-1.467 -1.503 -1.539 -1.575 -1.611 -1.648 -1.684 -1.719 -1.754 -1.790 -1.827
-1.863 -1.900 -1.917 -1.968 -2.021 -2.073 -2.125 -2.178 -2.230 -2.282 -2.335
-2.387 -2.440 -2.493 -2.545 -2.598 -2.650 -2.703 -2.756 -2.809 -2.861 -2.914
-2.967 -3.020 -3.073 -3.126 -3.178 -3.231 -3.284 -3.300

5 11      1 173 0 0 0 2.0972e-19 0.000e+00
0.015 0.031 0.046 0.062 0.077 0.092 0.107 0.122 0.137 0.152 0.166 0.181 0.196
0.210 0.225 0.239 0.253 0.268 0.282 0.296 0.310 0.324 0.338 0.351 0.365 0.379
0.393 0.406 0.420 0.433 0.446 0.460 0.473 0.486 0.499 0.513 0.526 0.539 0.552
0.564 0.577 0.590 0.603 0.615 0.628 0.641 0.653 0.666 0.678 0.691 0.696 0.714
0.731 0.749 0.766 0.784 0.801 0.818 0.835 0.852 0.869 0.886 0.903 0.919 0.936
0.952 0.969 0.985 1.001 1.018 1.034 1.050 1.067
-0.155 -0.193 -0.230 -0.267 -0.304 -0.341 -0.379 -0.415 -0.452 -0.489 -0.527
-0.564 -0.602 -0.638 -0.675 -0.712 -0.749 -0.788 -0.824 -0.863 -0.900 -0.939
-0.975 -1.012 -1.049 -1.087 -1.125 -1.162 -1.200 -1.237 -1.275 -1.312 -1.350

```

-1.388 -1.426 -1.463 -1.500 -1.539 -1.577 -1.614 -1.652 -1.690 -1.728 -1.764  
-1.804 -1.841 -1.879 -1.917 -1.954 -1.992 -2.010 -2.064 -2.119 -2.173 -2.228  
-2.282 -2.337 -2.392 -2.446 -2.501 -2.556 -2.610 -2.665 -2.720 -2.775 -2.829  
-2.884 -2.939 -2.994 -3.049 -3.104 -3.158 -3.179  
6 11 1 177 0 0 0 1.3941e-19 0.000e+00  
0.011 0.022 0.033 0.044 0.055 0.066 0.077 0.088 0.099 0.110 0.121 0.132 0.142  
0.153 0.164 0.174 0.185 0.196 0.206 0.217 0.227 0.238 0.248 0.259 0.269 0.280  
0.290 0.300 0.311 0.321 0.331 0.341 0.351 0.362 0.372 0.382 0.392 0.402 0.412  
0.422 0.432 0.442 0.452 0.462 0.471 0.481 0.491 0.501 0.511 0.520 0.530 0.540  
0.549 0.559 0.569 0.578 0.588 0.597 0.607 0.616 0.626 0.635 0.644 0.654 0.663  
0.672 0.682 0.691 0.700 0.703 0.716 0.729 0.742 0.756 0.769 0.782 0.799  
-0.333 -0.371 -0.410 -0.448 -0.487 -0.525 -0.564 -0.602 -0.640 -0.679 -0.717  
-0.757 -0.795 -0.833 -0.872 -0.910 -0.950 -0.987 -1.026 -1.065 -1.103 -1.142  
-1.181 -1.219 -1.258 -1.296 -1.335 -1.374 -1.413 -1.452 -1.490 -1.529 -1.568  
-1.607 -1.646 -1.684 -1.723 -1.762 -1.801 -1.841 -1.879 -1.917 -1.955 -1.995  
-2.035 -2.073 -2.112 -2.151 -2.190 -2.230 -2.268 -2.307 -2.346 -2.385 -2.424  
-2.463 -2.503 -2.542 -2.581 -2.620 -2.659 -2.699 -2.737 -2.777 -2.815 -2.854  
-2.893 -2.932 -2.973 -2.984 -3.038 -3.094 -3.150 -3.206 -3.262 -3.317 -3.343  
7 11 1 179 0 0 0 2.2219e-19 0.000e+00  
0.018 0.037 0.055 0.074 0.092 0.111 0.129 0.147 0.165 0.184 0.202 0.220 0.238  
0.256 0.274 0.291 0.309 0.327 0.345 0.362 0.380 0.397 0.415 0.432 0.450 0.467  
0.484 0.502 0.519 0.536 0.553 0.570 0.587 0.604 0.621 0.638 0.655 0.672 0.689  
0.705 0.722 0.739 0.755 0.772 0.788 0.805 0.821 0.837 0.854 0.870 0.886 0.903  
0.919 0.935 0.951 0.967 0.983 0.999 1.015 1.031 1.034 1.057 1.080 1.103 1.126  
1.148 1.171 1.193 1.215 1.238 1.260 1.282 1.304 1.326 1.348 1.370 1.392 1.414  
1.431  
-0.130 -0.165 -0.201 -0.236 -0.271 -0.305 -0.341 -0.376 -0.411 -0.446 -0.481  
-0.516 -0.551 -0.587 -0.622 -0.657 -0.692 -0.728 -0.762 -0.798 -0.833 -0.869  
-0.903 -0.939 -0.975 -1.010 -1.045 -1.080 -1.116 -1.152 -1.187 -1.222 -1.258  
-1.293 -1.329 -1.364 -1.400 -1.436 -1.471 -1.507 -1.543 -1.578 -1.614 -1.650  
-1.686 -1.721 -1.757 -1.793 -1.829 -1.863 -1.899 -1.935 -1.971 -2.008 -2.044  
-2.080 -2.116 -2.152 -2.188 -2.224 -2.232 -2.283 -2.335 -2.386 -2.438 -2.490  
-2.542 -2.594 -2.646 -2.698 -2.750 -2.802 -2.855 -2.907 -2.959 -3.011 -3.063  
-3.115 -3.130  
8 11 1 177 0 0 0 3.1248e-19 0.000e+00  
0.016 0.033 0.049 0.065 0.082 0.098 0.114 0.130 0.146 0.162 0.177 0.193 0.209  
0.224 0.240 0.255 0.271 0.286 0.301 0.316 0.332 0.347 0.362 0.376 0.391 0.406  
0.421 0.435 0.450 0.465 0.479 0.493 0.508 0.522 0.536 0.550 0.565 0.579 0.593  
0.606 0.620 0.634 0.648 0.662 0.675 0.689 0.702 0.716 0.729 0.742 0.756 0.769  
0.782 0.795 0.808 0.821 0.834 0.847 0.860 0.873 0.886 0.898 0.908 0.926 0.944  
0.962 0.980 0.998 1.016 1.034 1.051 1.069 1.086 1.104 1.121 1.138 1.155  
0.018 -0.018 -0.054 -0.090 -0.127 -0.163 -0.199 -0.236 -0.272 -0.309 -0.346  
-0.382 -0.418 -0.455 -0.492 -0.529 -0.565 -0.602 -0.638 -0.676 -0.712 -0.749  
-0.785 -0.824 -0.860 -0.896 -0.932 -0.970 -1.008 -1.045 -1.082 -1.119 -1.156  
-1.194 -1.231 -1.268 -1.305 -1.343 -1.380 -1.418 -1.455 -1.492 -1.530 -1.567  
-1.604 -1.642 -1.680 -1.717 -1.754 -1.793 -1.830 -1.866 -1.906 -1.943 -1.979  
-2.018 -2.056 -2.093 -2.131 -2.169 -2.207 -2.245 -2.274 -2.326 -2.380 -2.434  
-2.488 -2.542 -2.597 -2.651 -2.705 -2.760 -2.814 -2.868 -2.923 -2.977 -2.995  
9 11 1 182 0 0 0 2.7680e-19 0.000e+00  
0.013 0.027 0.040 0.054 0.067 0.080 0.093 0.106 0.119 0.132 0.145 0.158 0.170  
0.183 0.195 0.208 0.220 0.233 0.245 0.257 0.270 0.282 0.294 0.306 0.318 0.330  
0.341 0.353 0.365 0.377 0.388 0.400 0.411 0.423 0.434 0.446 0.457 0.468 0.480  
0.491 0.502 0.513 0.524 0.535 0.546 0.557 0.568 0.579 0.590 0.600 0.611 0.622  
0.633 0.643 0.654 0.664 0.675 0.685 0.696 0.706 0.716 0.727 0.737 0.747 0.757  
0.767 0.777 0.788 0.798 0.808 0.818 0.828 0.837 0.847 0.857 0.867 0.877 0.887  
0.896 0.906 0.913 0.930  
-0.035 -0.073 -0.111 -0.149 -0.187 -0.225 -0.263 -0.301 -0.339 -0.378 -0.415  
-0.453 -0.492 -0.530 -0.567 -0.605 -0.644 -0.682 -0.721 -0.759 -0.796 -0.835  
-0.873 -0.910 -0.950 -0.987 -1.027 -1.065 -1.104 -1.142 -1.181 -1.219 -1.257  
-1.296 -1.334 -1.373 -1.412 -1.450 -1.489 -1.527 -1.565 -1.605 -1.644 -1.682  
-1.721 -1.759 -1.798 -1.836 -1.876 -1.914 -1.954 -1.991 -2.030 -2.069 -2.108  
-2.147 -2.186 -2.224 -2.263 -2.302 -2.341 -2.380 -2.419 -2.458 -2.497 -2.536  
-2.575 -2.614 -2.653 -2.692 -2.730 -2.769 -2.809 -2.847 -2.886 -2.928 -2.966  
-3.004 -3.044 -3.083 -3.113 -3.135  
10 11 1 182 0 0 0 2.7680e-19 0.000e+00  
0.013 0.027 0.040 0.054 0.067 0.080 0.093 0.106 0.119 0.132 0.145 0.158 0.170  
0.183 0.195 0.208 0.220 0.233 0.245 0.257 0.270 0.282 0.294 0.306 0.318 0.330  
0.341 0.353 0.365 0.377 0.388 0.400 0.411 0.423 0.434 0.446 0.457 0.468 0.480  
0.491 0.502 0.513 0.524 0.535 0.546 0.557 0.568 0.579 0.590 0.600 0.611 0.622  
0.633 0.643 0.654 0.664 0.675 0.685 0.696 0.706 0.716 0.727 0.737 0.747 0.757  
0.767 0.777 0.788 0.798 0.808 0.818 0.828 0.837 0.847 0.857 0.867 0.877 0.887  
0.896 0.906 0.913 0.930  
-0.035 -0.073 -0.111 -0.149 -0.187 -0.225 -0.263 -0.301 -0.339 -0.378 -0.415  
-0.453 -0.492 -0.530 -0.567 -0.605 -0.644 -0.682 -0.721 -0.759 -0.796 -0.835  
-0.873 -0.910 -0.950 -0.987 -1.027 -1.065 -1.104 -1.142 -1.181 -1.219 -1.257  
-1.296 -1.334 -1.373 -1.412 -1.450 -1.489 -1.527 -1.565 -1.605 -1.644 -1.682  
-1.721 -1.759 -1.798 -1.836 -1.876 -1.914 -1.954 -1.991 -2.030 -2.069 -2.108  
-2.147 -2.186 -2.224 -2.263 -2.302 -2.341 -2.380 -2.419 -2.458 -2.497 -2.536  
-2.575 -2.614 -2.653 -2.692 -2.730 -2.769 -2.809 -2.847 -2.886 -2.928 -2.966  
-3.004 -3.044 -3.083 -3.113 -3.135  
\*\*\* Line transitions  
1 2 -1 0 1 0 0 6.6000e-02 7.000e-01  
F 1 7 0. 0.  
1 3 -1 0 1 0 0 1.3300e-01 7.000e-01  
F 1 7 0. 0.

1 4		0 0 4 0 0 0.0000e+00	5.000e-01
1 5		-1 0 1 0 0 2.6550e-01	2.000e-01
	F 1 7 0.	0.	
1 6		0 0 4 0 0 0.0000e+00	5.000e-01
1 7		0 0 4 0 0 0.0000e+00	5.000e-01
1 8		-1 0 1 0 0 7.4200e-02	2.000e-01
	F 1 7 0.	0.	
1 9		0 0 4 0 0 0.0000e+00	5.000e-01
1 10		0 0 4 0 0 0.0000e+00	5.000e-01
2 3		0 0 4 0 0 0.0000e+00	5.000e-01
2 4		-1 0 1 0 0 2.8900e-02	2.000e-01
	F 1 7 0.	0.	
2 5		0 0 4 0 0 0.0000e+00	5.000e-01
2 6		-1 0 1 0 0 6.5669e-01	2.000e-01
	F 1 7 0.	0.	
2 7		-1 0 1 0 0 5.7100e-03	2.000e-01
	F 1 7 0.	0.	
2 8		0 0 4 0 0 0.0000e+00	5.000e-01
2 9		-1 0 1 0 0 1.2250e-01	2.000e-01
	F 1 7 0.	0.	
2 10		0 0 4 0 0 0.0000e+00	5.000e-01
3 4		-1 0 1 0 0 2.9000e-02	2.000e-01
	F 1 7 0.	0.	
3 5		0 0 4 0 0 0.0000e+00	5.000e-01
3 6		-1 0 1 0 0 6.5662e-01	2.000e-01
	F 1 7 0.	0.	
3 7		-1 0 1 0 0 5.7000e-03	2.000e-01
	F 1 7 0.	0.	
3 8		0 0 4 0 0 0.0000e+00	5.000e-01
3 9		-1 0 1 0 0 1.2230e-01	2.000e-01
	F 1 7 0.	0.	
3 10		0 0 4 0 0 0.0000e+00	5.000e-01
4 5		-1 0 1 0 0 3.3500e-01	7.000e-01
	F 1 7 0.	0.	
4 6		0 0 4 0 0 0.0000e+00	5.000e-01
4 7		0 0 4 0 0 0.0000e+00	5.000e-01
4 8		-1 0 1 0 0 2.7730e-01	2.000e-01
	F 1 7 0.	0.	
4 9		0 0 4 0 0 0.0000e+00	5.000e-01
4 10		0 0 4 0 0 0.0000e+00	5.000e-01
5 6		-1 0 1 0 0 4.8033e-02	7.000e-01
	F 1 7 0.	0.	
5 7		-1 0 1 0 0 9.5650e-02	2.000e-01
	F 1 7 0.	0.	
5 8		0 0 4 0 0 0.0000e+00	5.000e-01
5 9		-1 0 1 0 0 5.5698e-01	2.000e-01
	F 1 7 0.	0.	
5 10		0 0 4 0 0 0.0000e+00	5.000e-01
6 7		0 0 4 0 0 0.0000e+00	5.000e-01
6 8		-1 0 1 0 0 1.5295e-02	2.000e-01
	F 1 7 0.	0.	
6 9		0 0 4 0 0 0.0000e+00	5.000e-01
6 10		-1 0 1 0 0 1.6875e+00	2.000e-01
	F 1 7 0.	0.	
7 8		-1 0 1 0 0 4.6300e-01	7.000e-01
	F 1 7 0.	0.	
7 9		0 0 4 0 0 0.0000e+00	5.000e-01
7 10		0 0 4 0 0 0.0000e+00	5.000e-01
8 9		-1 0 1 0 0 8.5391e-02	7.000e-01
	F 1 7 0.	0.	
8 10		0 0 4 0 0 0.0000e+00	5.000e-01
9 10		-1 0 1 0 0 3.9660e-03	7.000e-01
	F 1 7 0.	0.	

# Line list

9.3110	08.05	-2.192	0.000	0.5	1074000.000	0.5	9.39	0.00	0.00	0	!TBtr
9.3110	08.05	-2.192	0.000	0.5	1074000.000	1.5	9.39	0.00	0.00	0	!TBtr
9.3915	08.05	-2.047	0.000	0.5	1064790.000	0.5	9.53	0.00	0.00	0	!TBtr
9.3915	08.05	-2.047	0.000	0.5	1064790.000	1.5	9.53	0.00	0.00	0	!TBtr
9.5082	08.05	-1.883	0.000	0.5	1051724.000	0.5	9.68	0.00	0.00	0	!TBtr
9.5082	08.05	-1.883	0.000	0.5	1051724.000	1.5	9.68	0.00	0.00	0	!TBtr
9.6840	08.05	-1.695	0.000	0.5	1032631.000	0.5	9.85	0.00	0.00	0	!TBtr
9.6840	08.05	-1.695	0.000	0.5	1032631.000	1.5	9.85	0.00	0.00	0	!TBtr
9.9688	08.05	-1.471	0.000	0.5	1003130.000	0.5	10.05	0.00	0.00	0	!TBtr
9.9688	08.05	-1.471	0.000	0.5	1003130.000	1.5	10.05	0.00	0.00	0	!TBtr
10.2247	08.05	-2.110	96375.000	0.5	1074400.000	1.5	9.39	0.00	0.00	0	!TBtr
10.2247	08.05	-2.110	96375.000	0.5	1074400.000	2.5	9.39	0.00	0.00	0	!TBtr
10.2303	08.05	-1.809	96907.500	1.5	1074400.000	1.5	9.39	0.00	0.00	0	!TBtr
10.2303	08.05	-1.809	96907.500	1.5	1074400.000	2.5	9.39	0.00	0.00	0	!TBtr
10.2456	08.05	-3.413	96375.000	0.5	1072406.849	0.5	8.09	0.00	0.00	0	!TBtr
10.2512	08.05	-3.112	96907.500	1.5	1072406.849	0.5	8.09	0.00	0.00	0	!TBtr
10.3203	08.05	-1.960	96375.000	0.5	1065337.000	2.5	9.53	0.00	0.00	0	!TBtr
10.3206	08.05	-1.956	96375.000	0.5	1065311.000	1.5	9.24	0.00	0.00	0	!NISTtr
10.3260	08.05	-1.702	96907.500	1.5	1065337.000	2.5	9.32	0.00	0.00	0	!NISTtr
10.3263	08.05	-2.655	96907.500	1.5	1065311.000	1.5	8.54	0.00	0.00	0	!NISTtr
10.3473	08.05	-3.262	96375.000	0.5	1062811.418	0.5	8.23	0.00	0.00	0	!TBtr
10.3530	08.05	-2.961	96907.500	1.5	1062811.418	0.5	8.23	0.00	0.00	0	!TBtr
10.4611	08.05	-1.789	96375.000	0.5	1052301.000	2.5	9.69	0.00	0.00	0	!TBtr
10.4612	08.05	-1.788	96375.000	0.5	1052288.000	1.5	9.39	0.00	0.00	0	!NISTtr
10.4669	08.05	-1.533	96907.500	1.5	1052301.000	2.5	9.47	0.00	0.00	0	!NISTtr
10.4670	08.05	-2.488	96907.500	1.5	1052288.000	1.5	8.69	0.00	0.00	0	!NISTtr
10.4803	08.05	-3.103	96375.000	0.5	1050543.000	0.5	8.38	0.00	0.00	0	!NISTtr
10.4813	08.05	-1.194	0.000	0.5	954080.000	0.5	10.29	0.00	0.00	0	!TBtr
10.4813	08.05	-1.194	0.000	0.5	954080.000	1.5	10.29	0.00	0.00	0	!TBtr
10.4862	08.05	-2.804	96907.500	1.5	1050543.000	0.5	8.68	0.00	0.00	0	!NISTtr
10.6728	08.05	-1.589	96375.000	0.5	1033334.000	2.5	9.88	0.00	0.00	0	!TBtr
10.6731	08.05	-1.588	96375.000	0.5	1033310.000	1.5	9.58	0.00	0.00	0	!NISTtr
10.6789	08.05	-1.333	96907.500	1.5	1033334.000	2.5	9.66	0.00	0.00	0	!NISTtr
10.6792	08.05	-2.287	96907.500	1.5	1033310.000	1.5	8.88	0.00	0.00	0	!NISTtr
10.7020	08.05	-2.905	96375.000	0.5	1030780.000	0.5	8.56	0.00	0.00	0	!NISTtr
10.7081	08.05	-2.605	96907.500	1.5	1030780.000	0.5	8.86	0.00	0.00	0	!NISTtr
11.0155	08.05	-1.347	96375.000	0.5	1004184.000	2.5	10.09	0.00	0.00	0	!TBtr
11.0157	08.05	-1.347	96375.000	0.5	1004170.000	1.5	9.79	0.00	0.00	0	!NISTtr
11.0220	08.05	-1.093	96907.500	1.5	1004184.000	2.5	9.87	0.00	0.00	0	!NISTtr
11.0222	08.05	-2.048	96907.500	1.5	1004170.000	1.5	9.09	0.00	0.00	0	!NISTtr
11.0656	08.05	-2.670	96375.000	0.5	1000080.000	0.5	8.77	0.00	0.00	0	!NISTtr
11.0721	08.05	-2.365	96907.500	1.5	1000080.000	0.5	9.07	0.00	0.00	0	!NISTtr
11.5821	08.05	-1.004	0.000	0.5	863397.700	1.5	10.09	0.00	0.00	0	!NISTtr
11.5830	08.05	-1.306	0.000	0.5	863333.800	0.5	10.09	0.00	0.00	0	!NISTtr
11.6349	08.05	-1.039	96375.000	0.5	955860.000	2.5	10.35	0.00	0.00	0	!TBtr
11.6350	08.05	-1.041	96375.000	0.5	955851.000	1.5	10.05	0.00	0.00	0	!NISTtr
11.6421	08.05	-0.784	96907.500	1.5	955860.000	2.5	10.13	0.00	0.00	0	!NISTtr
11.6422	08.05	-1.740	96907.500	1.5	955851.000	1.5	9.35	0.00	0.00	0	!NISTtr
11.7328	08.05	-2.355	96375.000	0.5	948690.000	0.5	9.03	0.00	0.00	0	!NISTtr
11.7401	08.05	-2.056	96907.500	1.5	948690.000	0.5	9.33	0.00	0.00	0	!NISTtr
12.9781	08.05	-0.611	96375.000	0.5	866901.500	2.5	10.68	0.00	0.00	0	!TBtr
12.9785	08.05	-0.609	96375.000	0.5	866880.100	1.5	10.39	0.00	0.00	0	!NISTtr
12.9871	08.05	-0.357	96907.500	1.5	866901.500	2.5	10.46	0.00	0.00	0	!NISTtr
12.9875	08.05	-1.308	96907.500	1.5	866880.100	1.5	9.69	0.00	0.00	0	!NISTtr
13.2219	08.05	-1.942	96375.000	0.5	852696.000	0.5	9.34	0.00	0.00	0	!NISTtr
13.2312	08.05	-1.642	96907.500	1.5	852696.000	0.5	9.64	0.00	0.00	0	!NISTtr
15.0089	08.05	-0.451	0.000	0.5	666269.800	1.5	10.42	0.00	0.00	0	!NISTtr
15.0125	08.05	-0.752	0.000	0.5	666113.200	0.5	10.42	0.00	0.00	0	!NISTtr
17.2920	08.05	0.118	96375.000	0.5	674676.800	2.5	11.16	0.00	0.00	0	!TBtr
17.2935	08.05	0.119	96375.000	0.5	674625.700	1.5	10.87	0.00	0.00	0	!NISTtr
17.3079	08.05	0.374	96907.500	1.5	674676.800	2.5	10.94	0.00	0.00	0	!NISTtr
17.3095	08.05	-0.581	96907.500	1.5	674625.700	1.5	10.16	0.00	0.00	0	!NISTtr
18.3937	08.05	-1.238	96375.000	0.5	640039.800	0.5	9.76	0.00	0.00	0	!NISTtr
18.4117	08.05	-0.936	96907.500	1.5	640039.800	0.5	10.06	0.00	0.00	0	!NISTtr

# Grotrian diagram

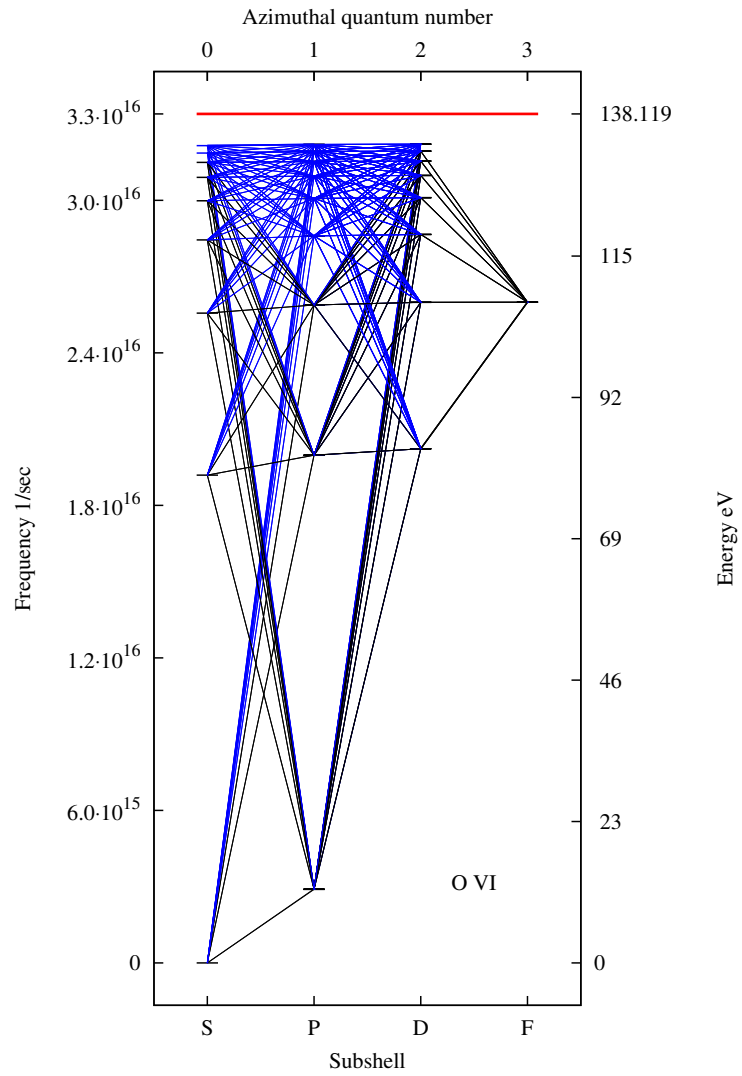


Figure A.1: Grotrian diagram for O VI.



## Appendix B

# Catalog of Galactic CNe with Supersoft Phase

This catalog lists the most recent galactic CNe which were observed to have supersoft phase. It can be considered as an update of the online<sup>1</sup> catalog of Greiner (2000). For each novae equatorial coordinates for year 2000 and finder charts were collected from the SIMBAD<sup>2</sup> database. Other data on each novae were collected from the scientific literature. The time of visual maximum ( $t_0$ ) is given in UT, where available decline rates in the optical band ( $t_2$ ,  $t_3$ ) are also given. The object type CN refers to classical novae, RN stands for recurrent novae. The general data table has data on maximum optical brightness in V band, interstellar reddening (either with (B-V) color index or E(B-V) color excess), measured expansion or terminal velocity, distance to the object, absolute brightness in V band and orbital period. The times X-on and

---

<sup>1</sup><http://www.mpe.mpg.de/~jcg/sss/ssscat.html>

<sup>2</sup><http://simbad.u-strasbg.fr/simbad/>

X-off refers to the dates when the nova was first and last observed in the supersoft range, respectively. For some novae only the estimated length of the supersoft phase were available, in those cases this is given as  $t_{\text{BOL}}$  in years. Model data is listed if either black-body (BB) or WD model fits were available. From modeling only the most important parameters are shown, the effective temperature ( $T_{\text{eff}}$ ), the date after  $t_0$  when the spectrum was taken, the derived luminosity and hydrogen column-density. Data are labeled with superscripts and their sources can be found in the References.

Journal Abbreviations:

New Astr.	New Astronomy
RMxAC2	Revista Mexicana de Astronomia y Astrofisica
ApJ	Astrophysical Journal
AN	Astronomische Nachrichten
ATel	The Astronomer's Telegram
IAUC	International Astronomical Union Circulars
MNRAS	Monthly Notices of the Royal Astronomical Society
A&A	Astronomy & Astrophysics
AAS	American Astronomical Society
AJ	The Astronomical Journal
AB	Astrophysical Bulletin

# GQ Mus

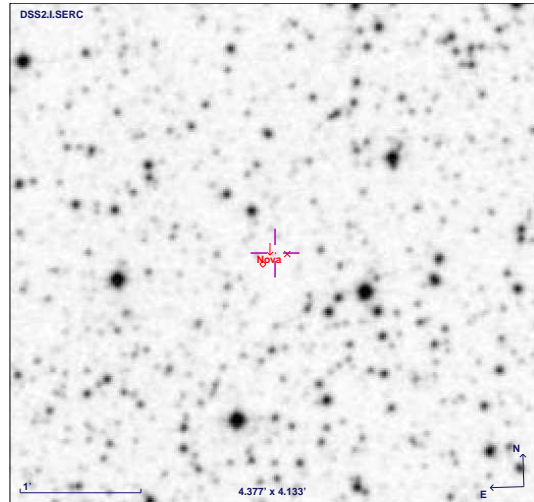
RA (2000) = 11 52 02.5

DEC(2000) = -67 12 24

$t_0 = 1983/01/18^{[2]}$

$t_3 = 40^{[2]}$  [d]

Type: CN



## General Data

$m_B$ [mag] = $7.21^{[1]}$	$E(B-V) = 0.45 \pm 0.15^{[2]}$	$v_\infty$ [km/s] = $550 - 800^{[1]}$
$D$ [kpc] = $4.7 \pm 1.5^{[1]}$	$M_V = -7.75^{[2]}$	$P_{\text{orb}}$ [d] = $0.0588^{[1]}$
X-ray on =	$t_{\text{Bol}}$ [yr] = $9 - 10^{[3]}$	

## Model Data

Model	$T_{\text{eff}}$ [ $\times 10^3$ K]	t after $t_0$ [d]	L [erg/s]	$N_H$ [ $10^{21}$ cm $^{-2}$ ]
BB $^{[1]}$	290 - 400			1 - 3.4
WD				

## References

1	J. Greiner; 2000, New Astr., 5, 137
2	J. Krautter et al.; 1984, A&A, 137, 307
3	M. Orio; 2004, RMxAC, 20, 182

# V1974 Cyg

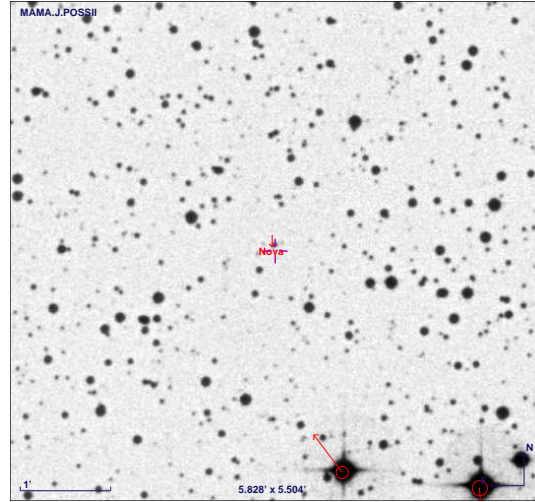
RA (2000) = 20 30 31.8

DEC(2000) = +52 37 53

$t_0 = 1992/02/22^{[3]}$

$t_2 = 17^{[1]}$  d

Type: CN



## General Data

$m_V$ [mag] = $4.3^{[3]}$	$(B-V) = -0.6 \pm 0.45^{[1]}$	$v_\infty$ [km/s] = $2000^{[1]}$
$D$ [kpc] = $1.8 - 3.2^{[1]}$	$M_V$ [mag] = $-7.78 \pm 0.12^{[1]}$	$P_{\text{orb}}$ [d] = $0.081263^{[1]}$
X-ray on = $t_0 + 434^{[2]}$	$t_{\text{Bol}}$ [yr] = $2 - 3^{[2]}$	

## Model Data

Model	$T_{\text{eff}} [\times 10^3 \text{ K}]$	t after $t_0$ [d]	L [erg/s]	$N_H [10^{21} \text{ cm}^{-2}]$
BB <sup>[1]</sup>	220 - 300			
WD <sup>[1]</sup>	350 - 600			1.9 - 2.5

## References

- |   |  |
|---|--|
| 1 | J. Greiner; 2000, New Astr., 5, 137      |
| 2 | M. Orio; 2004, RMxAC, 20, 182            |
| 3 | J.A. DeYoung et al.; 1994, ApJ, 431, L47 |

# V2491 Cyg

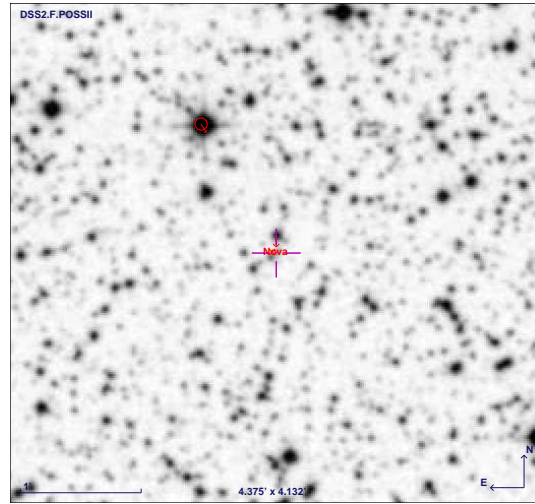
RA (2000) = 19 43 01.96

DEC(2000) = +32 19 13.8

$t_0 = 2008/04/10.7^{[2]}$

$t_2 = 5.65 \pm 0.1^{[3]}$  d

Type: CN



## General Data

$m_V$ [mag] = 7.5 <sup>[4]</sup>	$E(B-V) = 0.43^{[5]}$	$v_\infty$ [km/s] = 4800
$D$ [kpc] = 10.5 <sup>[2]</sup>	$M_V =$	$P_{\text{orb?}} = 0.09580^{[4]}$
X-ray on =	$t_{\text{Bol}}$ [month] < 3 <sup>[3]</sup>	

## Model Data

Model	$T_{\text{eff}}$ [ $\times 10^3$ K]	t after $t_0$ [d]	L [erg/s]	$N_H$ [ $10^{21}$ cm <sup>-2</sup> ]
BB <sup>[2,3]</sup>	520	39.9	$1 \times 10^{40}$	5 <sup>[2]</sup>
BB <sup>[2,3]</sup>	570	49.7	$8.7 \times 10^{38}$	4.7 <sup>[2]</sup>
WD <sup>[1]</sup>	600			2.8 – 5

## References

- |   |   |
|---|---|
| 1 | D.R. van Rossum et al.; 2010, AN, 331 175 |
| 2 | J.-U. Ness; 2010, AN, 331, 179            |
| 3 | this work                                 |
| 4 | A. Baklanov et al.; 2008, ATel, 1514      |
| 5 | R.J. Rudy et al.; 2008, IAUC, 8938        |

# V4743 Sgr

RA (2000) = 19 01 09.38

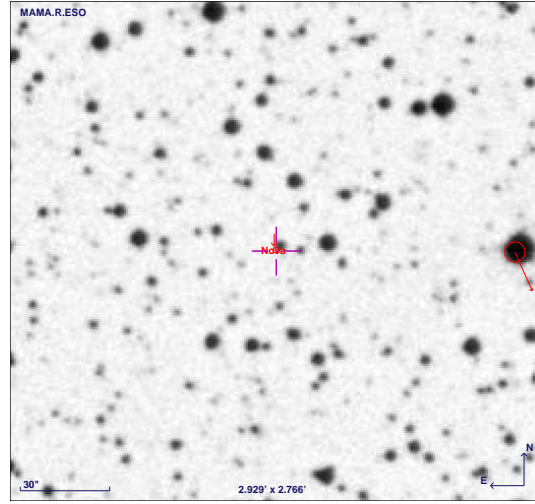
DEC(2000) = -22 00 05.9

$t_0 = 2002/09/18.3^{[1]}$

$t_2 = 9 \text{ d}^{[1]}$

$t_3 = 16 \text{ d}^{[1]}$

Type: CN



## General Data

$m_V$ [mag] = 5 <sup>[1]</sup>	$E(B-V) = 0.25^{[6]}$	$v_\infty$ [km/s] = 2200-2700 <sup>[1]</sup>
$D$ [kpc] = $3.9 \pm 0.3^{[6]}$	$M_V =$	$P_{\text{orb}}$ [d] = 0.2799 <sup>[5]</sup>
X-ray on = $t_0 + 180^{[4]}$ d	$t_{\text{Bol}}$ [yr] $\approx 1.5^{[4]}$	

## Model Data

Model	$T_{\text{eff}}$ [ $\times 10^3$ K]	$t$ after $t_0$ [d]	$L$ [erg/s]	$N_H$ [ $10^{21} \text{ cm}^{-2}$ ]
BB <sup>[2]</sup>	390	180.4	$1.6 \times 10^{40}$	2.1
BB <sup>[2]</sup>	460	371	$1.8 \times 10^{39}$	1.8
WD <sup>[3]</sup>	600	182		4.6
WD <sup>[3]</sup>	580	303		4.4
WD <sup>[3]</sup>	580	372		4.2
WD <sup>[3]</sup>	540	528		3.3
WD <sup>[4]</sup>	580	182	$7.8 \times 10^{37}$	0.46
WD <sup>[4]</sup>	600	303	$1.1 \times 10^{38}$	0.51
WD <sup>[4]</sup>	560	372	$8.5 \times 10^{37}$	0.51
WD <sup>[4]</sup>	455	528	$3.7 \times 10^{37}$	0.51

## References

- 1 G.E. Morgan et al.; 2003, MNRAS, 344 521
- 2 J.-U. Ness; 2010, AN, 331, 179
- 3 A. Petz et al.; 2005, A&A, 431, 321
- 4 this work
- 5 T.W. Kang et al.; 2006, ApJ, 132, 608
- 6 K.M. Vanlandingham et al.; 2007, AAS, 210

# RS Oph

RA (2000) = 17 50 13.20

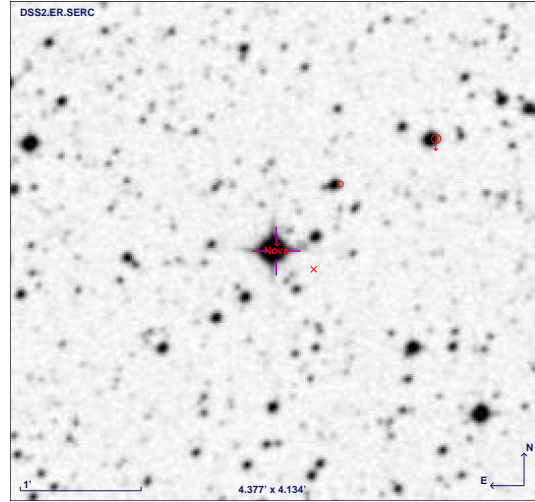
DEC(2000) = -06 42 28.48

$t_0 = 2006/02/12.85^{[2]}$

$t_2 = 6.8^{[1]}$  d

$t_3 = 14.0^{[1]}$  d

Type: RN



## General Data

$m_V$ [mag] = $4.5^{[2]}$	$E(B-V) = 0.73^{[1]}$	$v_\infty$ [km/s] = $5600 \pm 1100^{[2]}$
$D$ [kpc] = $4.3 \pm 0.7^{[1]}$ , $1.6 \pm 0.3^{[3]}$	$M_{\text{Bol}} = -3.66^{[1]}$	$P_{\text{orb}}$ [d] = $453.6 \pm 0.4^{[6]}$
X-ray on =	$t_{\text{Bol}}$ [yr] =	

## Model Data

Model	$T_{\text{eff}} [\times 10^3 \text{ K}]$	t after $t_0$ [d]	L[erg/s]	$N_H [10^{21} \text{ cm}^{-2}]$
BB <sup>[4]</sup>	620	39.7	$2.7 \times 10^{38}$	5.1
BB <sup>[4]</sup>	500	66.9	$7.2 \times 10^{39}$	6.9
WD <sup>[5]</sup>	550	39.7		4.8

## References

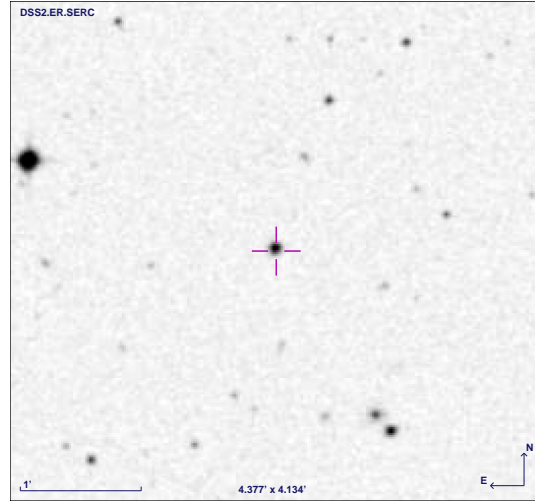
- |   |                                       |
|---|---------------------------------------|
| 1 | B. E. Schaefer; 2009, ApJ, 697, 721   |
| 2 | K. Hirose; 2006, IAUC, 8671           |
| 3 | M.F. Bode; 2009, AN, 331, 160         |
| 4 | J.U. Ness; 2010, AN, 331, 179         |
| 5 | D.R. van Rossum et al.; AN, 331, 175  |
| 6 | E. Brandi et al.; 2009, A&A, 497, 815 |

# KT Eri

RA (2000) = 04 47 54.21  
 DEC(2000) = -10 10 43.1

$t_0 = 2009/11/14.572^{[1]}$   
 $t_0 = 2009/11/19.241^{[3]}$   
 $t_2 = 8^{[3]}$   
 $t_3 = 15^{[3]}$

Type: CN



## General Data

$m_V$ [mag] = 5.6 <sup>[3]</sup>	$E(B-V) = 0.08^{[3]}$	$v_\infty$ [km/s] = 5800 <sup>[1]</sup>
$D$ [kpc] = 6.5 <sup>[3]</sup> , 10.5 <sup>[ ]</sup>	$M_V = -8.7^{[3]}$	$P_{\text{orb}} =$
X-ray on = 2010/01/19 <sup>[1]</sup>	$t_{\text{Bol}}$ [yr] =	

## Model Data

Model	$T_{\text{eff}}$ [ $\times 10^3$ K]	$t$ after $t_0$ [day]	$L$ [erg/s]	$N_H$ [ $10^{21}$ cm <sup>-2</sup> ]
BB <sup>[1]</sup>	520	61.4		$2.8 \pm 0.1$
BB <sup>[1]</sup>	210	65.5		$2.8 \pm 0.1$
BB <sup>[2]</sup>	440	70.4		1.2
WD				

## References

- |   |                                     |
|---|-------------------------------------|
| 1 | M.F. Bode et al.; 2010, ATel, 2392  |
| 2 | J.-U. Ness et al.; 2010, ATel, 2418 |
| 3 | E. Ragan et al.; 2009, ATel, 2327   |

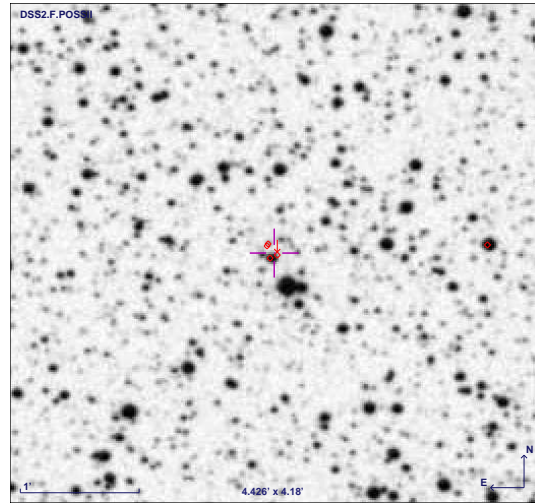


# V458 Vul

RA (2000) = 19 54 24.3  
 DEC(2000) = +20 52 47

$t_0 = 2007/08/8.54^{[1]}$   
 $t_2 = 7^{[1]}$  d

Type: CN



## General Data

$m_V$ [mag] =	$E(B-V) = 0.6^{[1]}$	$v_\infty$ [km/s] =
$D$ [kpc] = $8.8 \pm 0.8^{[1]}$	$M_V =$	$P_{\text{orb}}$ [d] = 0.58946
X-ray on = $t_0 + 315^{[1]}$ d	$t_{\text{Bol}}$ [yr] > $2^{[1]}$	

## Model Data

Model	$T_{\text{eff}}$ [ $\times 10^3$ K]	t after $t_0$ [d]	L [erg/s]	$N_H$ [ $10^{21}$ cm $^{-2}$ ]
BB <sup>[2]</sup>	333	37		3.3
WD				

## References

- |   |  |
|---|--|
| 1 | J.-U. Ness et al.; 2010, AJ, 137, 4160 |
| 2 | J.J. Drake et al.; 2008, ATel, 1721    |

# V5116 Sgr

RA (2000) = 18 17 50.77

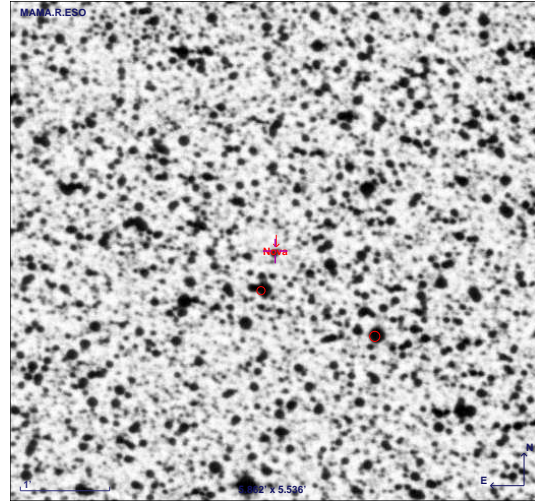
DEC(2000) = -30 26 31.2

$t_0 = 2005/07/5.085^{[2]}$

$t_2 = 6.5 \pm 1^{[5]}$  days

$t_3 = 39^{[3]}$  days

Type: CN



## General Data

$m_V$ [mag] = $7.2^{[2]}$	$(B-V) = 0.48^{[8]}$	$v_\infty$ [km/s] = $2200^{[4]}$
D [kpc] = $11.3 \pm 3^{[6]}$	$M_V$ [mag] = $-8.85 \pm 0.04^{[5]}$	$P_{\text{orb}}$ [h] = $2.9712 \pm 0.0024^{[5]}$
X-ray on $\approx t_0 + 700^{[9]}$ d	$t_{\text{Bol}}$ [yr] $\approx 1^{[9]}$	

## Model Data

Model	$T_{\text{eff}}$ [ $\times 10^3$ K]	t after $t_0$ [d]	L [erg/s]	$N_H$ [ $\times 10^{21}$ cm $^{-2}$ ]
BB				
WD <sup>[1]</sup>	$610 \pm 0.6$		$2.6 \pm 0.7 \times (d/10\text{kpc})$	$1.3 \pm 0.1$
WD <sup>[7]</sup>	465			

## References

1 G. Sala et al.; 2007, ATel, 1184	6 G. Sala et al.; 2008b, A&A, 473, 61
2 W. Liller; 2005, IAUC, 8559	7 T. Nelson et al.; 2007, ATel, 1202
3 R. Williams et al.; 2008, ApJ, 685, 451	8 A.C. Gilmore et al.; 2005, IAUC, 8559
4 R. Russell et al.; 2005, IAUC 8579	9 G. Sala et al.; 2010, AN, 331, 201
5 A. Dobrotka et al.; 2008, A&A, 478, 815	

# V723 Cas

RA (2000) = 01 05 05.37

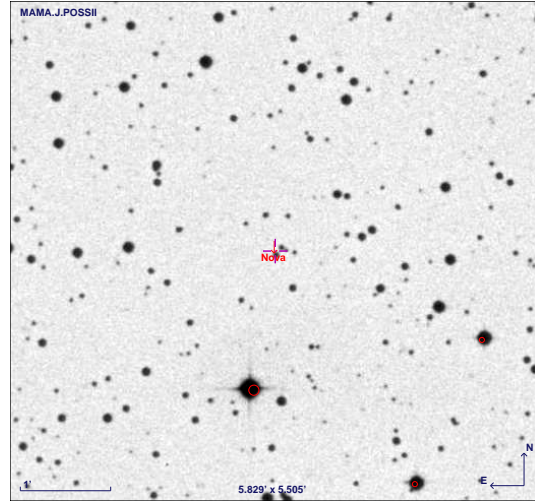
DEC(2000) = +54 00 40.5

$t_0 = 1995/12/17^{[3]}$

$t_2 = 340^{[4]}$

$t_3 = 515^{[4]}$

Type: CN



## General Data

$m_V$ [mag] = $7.1^{[3]}$	$E(B-V) = 0.57 \pm 0.05^{[4]}$	$v_\infty$ [km/s] =
$D$ [kpc] = $3.85^{+0.23}_{-0.21}^{[1]}$	$M_V =$	$P_{\text{orb}}$ [d] = $0.693265^{[4]}$
X-ray on =	$t_{\text{Bol}}$ [yr] =	

## Model Data

Model	$T_{\text{eff}}$ [ $\times 10^3$ K]	Peak flux [cts/s]	$L$ [erg/s]	$N_H$ [ $10^{21}$ cm $^{-2}$ ]
BB <sup>[2]</sup>	280 – 380	$0.022 \pm 0.01$	$> 0.5 \times 10^{37}$	1.6 – 4.8
WD				

## References

1 J.E. Lyke et al.; 2009, ApJ, 138, 1090	4 V.P. Goranskij et al.; 2007, AB, 62, 2
2 J.-U. Ness et al.; 2008, AJ, 135, 1328	
3 Munari et al.; 1996, A&A, 315, 166	

# V1494 Aql

RA (2000) = 19 23 05.30

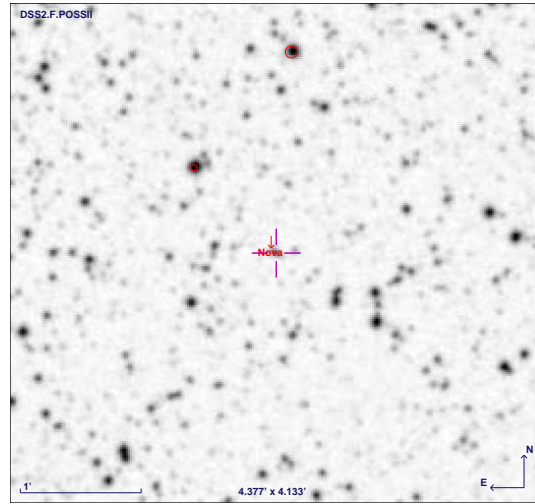
DEC(2000) = +04 57 19.1

$t_0 = 1999/12/3.4^{[2]}$

$t_2 = 6.6 \pm 0.5^{[2]}$  d

$t_3 = 16 \pm 0.5^{[2]}$  d

Type: CN



## General Data

$m_V$ [mag] = 4.0	$E(B-V) = 0.6 \pm 0.1^{[1]}$	$v_\infty$ [km/s] = 2900 <sup>[1]</sup>
$D$ [kpc] = $1.6 \pm 0.2^{[1]}$ , $3.6 \pm 0.3^{[2]}$	$M_V = -8.8 \pm 0.2^{[2]}$	$P_{\text{orb}} =$
X-ray on = $t_0 + 180^{[3]}$ d	$t_{\text{Bol}}$ [year] = $2.5 - 3^{[3]}$	

## Model Data

Model	$T_{\text{eff}}$ [ $\times 10^3$ K]	t after $t_0$ [d]	L [erg/s]	$N_H$ [ $10^{21}$ cm <sup>-2</sup> ]
BB				
WD				

## References

- |   |                                       |
|---|---------------------------------------|
| 1 | T. Iijima et al.; 2003, A&A, 404, 997 |
| 2 | L.L. Kiss et al.; 2000, A&A, 355, L9  |
| 3 | M. Orio; 2000, RMxAC, 20, 182         |